



# Experimental and Computational Icing Simulation for Large Swept Wings

*Andy P. Broeren*  
*Glenn Research Center, Cleveland, Ohio*

*Sam Lee*  
*HX5, LLC, Brook Park, Ohio*

*Michael B. Bragg*  
*University of Washington, Seattle, Washington*

*Brian S. Woodard*  
*University of Illinois, Urbana, Illinois*

*Emmanuel Radenac*  
*Office National d'Etudes et de Recherches Aérospatiales, Toulouse, France*

*Frédéric Moens*  
*Office National d'Etudes et de Recherches Aérospatiales, Meudon, France*

## NASA STI Program . . . in Profile

Since its founding, NASA has been dedicated to the advancement of aeronautics and space science. The NASA Scientific and Technical Information (STI) Program plays a key part in helping NASA maintain this important role.

The NASA STI Program operates under the auspices of the Agency Chief Information Officer. It collects, organizes, provides for archiving, and disseminates NASA's STI. The NASA STI Program provides access to the NASA Technical Report Server—Registered (NTRS Reg) and NASA Technical Report Server—Public (NTRS) thus providing one of the largest collections of aeronautical and space science STI in the world. Results are published in both non-NASA channels and by NASA in the NASA STI Report Series, which includes the following report types:

- TECHNICAL PUBLICATION. Reports of completed research or a major significant phase of research that present the results of NASA programs and include extensive data or theoretical analysis. Includes compilations of significant scientific and technical data and information deemed to be of continuing reference value. NASA counter-part of peer-reviewed formal professional papers, but has less stringent limitations on manuscript length and extent of graphic presentations.
- TECHNICAL MEMORANDUM. Scientific and technical findings that are preliminary or of specialized interest, e.g., “quick-release” reports, working papers, and bibliographies that contain minimal annotation. Does not contain extensive analysis.
- CONTRACTOR REPORT. Scientific and technical findings by NASA-sponsored contractors and grantees.
- CONFERENCE PUBLICATION. Collected papers from scientific and technical conferences, symposia, seminars, or other meetings sponsored or co-sponsored by NASA.
- SPECIAL PUBLICATION. Scientific, technical, or historical information from NASA programs, projects, and missions, often concerned with subjects having substantial public interest.
- TECHNICAL TRANSLATION. English-language translations of foreign scientific and technical material pertinent to NASA's mission.

For more information about the NASA STI program, see the following:

- Access the NASA STI program home page at <http://www.sti.nasa.gov>
- E-mail your question to [help@sti.nasa.gov](mailto:help@sti.nasa.gov)
- Fax your question to the NASA STI Information Desk at 757-864-6500
- Telephone the NASA STI Information Desk at 757-864-9658
- Write to:  
NASA STI Program  
Mail Stop 148  
NASA Langley Research Center  
Hampton, VA 23681-2199



# Experimental and Computational Icing Simulation for Large Swept Wings

*Andy P. Broeren*  
*Glenn Research Center, Cleveland, Ohio*

*Sam Lee*  
*HX5, LLC, Brook Park, Ohio*

*Michael B. Bragg*  
*University of Washington, Seattle, Washington*

*Brian S. Woodard*  
*University of Illinois, Urbana, Illinois*

*Emmanuel Radenac*  
*Office National d'Etudes et de Recherches Aérospatiales, Toulouse, France*

*Frédéric Moens*  
*Office National d'Etudes et de Recherches Aérospatiales, Meudon, France*

National Aeronautics and  
Space Administration

Glenn Research Center  
Cleveland, Ohio 44135

## Acknowledgments

The authors are indebted to many colleagues who made many significant contributions to this work. They are too numerous to name here; however, these individuals have been appropriately acknowledged in the many references cited in this report. The NASA-supported portion of this research was originally funded under the Atmospheric Environment Safety Technologies Project of the Aviation Safety Program with continued support under the Advanced Air Transport Technology and Aeronautics Evaluation and Test Capabilities Projects of the Advanced Air Vehicles Program. The Federal Aviation Administration (FAA) and Office National d'Études et de Recherches Aérospatiales (ONERA) also supported this research through interagency and international agreements, respectively. The university authors were supported from FAA Grant Award Number 15-G-009. All of the individual collaborators, organizations, projects, and programs are gratefully acknowledged.

This work was sponsored by the Advanced Air Vehicle Program  
at the NASA Glenn Research Center

Trade names and trademarks are used in this report for identification  
only. Their usage does not constitute an official endorsement,  
either expressed or implied, by the National Aeronautics and  
Space Administration.

*Level of Review:* This material has been technically reviewed by expert reviewer(s).

# Contents

Executive Summary.....	1
1.0 Introduction .....	2
1.1 Background and Motivation.....	3
1.2 Iced Airfoil Aerodynamic Simulation SUNSET I .....	4
1.3 Goal, Objectives, and Approach .....	4
2.0 Project Description.....	4
2.1 Phase I: 3D Ice-Accretion Classification .....	5
2.2 Phase II: Ice-Accretion and Aerodynamic Measurement Methods Development .....	6
2.2.1 Baseline Model Selection .....	6
2.2.2 3D Ice-Accretion Measurement.....	8
2.2.3 Aerodynamic Measurement Methods .....	9
2.3 Phase III: Ice-Accretion Testing .....	10
2.3.1 Selection of Airplane Missions and Simulation of Icing Conditions.....	10
2.3.2 Design of Hybrid Model Wing Sections for IRT.....	12
2.3.3 Ice-Accretion Testing .....	15
2.3.4 Posttest Comparison of Experimental and Computational Ice Shapes .....	17
2.4 Phases IV, V, and VI: Aerodynamic Testing at Low to High Reynolds Number .....	18
2.4.1 Experimental Facilities and Test Conditions .....	18
2.4.2 Wind Tunnel Models .....	19
2.4.3 Swept-Wing Performance Parameters .....	21
2.4.4 Flow Visualization.....	22
2.4.5 Wake Survey Measurements.....	23
2.4.6 Artificial Ice Shapes.....	23
2.4.7 Configurations Tested.....	25
2.5 Phase VII: 3D Ice-Accretion and Computational Flow-Field Simulation.....	25
3.0 Key Results and Findings.....	27
3.1 Database of 3D Ice-Accretion Geometry .....	28
3.1.1 Hybrid Model Design .....	28
3.1.2 Comparison of Experimental and Computational Ice-Shape Results .....	29
3.1.3 Ice-Shape Comparison.....	38
3.1.4 Generation of Artificial Ice Shapes.....	38
3.2 Understanding of Iced Swept-Wing Aerodynamics.....	39
3.2.1 Assumptions and Limitations of the Study.....	39
3.2.2 Reynolds and Mach Number Effects .....	40
3.2.3 Key Flow-Field Features—Type I and Type II Flows.....	44
3.2.4 Differences From 2D Iced Airfoil Aerodynamics .....	46
3.3 Ice-Shape Classification and Effect of Fidelity on Swept-Wing Performance .....	47
3.3.1 Swept-Wing Ice-Shape Classification .....	47
3.3.2 Ice-Shape Fidelity Effects on Aerodynamics.....	48
3.3.3 Recommendations for Research To Advance Understanding of Ice-Shape Fidelity Effects.....	53
3.4 Computational Aerodynamic Simulation of the Iced Swept Wing .....	54
3.4.1 Application of Immersed Boundary Conditions to Iced Swept-Wing CFD Simulation .....	54
3.4.2 3D RANS Simulations of 13.3-Percent-Scale Model of Clean Swept Wing.....	55
3.4.3 3D RANS Simulations of 13.3-Percent-Scale Model of Iced Swept Wing Using Mesh Deformation Method.....	57
3.4.4 3D RANS Simulations of 13.3-Percent-Scale Model of Iced Swept Wing Using IBC .....	57
3.4.5 3D RANS and IDDES Simulations of 8.9-Percent-Scale Model of Iced Swept Wing.....	61
4.0 Summary of Results .....	62
4.1 Project Summary.....	62

4.2 Key Contributions .....	62
5.0 Concluding Remarks .....	64
5.1 Conclusions .....	64
5.2 Recommendations .....	65
5.2.1 Experimental and Computational Methods.....	66
5.2.2 Additional Research Needed.....	66
Appendix—Nomenclature.....	67
Acronyms .....	67
Symbols.....	67
References .....	68

# Experimental and Computational Icing Simulation for Large Swept Wings

Andy P. Broeren  
National Aeronautics and Space Administration  
Glenn Research Center  
Cleveland, Ohio 44135

Sam Lee  
HX5, LLC  
Brook Park, Ohio 44142

Michael B. Bragg  
University of Washington  
Seattle, Washington 98195

Brian S. Woodard  
University of Illinois  
Urbana, Illinois 61801

Emmanuel Radenac  
Office National d'Etudes et de Recherches Aérospatiales  
31000 Toulouse, France

Frédéric Moens  
Office National d'Etudes et de Recherches Aérospatiales  
92190 Meudon, France

## Executive Summary

The purpose of this final report is to summarize the key results, findings, and contributions of a large, multi-organization, multiyear effort focused on swept-wing icing and aerodynamics. This research effort was jointly sponsored by NASA, the Federal Aviation Administration (FAA), and Office National d'Etudes et de Recherches Aérospatiales (ONERA) and was supported by Boeing, the University of Illinois, the University of Virginia, and the University of Washington.

In-flight icing of aircraft has traditionally been addressed as a significant safety consideration after the conceptual and preliminary design phases. In some cases, however, the current regulatory requirements can have a significant impact on aircraft configuration and sizing decisions during the earliest design stages. As a result, there is a need to greatly improve our understanding of ice accretion and its aerodynamic effect as well as our engineering simulation tools to advance the state of the art in aircraft design and certification. This technology development is needed to enable advanced airplane configurations designed to reduce fuel burn, carbon emissions, and noise. Such technology is also relevant to emerging-market aircraft, such as urban air mobility (UAM) and electric aircraft.

Significant improvements in icing simulation tools are therefore required to realize these important advancements in aircraft development.

The overall goal of this research was to improve the experimental and computational simulation capability for icing on large swept wings typical of commercial transports. This research included both ice-accretion and aerodynamic studies using the NASA Common Research Model (CRM) as the reference geometry. For this work, a 65-percent-scale version—CRM65—was used as the full-scale baseline airplane geometry. Ice-accretion testing was conducted in the Icing Research Tunnel (IRT) at the NASA Glenn Research Center using three hybrid swept-wing models representing three different stations along the span of the CRM65 wing. The three-dimensional (3D) ice-accretion geometries obtained from these test campaigns were used to evaluate the results of NASA and ONERA 3D icing simulation tools (LEWICE3D and IGLOO3D).

In addition, the 3D ice-accretion geometries were used to develop a series of artificial full-span ice shapes for low- and high-Reynolds-number aerodynamic testing. This was carried out using reflection-plane, semispan wing models designed for the low-Reynolds-number 7- by 10-ft atmospheric wind tunnel

at Wichita State University (WSU) and for the high-Reynolds-number ONERA F1 large-scale pressurized wind tunnel. The integrated aerodynamic forces, moments, and surface pressures, along with mini-tuft flow visualizations, were acquired in each facility. Additional measurements performed at WSU included surface oil flow visualizations and wake flow-field surveys. An 8.9-percent-scale model of the CRM65 wing was tested at WSU for Reynolds number based upon model mean aerodynamic chord of  $0.8 \times 10^6$ ,  $1.6 \times 10^6$ , and  $2.4 \times 10^6$ , which corresponded to freestream Mach (M) numbers of 0.09, 0.18, and 0.27. A 13.3-percent-scale model of the CRM65 wing was tested at the ONERA F1 wind tunnel over a range of Reynolds number based upon model mean aerodynamic chord of  $1.6 \times 10^6$  to  $11.9 \times 10^6$  with a Mach number range of 0.09 to 0.34. Numerous leading-edge artificial ice-shape configurations were tested on the wind tunnel models. All configurations were full-span ice shapes and incorporated variations in the level of geometric fidelity relative to the ice accretion upon which they were based. The 3D high-fidelity ice shapes were developed from the 3D ice-accretion measurements in the IRT and were considered to accurately reproduce all of the highly 3D geometric features associated with the IRT ice accretion. A series of lower fidelity ice-shape geometries were also developed and tested.

This program marks the first nonproprietary research to generate and document full-scale swept-wing ice-shape accretions in an icing tunnel and then conduct semispan wing aerodynamic testing on scaled ice accretions at high Reynolds number (i.e., up to  $11.9 \times 10^6$ ). During this work, several new experimental and computational techniques were developed or documented, and new knowledge about swept-wing icing aerodynamics was identified. Key contributions include the following:

- Methods for designing and conducting icing tunnel tests for sections of a large-scale swept wing including hybrid model design
- Methods to measure experimental ice accretion geometry in 3D and to subsequently create highly 3D artificial ice shapes for aerodynamic testing
- Validation of low-cost, low-Reynolds-number test capability for the CRM65 wing with leading-edge ice shapes
- Integration of 3D computational methods with experimental methods to develop and conduct realistic and successful ice-accretion testing for large-scale swept-wing sections
- A preliminary aerodynamic understanding of the iced swept-wing flow field and effects of ice-shape geometric fidelity on the aerodynamic performance
- A database of experimental ice-accretion geometry and aerodynamic performance that will be accessible at <http://commonresearchmodel.larc.nasa.gov/home-2/icing-research>

In addition to these contributions, this research has resulted in the following conclusions described in this report:

- Many 3D computational simulations were required to refine the hybrid model design in the presence of the wind tunnel walls. Two-dimensional (2D) computational tools have limited value for large models, where the wind tunnel walls produce 3D flow effects that must be taken into account.
- Comparisons of computational and experimental ice shapes showed that in a number of cases there were significant differences in the results. A common trend was that the code results better matched the average experimental ice-shape cross section but typically underpredicted the maximum outer boundary of the experimental ice shape. The experimental ice accretions were highly 3D, whereas the icing code results were primarily 2D.
- Two key flow-field features were observed to result from leading-edge horn-ice-shape geometry. These two flow-field types are referred to as “Type I” and “Type II.” Type I flow fields are dominated by spanwise-running leading-edge vortices generated by flow separation from the leading-edge ice accretion. Type II flow fields lack the leading-edge spanwise vortex, which appears to be suppressed by streamwise vorticity resulting from highly 3D horns (scallop) and, in some cases, ice shapes with surface roughness added.
- For the limited number of leading-edge horn-ice shapes (including scalloped shapes) considered in this research, the aerodynamic results on the lower fidelity 3D smooth shapes based on the outermost surface geometry always generated nonconservative performance degradation as compared with the high-fidelity ice shapes. Three-dimensional ice features of the high-fidelity horn-ice configurations have an impact on the iced-wing flow field and resulting integrated performance.
- While Reynolds and Mach number effects are important for quantifying the clean-wing performance, there is very little to no effect for an iced wing with 3D, high-fidelity artificial ice shapes or 3D smooth ice shapes with grit roughness over the range tested.
- Preliminary computational aerodynamic studies for the CRM65 wing with one 3D smooth ice-shape configuration have accurately reproduced the experimental data and thus deserve further investigation.

## 1.0 Introduction

The purpose of this joint final report is to summarize the key results, findings, and contributions of a multiyear research effort aimed at swept-wing icing and aerodynamics. The Swept-Wing

Icing Project (SWIP), also known as SUNSET II<sup>1</sup>, was jointly sponsored by NASA, the Federal Aviation Administration (FAA), and Office National d'Etudes et de Recherches Aéropatiales (ONERA) and supported by Boeing, the University of Illinois, the University of Virginia, and the University of Washington. A significant amount of original research was conducted during the course of this project. Detailed results are presented in numerous references cited in this report; as such, these details are not presented here. This report focuses instead on what was learned as a result of this research.

## 1.1 Background and Motivation

The in-flight icing of aircraft has traditionally been addressed as a significant safety consideration long after the conceptual and preliminary aircraft design phases. In some cases, however, the current regulatory requirements can have a significant impact on aircraft configuration and sizing decisions during the earliest design stages (Ref. 1). There is increasing demand to balance tradeoffs in aircraft efficiency, cost, and noise that tend to compete directly with allowable performance degradations over an increasing range of icing conditions. As a result, there is a need to greatly improve both our understanding and our engineering simulation tools to advance the state of the art in aircraft research and development. NASA, the FAA, and ONERA conduct icing research to enable advanced airplane configurations designed to reduce fuel burn, carbon emissions, and noise while maintaining a sufficient level of flight safety. Icing research is also critical to emerging-market aircraft, such as urban air mobility (UAM) and electric aircraft.

Ice accretion and its aerodynamic effect on highly three-dimensional (3D) swept wings are extremely complex phenomena important to the design, certification, and safe operation of small and large transport aircraft. Computational fluid dynamics (CFD) codes have reached a level of maturity where they are being proposed by manufacturers for use in certification of aircraft for flight in icing, but high-quality, representative icing and aerodynamic data are required to evaluate the performance of computational icing simulation tools for iced swept wings. Without such data, it is difficult to determine how much confidence can be placed in results from CFD codes used in design, and particularly in certification. At the outset of this project, sufficient data were not available in the public domain.

An understanding of the icing effects on swept-wing aerodynamics is critical to evaluating the accuracy to which ice accretion must be predicted by computational tools or simulated

in aerodynamic testing. For example, it is known for some cases that swept-wing ice accretion can be highly 3D (e.g., “scallops” or “lobster tails”), as shown in Figure 1. An important question is how much detail of that three-dimensionality is critical to the aerodynamic performance and must therefore be accurately simulated. Uncertainties as to the impact of ice accretion on aerodynamics can lead to highly conservative designs which, in turn, can adversely affect critical parameters such as fuel burn, approach and landing speeds, and aircraft weight. In addition, basic swept-wing aerodynamic effects such as spanwise flow and configuration dependence play an important role and affect the ability to make general conclusions. An understanding of scale effects, including Reynolds and Mach number effects, is needed to develop lower cost aerodynamic test techniques for iced swept wings. Wind tunnel tests conducted at smaller geometric scale and lower Reynolds number hold potential for developing a more complete understanding of the aerodynamics. Both full-scale and subscale research is needed to develop and validate CFD simulation tools used to predict the aerodynamics of iced-wing configurations. All of these factors have provided motivation for a collaborative research effort in this arena.

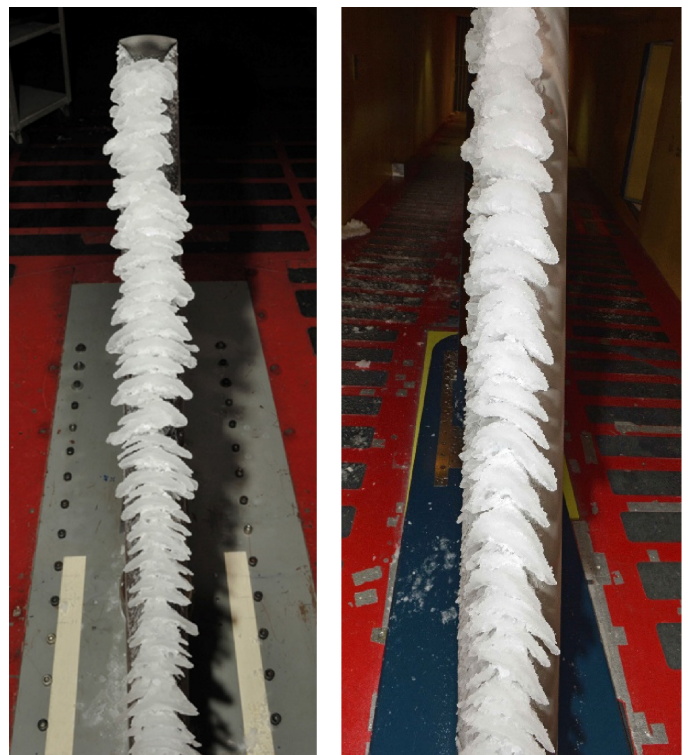


Figure 1.—Examples of highly 3D swept-wing ice accretion, referred to as “scallops” or “lobster tails.”

<sup>1</sup>The Swept-Wing Icing Project was modeled after an earlier ice-accretion aerodynamics study named “StUdies oN Scaling EffecTs due to ice,” or SUNSET (later referred to as SUNSET I).

## 1.2 Iced Airfoil Aerodynamic Simulation SUNSET I

This research effort was modeled after SUNSET I, a successful international collaboration that investigated aerodynamic effects and ice-accretion simulation for airfoils and straight wings (Refs. 2 to 20). The overall goal of the previous collaboration was to provide high-fidelity, full-scale iced-airfoil aerodynamic data and validated subscale-model simulation methods that produce the essential full-scale aerodynamic characteristics. The research was organized into six phases and involved icing wind tunnel and aerodynamic wind tunnel experiments with both subscale and full-scale models using the National Advisory Committee for Aeronautics (NACA) 23012 airfoil. An important initial step in this research was the classification of ice accretion according to the aerodynamic effect on the flow field. This provided a framework within which the ice-accretion and aerodynamic testing was conducted. The NASA Icing Research Tunnel (IRT) was used to generate the ice accretion using both subscale and full-scale models. Aerodynamic testing was performed at the ONERA F1 pressurized wind tunnel using a 72-in. (1.83-m) chord, full-span, unswept NACA 23012 airfoil model with high-fidelity 3D castings of the IRT ice accretions. Performance data were recorded over a large range of Reynolds number, from  $4.5 \times 10^6$  to  $15.9 \times 10^6$ , and a Mach number range of 0.10 to 0.28. This generated a large, high-quality, benchmark iced-airfoil aerodynamic database. Lower fidelity simulation methods were developed and tested on an 18-in. (0.46-m) chord NACA 23012 airfoil model at the University of Illinois wind tunnel at lower Reynolds number. The aerodynamic accuracy of the lower fidelity subscale ice simulations was validated against the full-scale results for a factor of 4 reduction in model scale and a factor of 8 reduction in Reynolds number. Methods were developed for designing lower fidelity artificial ice shapes for subscale models. The completed research defined the level of geometric fidelity required for artificial ice shapes to yield aerodynamic performance results to within a known level of uncertainty. This previous work has led to a more complete understanding of ice contamination aerodynamic effects on airfoils. This is an important building block, but a fundamental question remained as to how relevant these two-dimensional (2D) data are to 3D swept-wing geometries.

### 1.3 Goal, Objectives, and Approach

The overall goal of this research effort was to improve the fidelity of experimental and computational simulation methods

for swept-wing ice-accretion formation and resulting aerodynamic effect. There were three specific objectives:

1. Generate a database of 3D swept-wing ice-accretion geometries for icing-code development and validation and for aerodynamic testing.
2. Develop a systematic understanding of the aerodynamic effect of icing on swept wings, including Reynolds and Mach number effects, important flow-field physics, and fundamental differences from 2D geometries.
3. Determine the effect of ice-shape geometric fidelity on aerodynamic simulation of swept-wing icing effects.

A seven-phase research effort was designed that incorporates ice-accretion and aerodynamic experiments and computational simulations to address these objectives. This is depicted schematically in Figure 2. Phase I was a review of the technical literature associated with iced swept-wing aerodynamics with emphasis on classifying ice accretion based upon key aerodynamic features of the flow field. The research conducted in Phase II identified the baseline swept-wing model to be used for the experiments and computational analysis. In addition, measurement techniques were developed to document, in 3D, the experimental ice-accretion geometries. Aerodynamic measurement techniques suitable to iced swept-wing experiments were also investigated. The icing tests conducted in Phase III generated a large database of ice-accretion geometries on realistic large-scale swept-wing section models. Artificial ice shapes of varying geometric fidelity were then developed for aerodynamic testing over a large Reynolds number range in Phases IV and V. Exploring the effects of geometric fidelity and Reynolds number required final validation tests that were carried out in Phase VI. The research conducted in Phase VII explored the use of computational simulation tools for ice accretion and aerodynamics on swept wings. The work conducted in each phase is summarized in the next section of this report.

## 2.0 Project Description

This section summarizes the technical challenges and the research conducted in each of the seven phases illustrated in Figure 2. The details of this work and corresponding results can be found in the references cited herein. This section is based, in part, upon a 2013 paper by Broeren et al. (Ref. 21) that was written at the outset of this project. A companion summary of this project was written in 2017 by Potapczuk and Broeren (Ref. 22).

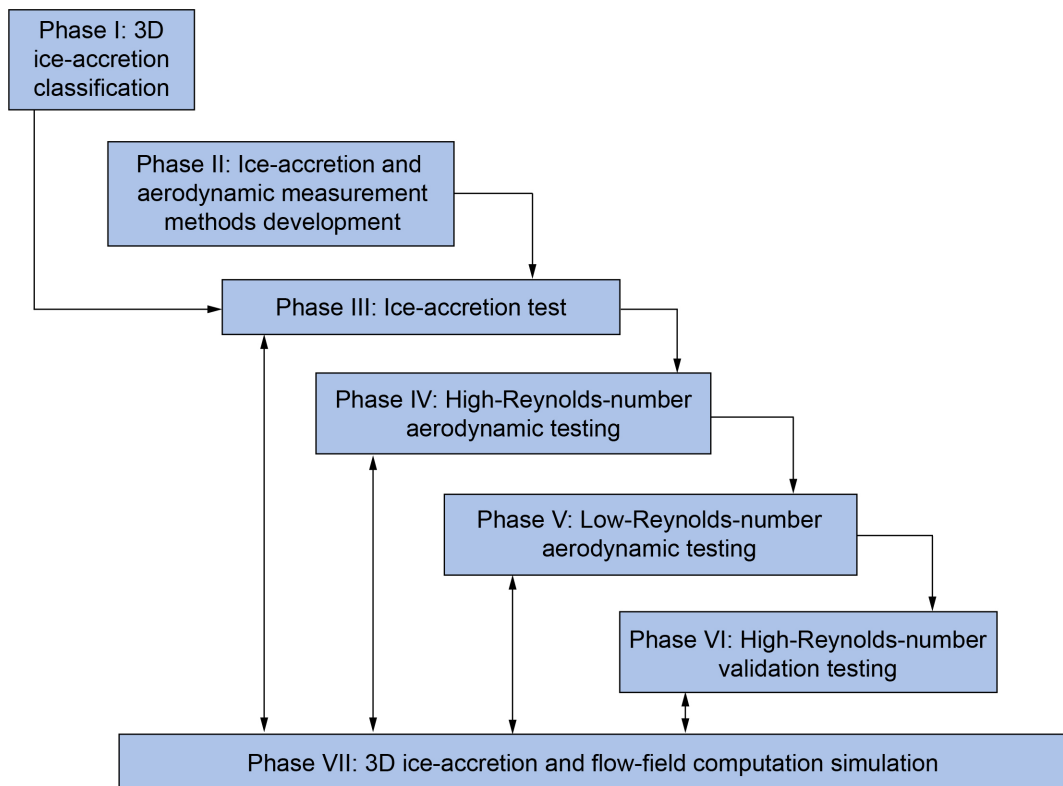


Figure 2.—Seven-phase research effort designed to investigate large-scale swept-wing ice accretion and aerodynamics.

## 2.1 Phase I: 3D Ice-Accretion Classification

Ice accretion is often described in terms of its appearance or composition: glaze, rime, clear, mixed, runback, beak, and intercycle, among others. This terminology can be useful for characterizing the visual attributes of ice accretion, but it is less helpful when the objective is to understand the aerodynamic effects. Bragg, Broeren, and Blumenthal (Refs. 4 and 5) examined the icing aerodynamics literature and developed four fundamental types, or categories, of ice accretion based upon the flow-field physics unique to each: (1) roughness, (2) horn ice, (3) streamwise ice, and (4) spanwise-ridge ice. This research was directed at the essentially 2D aspects of iced airfoils. Categorizing ice accretion in this way provided an aerodynamic framework for the research designed to quantify the effects of geometric fidelity on iced-airfoil aerodynamics. This proved to be a successful approach and was identified as an important part of the swept-wing icing research effort.

At the outset of this project, a small number of aerodynamic studies for iced swept wings were found in the public domain. In 1989, a fundamental study of the flow field on a subscale rectangular swept wing using a NACA 0012 airfoil section was conducted with a simulated glaze-ice accretion (Refs. 23 to 26). The 3D velocity measurements on the iced wing were

complemented with CFD simulations to develop a good understanding of the ice-shape effect on the flow field. In 2001, a research program involving the FAA, NASA, and Wichita State University (WSU) was conducted to develop an experimental database of ice-accretion effects on aerodynamic performance of a finite swept wing (Refs. 27 to 29). An icing test was conducted in the IRT on a subscale wing having a 28° sweep and GLC-305 airfoil section. High-fidelity ice-casting simulations were generated for aerodynamic testing in the WSU 7- by 10-ft wind tunnel at a Reynolds number of  $1.8 \times 10^6$ . Although this study utilized high-fidelity artificial ice shapes, the small model scale and low Reynolds number limit the applicability of the results to a full-scale airplane. Reehorst et al. (Refs. 30 and 31) also conducted a low-Reynolds-number aerodynamic study of icing effects on a realistic, fully 3D, 12.5-percent-scale model of a twin-engine, short-haul commercial transport. The authors considered various roughness-size scaling approaches for the small-scale and low-Reynolds-number investigation. Despite the low Reynolds number at which the data were acquired, this effort resulted in a large database of icing effects on a full-aircraft configuration. Aerodynamic testing of a full-scale swept-wing business jet T-tail model was performed under the auspices of the NASA/FAA Tailplane Icing Program, Phase II (Refs. 32 and 33). While the

T-tail model results are generally applicable to the swept-wing icing aerodynamics research described here, no highly 3D ice-shape configurations (such as scallop shapes) were tested.

Broeren, Diebold, and Bragg (Ref. 34) and Diebold, Broeren, and Bragg (Ref. 35) prepared extensive reviews of the preexisting data on swept-wing ice accretion and aerodynamics. The preexisting data tend to be (1) mostly at small scales, (2) at low Reynolds number, and (3) applicable to simple swept-wing geometries that do not have the characteristics typical of modern-design, large-scale commercial transport wings. Given what was known from the preexisting data, the same four classifications or fundamental categories used for iced airfoils were suggested: (1) roughness, (2) horn ice, (3) streamwise ice, and (4) spanwise-ridge ice. Instead of relying upon ice-accretion terminology such as rime and glaze, the four aerodynamic groups have names associated with ice-shape geometry. Based upon the results of the present study, it was found that these proposed classifications were generally applicable to the iced swept-wing aerodynamics but that an additional distinction was needed for leading-edge horn ice resulting in 3D leading-edge horn ice and highly 3D leading-edge horn ice. This is one of the key results and findings documented in Section 3.3 and in a paper by Bragg et al. (Ref. 36).

## 2.2 Phase II: Ice-Accretion and Aerodynamic Measurement Methods Development

The research conducted in Phase II provided the necessary foundation for the experimental and computational work conducted in the later phases. The Phase II research was organized into three areas:

1. Defining the baseline, full-scale, swept-wing model geometry to be used for the research effort
2. Developing and validating methods to measure highly 3D ice accretion
3. Developing the appropriate measurement methods to quantify the iced swept-wing aerodynamics

The work conducted in each of these areas is summarized here.

### 2.2.1 Baseline Model Selection

For this research to be useful and relevant, it was important to select a baseline swept-wing model geometry that is representative of current modern-design commercial transport airplanes. The selection process was complex given the large number of variables, such as sweep angle, aspect ratio, mean aerodynamic chord, and wingspan. An additional requirement was for the geometry to be nonproprietary and non-export-controlled. After a review of available options, the Common

Research Model (CRM) geometry was selected (Ref. 37). Boeing had provided the design of the CRM for a previous joint experimental effort with NASA that fabricated test articles and conducted aerodynamic testing (Refs. 38 and 39). The CRM geometry was also used as part of the American Institute of Aeronautics and Astronautics (AIAA) Drag Prediction Workshops (Ref. 40). The CRM, shown in Figure 3 with and without the engine nacelle/pylon, has a fuselage representative of a wide-body commercial transport airplane. Table I provides a comparison of the CRM wing geometry with existing wide-body airplanes. A key advantage in using the CRM is that all of the geometry information, CFD analysis, and experimental data are available in the public domain. Coupled with the CRM's modern design, this made the CRM an ideal baseline reference model for this research.

Because the CRM was designed to be representative of a wide-body transport airplane, its physical size is very large compared with that of many other swept-wing airplanes, such as single-aisle commercial transports, including regional and business jets. The large physical size of the CRM wing presents specific challenges to both the ice-accretion and aerodynamic testing. Applying icing scaling techniques for the CRM wing would be challenging, and thus ice-accretion tests on full-scale models were more desirable for this research. Due to the limited sizes of icing wind tunnels, large-scale wing ice-accretion testing requires the design of hybrid or truncated models where the full-scale leading-edge geometry is matched to a redesigned afterbody. This design process is the subject of Phase III of the research effort described in Section 2.3. The large physical size of the CRM wing requires a very aggressive design for the hybrid model that presents greater risk of adverse effects (such as tunnel wall boundary-layer separation) when installed in the IRT. For aerodynamic wind tunnel testing, the full-scale CRM wing can be scaled to an appropriate size for the facility. In the case of the ONERA F1 wind tunnel (described in Sec. 2.4), an 8-percent-scale model of the CRM would be of appropriate size. While this is not unreasonable for the clean baseline model geometry, such a large reduction in scale becomes challenging when the goal is to accurately simulate ice-accretion geometry that typically includes small roughness. Typical ice-roughness sizes on the full-scale model ice accretion could be in the range of 0.04 to 0.08 in. (1 to 2 mm), which is equivalent to 0.003 to 0.006 in. (0.08 to 0.16 mm) on the 8-percent-scale aerodynamic model. Small roughness features of this size are very challenging to accurately reproduce on the artificial ice shapes developed for aerodynamic testing. Based upon these factors, the research team decided to use a 65-percent-scale version of the CRM as the full-scale baseline reference geometry for this research. Table II provides a comparison of the CRM65 geometry with that of existing single-aisle commercial transport airplanes. The geometries are similar in scale, with only the

CRM65 sweep angle being considerably larger. More detailed geometry information for the CRM65 wing semispan is shown in Figure 4. Using the CRM65 as the full-scale baseline

reference geometry for this research reduces potential risks associated with the ice-accretion and aerodynamic testing while still being representative of current transport airplanes.

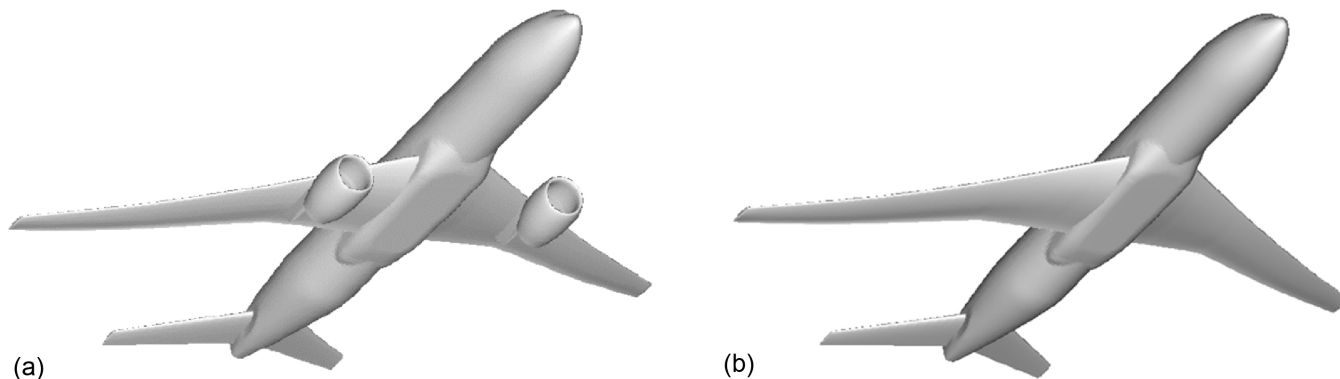


Figure 3.—Conceptual design of Common Research Model with and without engine nacelle/pylon, after Vassberg et al. (Ref. 37).

TABLE I.—COMPARISON OF CRM WING GEOMETRY WITH EXISTING WIDE-BODY AIRPLANES<sup>a</sup>

Airplane	Span, ft	Mean aerodynamic chord, ft	Area, ft <sup>2</sup>	Aspect ratio	Taper ratio	Sweep angle, c/4
CRM	192.8	23.0	4,130	9.0	0.28	35°
Airbus A330–200/300	198.0	23.9	3,892	9.5	0.22	30°
Boeing 777–200	199.9	26.5	4,389	8.7	0.27	31°
Boeing 787–9	197.0	20.6	3,880	9.6	0.18	32°
Boeing 747–400	211.4	29.8	5,417	7.7	0.28	37°

<sup>a</sup>Data for existing wide-body airplanes were compiled from publicly available sources that may use different conventions to define the geometric parameters.

TABLE II.—COMPARISON OF CRM65 WING GEOMETRY WITH EXISTING SINGLE-AISLE AIRPLANES<sup>a</sup>

Airplane	Span, ft	Mean aerodynamic chord, ft	Area, ft <sup>2</sup>	Aspect ratio	Taper ratio	Sweep angle, c/4
CRM65	125.3	15.0	1,745	9.0	0.28	35°
Airbus A320	112.0	14.1	1,320	9.5	0.21	25°
Boeing 737–800	112.6	13.0	1,341	9.5	0.16	25°
Boeing 757–200	124.8	16.7	1,847	7.8	0.21	25°

<sup>a</sup>Data for existing single-aisle airplanes were compiled from publicly available sources that may use different conventions to define the geometric parameters.

#### CRM65 wing geometry

- Semispan = 62.7 ft
- Root chord (symmetry plane) = 29.0 ft
- Root chord (fuselage side of body) = 25.4 ft
- Tip chord = 5.8 ft
- Mean aerodynamic chord = 15.0 ft
- Semispan area = 873 ft<sup>2</sup>
- Aspect ratio = 9.0
- Taper ratio = 0.28
- Sweep angle ( $c/4$ ) = 35°

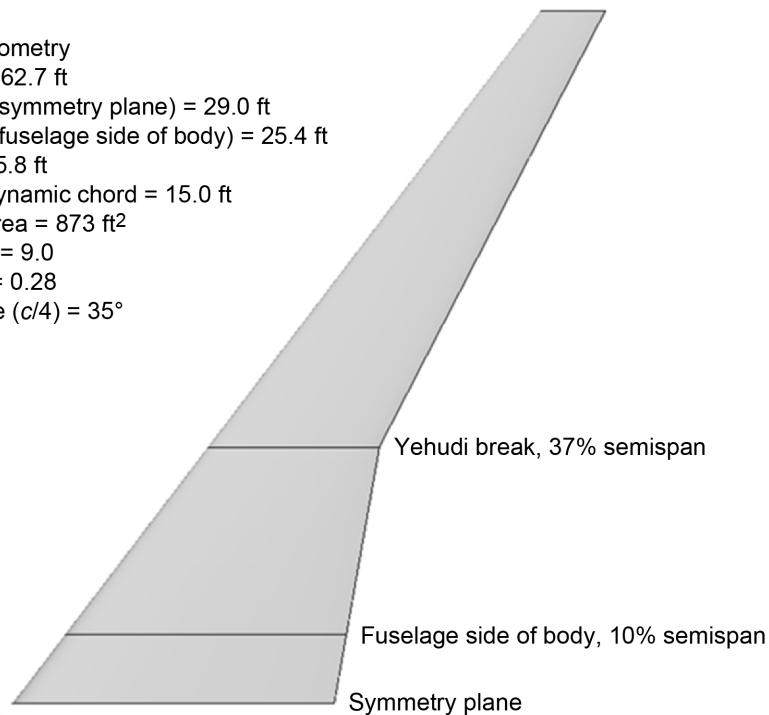


Figure 4.—Summary of CRM65 wing geometric characteristics, adapted from Vassberg et al. (Ref. 37).

### 2.2.2 3D Ice-Accretion Measurement

Generating a database of 3D experimental ice-accretion geometries and associated artificial ice shapes for subsequent aerodynamic testing required a robust measurement system that did not exist at the outset of this project. Standard ice-accretion documentation methods available at that time were generally 2D, such as cross-sectional tracings, or qualitative, such as photographs. Although these methods have been used for many years, they have significant shortcomings when used for the potentially highly 3D ice accretions that can occur on swept wings (Figure 1). Prior to this research effort, the best technology for capturing 3D features of ice accretion was the mold and casting method. This has been used for many years with various materials and was improved at NASA Glenn during the 1980s using more robust materials to improve accuracy and durability (Ref. 41), but a significant disadvantage to this method is that there is no digitized record of the ice accretion. A method to accurately and efficiently digitize ice accretion in 3D was needed, along with the capability to process and archive the data so that (1) comparisons to ice-accretion code results can be performed, (2) artificial ice shapes can be readily fabricated at appropriate geometric scales for aerodynamic testing, and (3) the geometry may be readily adapted for CFD simulations.

Lee et al. (Ref. 42) describe the effort to adapt commercial laser-based scanning methods to quantify the full 3D features

of ice accretion in the IRT. Demonstration tests of several different scanning systems and software were conducted in the IRT and evaluated against a set of predefined criteria. It was found that the scanning technology and capability was similar over the range of systems evaluated. An articulated-arm-based system, as shown in Figure 5, was selected because it required minimal modifications to the existing IRT test section, resulting in fewer risks during use, such as potential changes to the accreted ice.

Several different software packages were considered for postprocessing of the data. The processing steps included combining individual scans, developing a surface mesh, and filling holes or gaps in the scan data. The most critical software function for working with ice-scan data is the ability to create closed, watertight surfaces of the highly irregular, rough features of ice accretion. Through a series of demonstration tests, it was determined that the Geomagic Wrap<sup>®</sup> software package, now owned by 3D Systems, has the capability to process irregular organic surfaces like those typical of ice accretion. The software is also able to create data files that can be used for various rapid prototyping manufacturing methods. Such methods can be used to fabricate artificial ice shapes from the scan data. The software also has exact surfacing capability that can be used to develop grids for computational analysis.



Figure 5.—Arm-based 3D laser scanning system used to measure ice accretion in NASA Icing Research Tunnel.

The scanner system validation research was divided into two parts: one for straight-wing ice shapes and the other dedicated to swept-wing ice shapes, as detailed in References 43 to 47. For the straight-wing ice shapes, an aerodynamic validation was conducted. Ice-accretion testing was performed and measured with the scanning system. A mold was also made of the same ice accretion. Artificial ice shapes were subsequently fabricated using the casting method from the molds and from rapid prototyping methods based upon the 3D scan data. These artificial ice shapes were mounted to the leading edge of an airfoil model for aerodynamic testing. The results demonstrated comparable aerodynamic effects from the two sets of artificial ice shapes. The validation for swept-wing ice shapes included a geometric comparison between the 3D laser scan data and 3D data obtained from commercial x-ray computed tomography (CT) scanning. A significant challenge associated with swept-wing ice accretion is obtaining scan data within highly 3D features such as scallops and lobster tails. The arm-based, laser-scanning system uses a line-of-sight method that cannot acquire

data within small surface gaps. In this case, more manual intervention during postprocessing is required to create closed or watertight surfaces. Data from the non-line-of-sight CT scanning method were used to evaluate the accuracy of the laser-based system and postprocessing for highly 3D ice geometries (Ref. 44).

### 2.2.3 Aerodynamic Measurement Methods

An aerodynamic framework for classifying swept-wing ice accretion based upon unique flow-field features was described in Section 2.1. Identifying these flow-field features and their contribution to the resulting aerodynamic performance degradation was key to satisfying the objectives of this research effort as described in Section 1.3. In addition to analyzing standard performance data such as lift, drag, and pitching moment, it was important to understand the characteristics of the flow field that drive the changes in performance. Flow-field information is also required for the continued development and validation of computational simulation tools. Thus, measurement

methods designed to obtain flow-field information on an iced swept wing were investigated.

The development of these methods was carried out at small scale and very low Reynolds number at the University of Illinois. Diebold et al. (Refs. 48 to 51) describe the application of pressure-sensitive paint and wake survey techniques to iced swept wings. These experiments were conducted on an approximately 2-percent-scale modified CRM wing model with an artificial leading-edge ice shape. These methods have been investigated by many researchers and are well established. What was unique in this case were the potential challenges presented by the complexities of an iced swept-wing flow field. For airfoils, it was found that the addition of artificial ice geometries often resulted in large-scale unsteady, 3D, and separated flow. Such situations can challenge the implementation and interpretation of results from the selected measurement methods.

The experiments with pressure-sensitive paint were considered to be successful, especially when combined with surface oil flow visualization results. The surface pressure data made it possible to quantify the 3D flow separation features observed in the oil flow patterns. These results were very encouraging, given the known challenges associated with pressure-sensitive paint measurements at low dynamic pressure. Ultimately it was decided not to continue the pressure-sensitive paint measurements into Phases IV to VI of this research effort. As described later in this report, the wind tunnel models were built with over 200 conventional surface static pressure taps. It was determined that sufficient surface pressure data would be obtained from these pressure taps, and thus more effort was focused on the wake survey measurements.

The wake flow-field surveys were conducted using a five-hole pressure probe to yield total and static pressure in addition to all three velocity components (Refs. 50 and 51). Further analysis of the velocity data led to contour plots of wake vorticity. These data were carefully aligned to surface oil flow visualizations to elucidate separated flow regions on the wing. The quantitative wake data proved to be very useful in corroborating qualitative flow-field observations deduced from the surface oil flow visualizations. The wake data were also integrated to yield spanwise distributions of lift, profile drag, and induced drag for the clean and iced wing configurations. During the Phase II investigations of the wake survey methods, it was thought that the spanwise distributions of lift and drag could provide much-needed insight into the iced-wing aerodynamics, and the wake survey method was therefore implemented in the Phase V research. As described later in Section 2.4.5, the acquisition of these data proved to be very time consuming and thus was limited to a small number of configurations. It was also found that the spanwise distributions

of lift and drag did not significantly improve the understanding of iced-wing aerodynamics.

## 2.3 Phase III: Ice-Accretion Testing

The ice-accretion testing conducted in Phase III provided a database of ice-accretion geometry that was used for comparison to icing code results and for the creation of artificial ice shapes for aerodynamic testing. The ice-accretion testing was performed using swept-wing model sections of the CRM65 wing. The wing section models were of a hybrid design where the full-scale leading edge was maintained only to a certain percentage of the local chord while the aft section of the model was redesigned into a shortened aft section. This approach was needed because of the large size of the CRM65 wing. The local chord lengths, even on the outboard portions of the wing, were much larger than typical icing wind tunnel models. The Phase III research was organized into four areas:

1. Selection of airplane missions and simulation of icing conditions
2. Design of hybrid model wing sections for the IRT
3. Ice-accretion testing
4. Posttest comparison of experimental and computational ice shapes

The work conducted in each of these areas is summarized here.

### 2.3.1 Selection of Airplane Missions and Simulation of Icing Conditions

A set of icing mission scenarios that were typical of large commercial transport airplanes was defined. Climb, hold, and descent phases of flight were included. The selection of airplane weights, flight speeds, altitudes, and angles of attack for each flight phase was appropriate for an airplane of the CRM65 class. The selected icing conditions (drop median volumetric diameter (MVD), cloud liquid water content (LWC), and temperature) were based upon the Continuous Maximum envelope defined by Title 14, Code of Federal Regulations (CFR), Part 25, Appendix C (hereafter referred to as “App. C”). Further details regarding the mission scenarios and corresponding icing conditions are described by Fujiwara et al. (Refs. 52 and 53).

The large matrix of flight and icing conditions was reviewed, and several scenarios were selected for further analysis. This subset of icing scenarios provided for a range of ice-accretion shapes on the full-scale airplane while significantly reducing the workload associated with analyzing all cases. Flow simulations were performed at each of the selected flight conditions using the 3D Reynolds-averaged Navier–Stokes (RANS) code OVERFLOW (Ref. 54) version 2.2k, thus generating a large

database of flow-field information for the clean flight baseline (CFB) of the CRM65 airplane. The flow-field solution was used as input to the LEWICE3D (Ref. 55) ice-accretion prediction code to generate ice-shape results for the corresponding flight conditions. Some results are shown in Figure 6 and Figure 7 for a flight condition at 10,000-ft altitude, speed = 232 kn, static temperature =  $-4\text{ }^{\circ}\text{C}$ , airplane angle of attack =  $3.7^{\circ}$ , drop MVD =  $20\text{ }\mu\text{m}$ , cloud LWC =  $0.55\text{ g/m}^3$ , and an exposure time of 45 min. The contours of local collection efficiency in Figure 6 show the location of water impingement on the nose section of the fuselage and wing leading edge. The closeup view near the

wing tip illustrates the regions of highest local collection efficiency. Figure 7 depicts the LEWICE3D-generated ice shapes at several locations along the span of the wing. Closeup views are shown near the wing root and tip sections. LEWICE3D calculates ice growth along the wing sections perpendicular to the leading edge. For this case, the predicted ice shape is a large upper-surface horn. Results of this type were generated for all of the icing cases selected for analysis. Collectively, these results were called the iced flight baseline (IFB) and were informally referred to as the “gold standard” because they were considered to represent the full-scale airplane flight ice shapes.

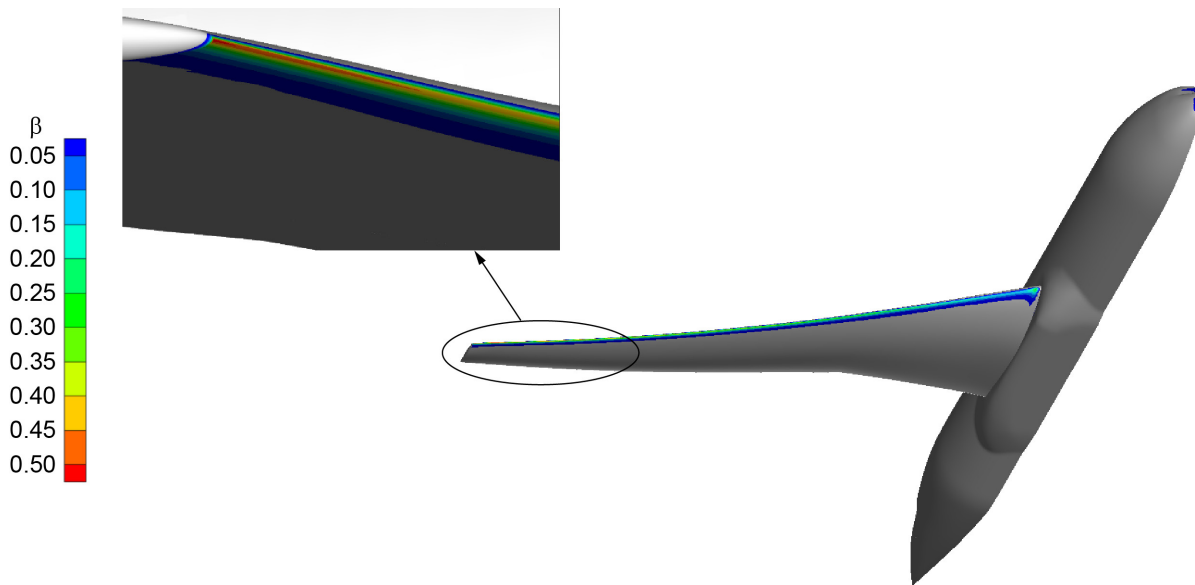


Figure 6.—LEWICE3D local collection efficiency  $\beta$  results for CRM65, MVD =  $20\text{ }\mu\text{m}$ , speed = 232 kn, altitude = 10,000 ft.

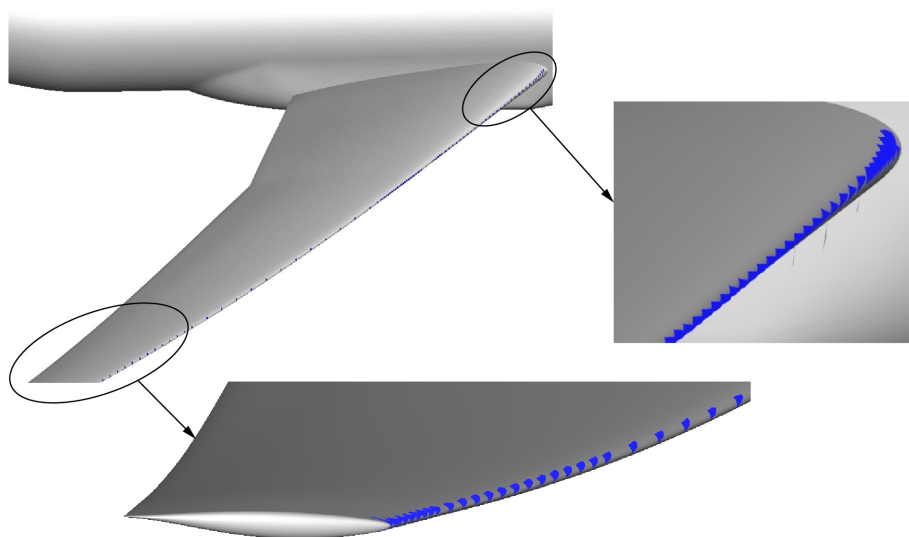


Figure 7.—LEWICE3D ice-shape results for CRM65, MVD =  $20\text{ }\mu\text{m}$ , speed = 232 kn, altitude = 10,000 ft, LWC =  $0.55\text{ g/m}^3$ , static temperature =  $-4\text{ }^{\circ}\text{C}$ , 45-min exposure.

The LEWICE3D results were analyzed to understand the spanwise variation in the predicted ice geometry. The maximum thickness of the ice and the angle associated with that maximum thickness location were calculated along the span of the wing (Ref. 53). These parameters are commonly referred to as “ice-horn thickness” and “ice-horn angle.” A major outcome of this analysis was the selection of the spanwise locations to be used for the hybrid model designs. Determining the number of spanwise locations to select required a balance of competing factors. In this research effort, each of the selected locations was used as the basis for the design of a hybrid swept-wing model to be constructed and tested in the IRT. Selecting a large number of spanwise locations provides the highest fidelity representation of the ice accretion along the entire wing, but practical considerations of time and resources limit the total number that can be successfully constructed and tested in the IRT. Ultimately it was decided that selecting three spanwise stations for further analysis provided a reasonable balance of the competing factors.

The selection of three spanwise stations was also driven by the expectation that these stations would be located near the (1) root, (2) midspan, and (3) tip. The section near the wing root, or Inboard station, was selected to be at 20-percent semispan because this corresponded to the minimum ice-horn angle for nearly all of the icing cases analyzed. The Midspan station was selected to be at 64-percent semispan because this corresponded to the maximum ice-horn angle for at least one of the icing cases analyzed. The section near the tip, or Outboard station, was selected to be at 83-percent semispan. This location approximates the outboard extent of the wing leading-edge ice protection system in some cases, making the icing characteristics significant. This location is also about halfway

between the 64-percent semispan station and the wing tip. These three wing stations are shown graphically in Figure 8. The wing sections were taken perpendicular to the leading edge to be consistent with the LEWICE3D ice-shape results.

### 2.3.2 Design of Hybrid Model Wing Sections for IRT

A hybrid model design approach was required for this research because of the large size of the wing sections relative to the size of the IRT test section. The dimensions of the IRT test section are 6 ft high by 9 ft wide by 20 ft long, whereas the streamwise chord length of the wing sections shown in Figure 8 ranged from 8.3 ft at the 83-percent semispan station to 21.7 ft at the 20-percent semispan station. The design of hybrid models for icing tests where the full-scale leading-edge geometry is combined with a truncated, aerodynamically tailored afterbody has been explored by Saeed et al. (Refs. 56 to 58). Past research was conducted primarily for 2D wing sections and for moderate model sizes that did not require special consideration of tunnel wall interference effects. In the current effort, these 2D design methods were adapted to the swept-wing geometry and extended to include the effects of the tunnel walls on the large-blockage-model flow field. A single-element slotted flap was also added to the hybrid model design at this stage. The flap was required to accommodate matching the leading-edge flow conditions (e.g., attachment line location) over the angle-of-attack range defined for the icing mission scenarios. The objective of the hybrid design approach was to produce ice shapes on the hybrid models in the IRT that were accurate representations of the gold-standard IFB ice shapes. Accomplishing this objective was entirely dependent upon the use of computational simulation tools.

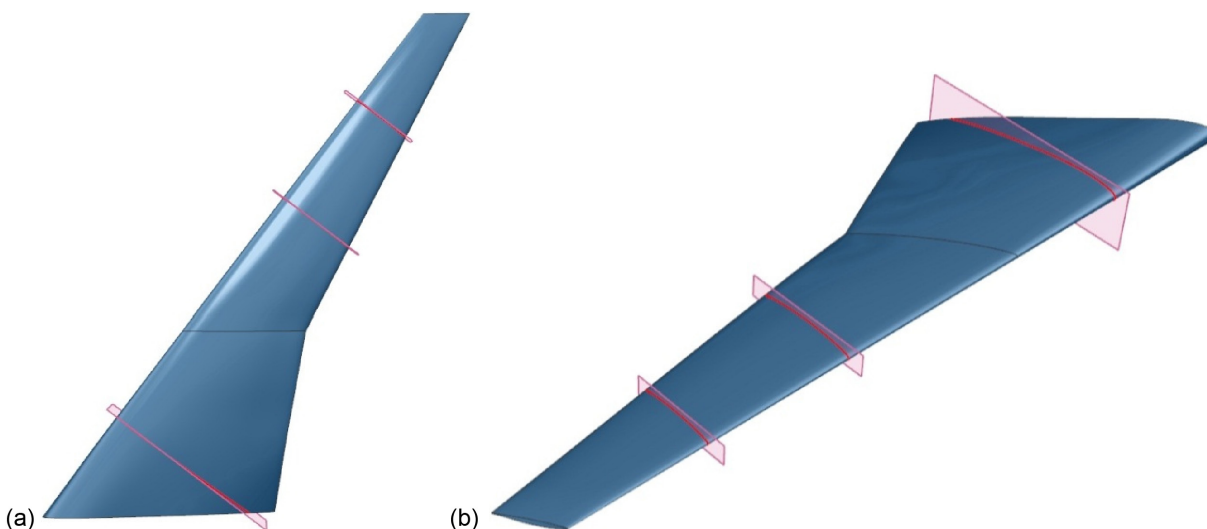


Figure 8.—Rendering of CRM65 wing showing selected hybrid model design stations at 20-, 64-, and 83-percent semispan (Ref. 53).

In simple infinite-swept-wing theory, the flow at a spanwise wing station is approximated by the flow about the leading-edge-normal airfoil section at the appropriate 2D Mach number and angle of attack. Since 2D hybrid airfoil design methods are relatively well developed, the first step in the swept-wing wind tunnel model design process took advantage of these 2D tools to produce a representative 2D hybrid airfoil (Refs. 52, 53, and 59 to 61). The 2D hybrid airfoil sections were extended and swept to create the 3D models for testing in the IRT (Refs. 62 and 63). Consistent with infinite-swept-wing theory, these models had zero twist and zero taper, greatly simplifying the design and construction. In the IRT testing, each 3D hybrid model (Inboard, Midspan, and Outboard) was used to generate the ice accretion found at one spanwise station of the full-scale swept wing. A summary of the hybrid model design characteristics is shown in Table III for all three models. The hybrid and full-scale airfoil section coordinates are plotted in Figure 9 to Figure 11. These plots show that each section included the local geometric angle of attack according to the wing twist distribution corresponding to airplane angle of attack equal to zero degrees. Therefore, only the airplane angle of attack needed to be specified to obtain the proper local angle of attack for each model.

The 3D hybrid model designs were checked using 3D simulation tools (Refs. 53 and 64 to 67). This analysis included 3D RANS flow simulations along with LEWICE3D icing simulations. The flow simulations were conducted to evaluate

the effect of the test-section walls, the resulting flow separation, and its impact on the hybrid model aerodynamics. The flow simulations were also used to optimize the flap deflection necessary to match the attachment line location to the corresponding CFB scenario. With the proper flap deflection identified, the LEWICE3D simulations then provided droplet impingement and ice-shape information for comparison with the IFB results generated earlier. The acceptance criteria for the final hybrid model design were based upon a number of comparisons. These comparisons were based purely on the results of 3D RANS flow-field simulations and LEWICE3D icing simulations performed for both the CRM65 airplane flying the icing mission scenarios (CFB + IFB) and the hybrid models designs “flying” in the IRT at the same conditions (e.g., airspeed, temperature, pressure, MVD, and LWC). A set of results is shown in Figure 12 for the Outboard model and one icing condition. Over the course of the research, it was determined important to match the location of the hybrid model’s attachment line with that of the CRM65 CFB. In addition, the LEWICE3D-generated droplet impingement and ice shapes were compared for the hybrid model in the IRT and the CRM65 IFB, as illustrated in Figure 12. The result of the hybrid model design process was the main element and flap “outer mold line” geometry for each of the three models: the Inboard model at 20-percent semispan, the Midspan model at 64-percent semispan, and the Outboard model at 83-percent semispan.

TABLE III.—ICING RESEARCH TUNNEL MODEL GEOMETRY INFORMATION

	Inboard	Midspan	Outboard
CRM65 semispan location, percent	20	64	83
Full-scale (FS) normal chord, $c_{FS}$ , in.	297.9	122.7	91.3
FS streamwise chord, in.	260.3	135.7	100.7
Upper-surface FS leading-edge extent, $x/c_{FS}$	0.04	0.10	0.17
Lower-surface FS leading-edge extent, $x/c_{FS}$	0.06	0.10	0.15
Model scale factor, $c_{FS}/c_{Hyb}$	2.25	2.0	1.5
Hybrid model normal chord, $c_{Hyb}$ , in.	132.4	61.4	60.9
Hybrid flap normal chord, in.	32.7	15.1	15.0
Hybrid model streamwise chord, in.	161.8	74.6	74.0
Hybrid flap streamwise chord, in.	41.1	18.7	18.8
Upper-surface FS leading-edge extent streamwise, in.	15.0	15.4	19.5
Upper-surface FS removable leading-edge extent streamwise, in.	11.2	12.3	11.4
Lower-surface FS leading-edge extent streamwise, in.	22.4	15.4	17.2
Lower-surface FS removable leading-edge extent streamwise, in.	14.9	15.4	13.8

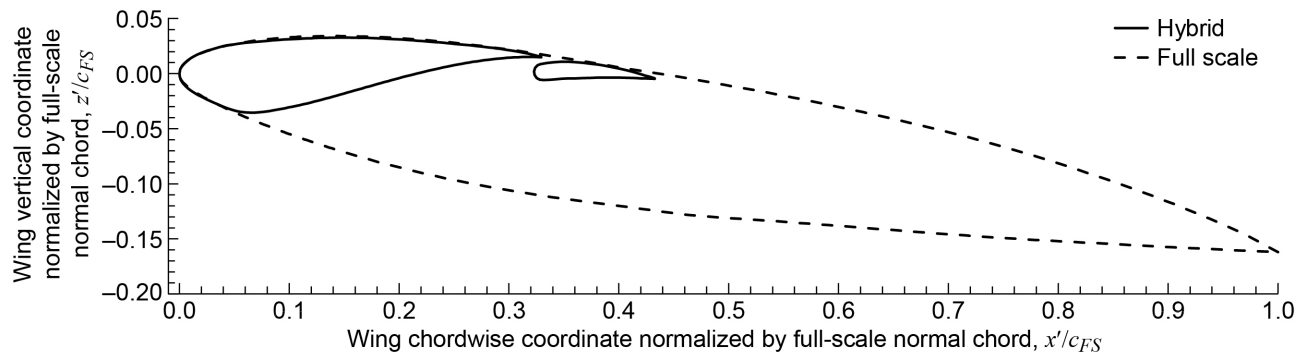


Figure 9.—Inboard model airfoil section (perpendicular to leading edge).

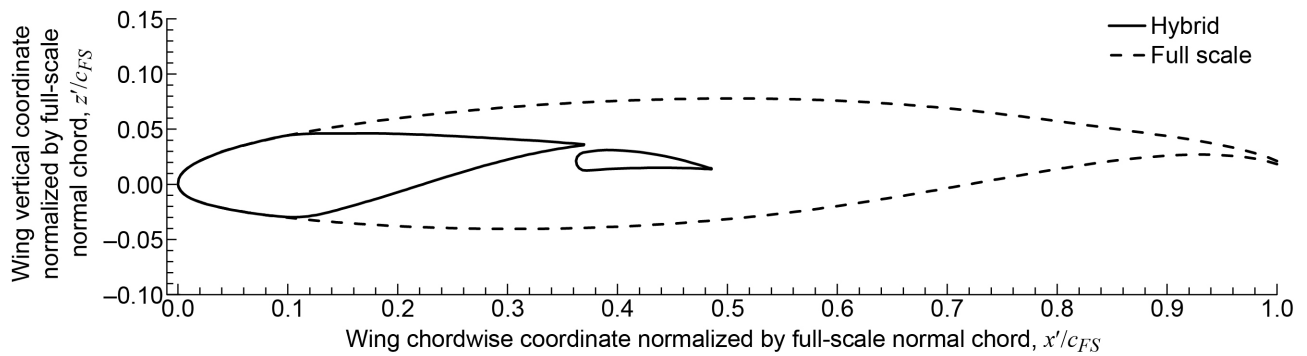


Figure 10.—Midspan model airfoil section (perpendicular to leading edge).

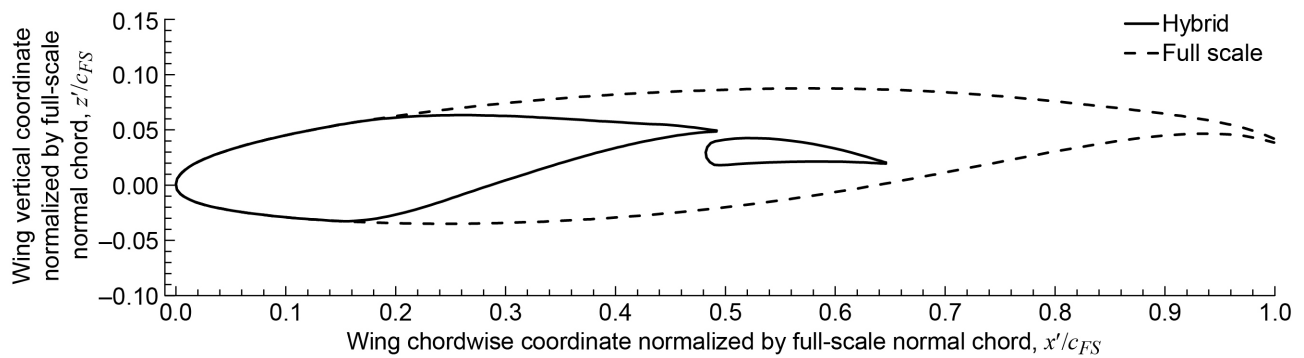


Figure 11.—Outboard model airfoil section (perpendicular to leading edge).

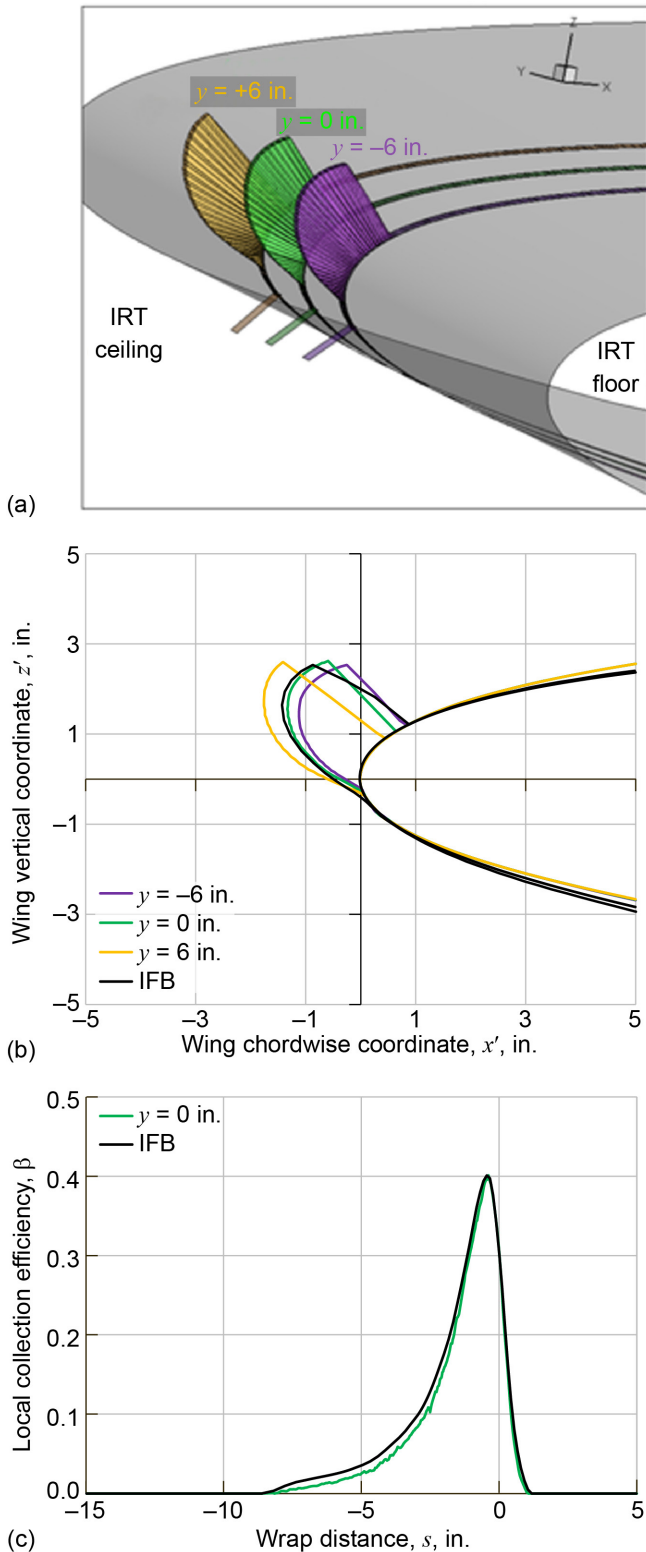


Figure 12.—Outboard model LEWICE3D simulations for case WB33  $T = -4$  °C,  $\alpha = 3.7^\circ$ ,  $\delta = 11^\circ$ , where  $y = 0$  corresponds to IRT test section vertical center, after Reference 53. (a) IRT ice shape. (b) IRT ice shape compared with iced flight baseline (IFB). (c) IRT collection efficiency compared with IFB.

### 2.3.3 Ice-Accretion Testing

Ice-accretion testing was carried out in the IRT. A complete description of the test program and results is provided in Reference 68. The IRT is a closed-return, refrigerated wind tunnel that simulates flight through an icing cloud at pressure altitudes near sea level. Temperature control is provided via an external refrigeration plant connected to a large heat exchanger located upstream of the settling chamber turning vanes. Downstream of the turning vanes are 10 spray bars, each with 55 possible nozzle positions. The airflow and water droplets are accelerated to the test section via a 14:1 contraction section. The test section is approximately 6 ft high by 9 ft wide by 20 ft long and has a calibrated speed range from 50 to 325 kn (empty). The available temperature range is from  $-40$  °C static to  $20$  °C total. The icing cloud is calibrated on a periodic basis and after any significant modification to the facility. Steen et al. (Ref. 69) describe the calibration that was used for the present test campaigns. Soeder et al. (Ref. 70) provide a more detailed description of the facility.

Each model was mounted vertically in the test section and spanned the entire height, as shown in Figure 13. Each model was composed of a main element, a single-element slotted flap, and a removable leading-edge section. Some details of the model geometries are shown in Table III, including the upper- and lower-surface extents of the full-scale leading edge. The main element and flap were instrumented with three streamwise rows of surface pressure taps located at spanwise stations 18, 36, and 54 in. above the test-section floor. Three thermocouples were installed inside the main element structure; these temperatures were monitored to ensure the model temperature was in equilibrium with the surrounding air. Each model had two different interchangeable leading edges. One leading edge was instrumented with pressure taps; the other was used for icing tests and thus had a completely smooth exterior surface. The removable leading edges were made from 0.090-in.-thick aluminum that was stretch formed to the desired airfoil coordinates and then hard anodized to improve the surface durability. For the icing leading edge, five thermocouples were located on the inside surface of the skin. Commercially available electrothermal heaters were also mounted to the inside surface of the icing leading edge. These heaters were only used to deice the leading edge after the ice accretion was fully documented.

The flap of each model had a motorized drive system with positioning feedback provided via a calibrated linear potentiometer. The flap control switch was located in the control room with the flap angle readout on the IRT Escort data system. The flap was also equipped with a custom-designed, anti-icing, electrothermal surface heater. It was important to the hybrid design that the flap aerodynamics not be compromised by any ice accretion. Twelve thermocouples were installed in various locations beneath the flap heater to monitor the skin temperature.

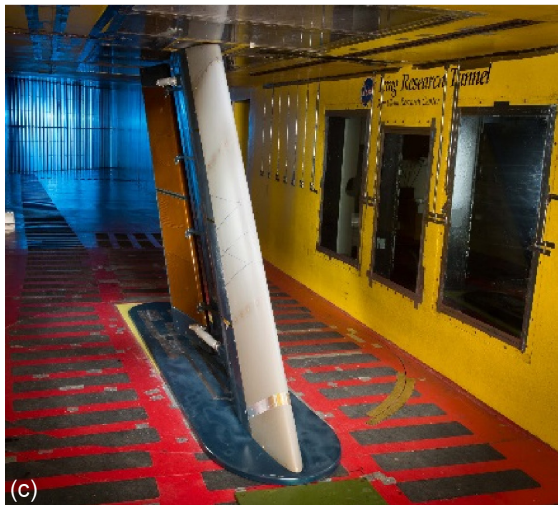


Figure 13.—Models installed in IRT test section. (a) Inboard model. (b) Midspan model. (c) Outboard model.

The models were tested in three separate test campaigns. Each model was initially installed in the IRT test section with the pressure-instrumented leading edge. The model surface pressures were measured over a large range of angles of attack and flap deflections. The pressure data were used to confirm that the aerodynamics were consistent with the 3D RANS CFD simulations performed during the design phase. In addition, the pressure data on the model leading edge were used to track the location of the attachment point at the spanwise station 36 in. above the test-section floor (test-section and model centerline). This was referred to as an “aerodynamic calibration,” or “aerocal.” The aerocal was used to ensure that the attachment point location on the hybrid IRT matched that of the CFB simulation results. This was considered to be of primary importance to matching the IRT model ice shape to the IFB configuration. The pressure data are presented by Broeren et al. (Ref. 68); some examples are presented in Section 3.1.2.

For icing tests, the pressure-instrumented leading edge was removed and replaced with a completely smooth leading edge. For each icing test run, the desired temperature and speed condition were established with the appropriate time allotted for the model and tunnel to reach thermal equilibrium. The spray cloud was turned on for the desired period of time and then the tunnel was shut down to allow for documentation of the ice accretion. Photographs were taken first, followed by 3D digital measurement using a laser-based scanning system (described in Sec. 2.2). In some cases, a section of the ice was removed from the model and weighed after the 3D measurements were completed.

The ice-accretion results shown by Broeren et al. (Ref. 68) consist of 2D section cuts and photographs to document the general 3D morphology. Many of the ice accretions observed during the IRT test campaigns were highly 3D, such that any type of 2D description is limited. Given that icing simulation tools typically provide 2D ice-shape cross sections, results of this type are required for comparison. The approach that was used for this research effort was to take 30 section cuts through the 3D scan of the ice accretion perpendicular to the wing leading edge, as shown in Figure 14. These 30 section cuts were taken at a spacing of 0.2 in., thus covering 6 in. of ice accretion along the leading edge near the model centerline, 36 in. above the floor. The section cuts were projected onto a single plane and the maximum outer boundary was obtained. The resulting maximum combined cross section (MCCS) represents the outermost extent of the ice over that 6-in. segment. The 6-in. segment was determined to be sufficient to capture all of the significant features of the ice accretions in these test campaigns. The MCCS is considered to be equivalent to the traditional hand-tracing method that typically results in the maximum outer boundary of an ice accretion. Traditionally, digitized hand tracings of ice accretion have been the basis for evaluation of icing simulation codes such as LEWICE3D.

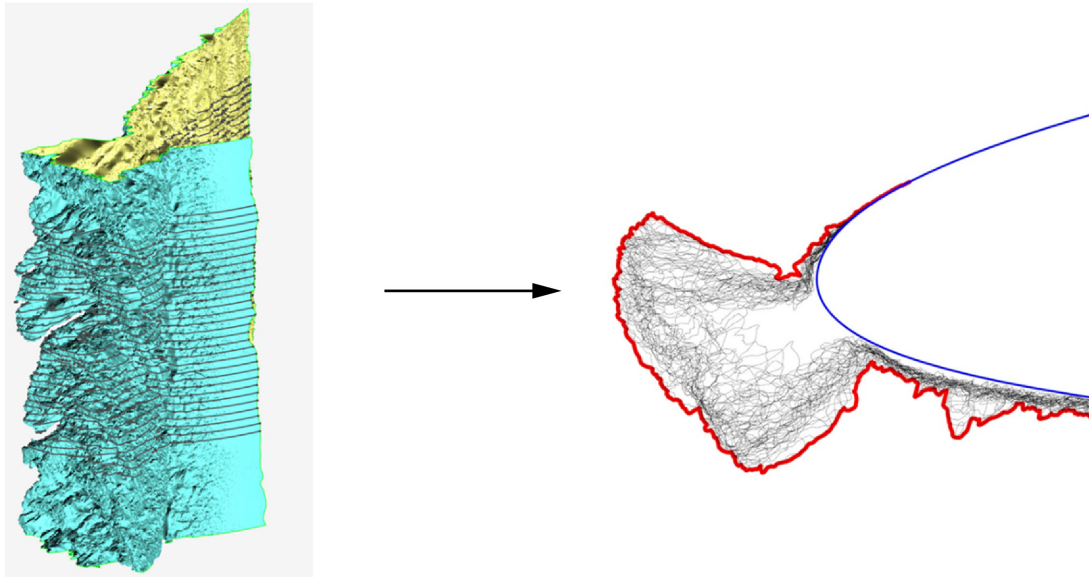


Figure 14.—Schematic description of process used to determine maximum combined cross section of 3D ice accretion.

The aerodynamic and icing test conditions were based upon the in-flight icing mission scenarios for the CRM65 airplane originally used in the hybrid model design process described in Section 2.3.2. A key advantage and motivation behind the hybrid model design approach utilized in this effort was maintaining the full-scale wing leading-edge geometry to generate flight-scale representative ice accretion. However, the resulting model sizes were still large relative to the IRT test section. These large model sizes, particularly for the Inboard model, limited the maximum speed that could be obtained. This limitation was primarily due to the solid and wake blockage effects of the model in addition to high aerodynamic loads. The Inboard model was tested in the first campaign, and it was found that the optimum speed for icing tests was 130 kn due to model dynamics and tunnel constraints. Both of these issues would have been exacerbated for larger models, such as an unscaled CRM inboard wing section. Because a key objective of this work was to simulate the ice accretion that would build up on the CRM65 airplane wing, identical icing conditions, including the speed of 130 kn, were used for all three models for consistency. To account for the reduction in speed to 130 kn, a scaling analysis was performed to match the freezing fraction at the attachment point and the local collection efficiency at the attachment point multiplied by the accumulation parameter. These are standard scaling methods that have been developed primarily for model-size-scaling applications (Ref. 71) and applied to swept wings (Refs. 72 and 73). A limited set of conditions at higher speeds was also run for the smaller Midspan and Outboard models. These results indicated that there are some effects on the final ice shape that cannot be

accounted for in scaling for speed (Ref. 68). However, this was considered an acceptable tradeoff in order to generate full-scale ice shapes in the IRT testing.

#### 2.3.4 Posttest Comparison of Experimental and Computational Ice Shapes

After the completion of the IRT test campaigns, a significant effort was dedicated to comparisons of the experimental ice shapes with those obtained from computational simulation. This work built directly upon the simulations described in Sections 2.3.1 and 2.3.2 and was performed using the model geometries as tested in the IRT along with the equivalent test conditions. Fujiwara et al. (Refs. 74 and 75) describe the icing simulations and comparisons performed for a set of six icing conditions on each of the three hybrid models (Inboard, Midspan, and Outboard). The 3D RANS solver OVERFLOW was used to compute the initial flow field, and the ice shapes were generated with LEWICE3D. Yadlin et al. (Ref. 76) performed a larger set of experimental versus computational ice-shape comparisons that also used OVERFLOW for the initial flow-field solutions. For these simulations, the version of LEWICE3D was slightly different and resulted in some improvements to the ice-shape comparisons as addressed in Section 3.1.2.

Radenac et al. (Refs. 77 and 78) also performed a series of ice-accretion simulations using the ONERA software called IGLOO3D. The so-called “predictor” approach was used: an initial flow-field solution was generated using ONERA’s 3D flow solver, elsA (ONERA/Airbus/Safran), described in Section 2.5. The droplet trajectories were then calculated with

ONERA’s CEDRE® platform using an Eulerian approach (SPIREE). Finally, the 3D Messinger solver MESSINGER3D of IGLOO3D was used to calculate the ice growth. For the cases assessed in this work, there was reasonable agreement between the IGLOO3D and LEWICE3D ice shapes, with most of the differences occurring for glaze ice. It is well known that numerical predictions of glaze ice are very sensitive to roughness and heat transfer models.

The comparison of the experimental ice-accretion results with the various computational simulation results was a major aspect of this research effort. Section 3.1.2 summarizes some of the key results and findings.

## 2.4 Phases IV, V, and VI: Aerodynamic Testing at Low to High Reynolds Number

Clean-wing and iced-wing aerodynamic testing was conducted at low to high Reynolds number in Phases IV, V, and VI. The high-Reynolds-number testing conducted in Phases IV and V was critical to determining both Reynolds and Mach number effects on the clean and iced wing performance. The low-Reynolds-number testing conducted in Phase V was performed to determine if a lower cost test capability is a viable option for iced swept-wing aerodynamic evaluation. The low-Reynolds-number tests were also needed to prepare models and test methods for the much more expensive and critical high-Reynolds-number tests. Finally, the low-Reynolds-number tests were much more suitable for flow visualization and wake survey measurements.

The aerodynamic testing associated with Phases IV, V, and VI was not conducted in the stepwise chronological order implied by Figure 2. In reality, there were four low-Reynolds-number test campaigns (plus an initial model check-out test) associated with Phase V. These were conducted before, in between, and after the two high-Reynolds-number test campaigns associated with Phases IV and VI. This approach was employed to exploit the lower cost and more easily accessible low-Reynolds-number facility to minimize the risks associated with the higher cost and critically important high-Reynolds-number tests. There was an inseparable connection among the tests conducted in Phases IV, V, and VI. As such, it makes sense to combine the description of these phases into this single report section.

### 2.4.1 Experimental Facilities and Test Conditions

The high-Reynolds-number aerodynamic testing was carried out at the ONERA F1 pressurized wind tunnel located at Le Fauga-Mauzac Center in southwestern France. The closed-return tunnel can be pressurized to 56 psi and has a test section

approximately 11.5 ft high by 14.8 ft wide. The maximum speed is  $M = 0.36$  at a pressure of approximately 22 psi, which corresponds to a Reynolds number per foot of approximately  $3.7 \times 10^6$ . The maximum Reynolds number is  $6.1 \times 10^6/\text{ft}$  at a pressure of approximately 56 psi and  $M = 0.23$ . The angle-of-attack sweeps were performed with a continuous change in pitch angle at a constant rate of 0.1 deg/s. The model angle of attack was varied from  $-6^\circ$  to  $25^\circ$  except in cases where dynamic forces limited the maximum angle of attack or a clear local maximum in lift coefficient was measured. Force balance and surface pressure measurements were acquired for several combinations of Reynolds and Mach numbers. Torz-Dupuis (Ref. 79) and Rossoni (Ref. 80) provide detailed reports of the test setup and instrumentation, data reduction, experimental uncertainties, and wall corrections.

The low-Reynolds-number aerodynamic testing was carried out in the Walter H. Beech Wind Tunnel at Wichita State University (WSU). The tunnel is an atmospheric, closed-return, subsonic wind tunnel with a 7- by 10-ft test section. The maximum speed of the tunnel is approximately 350 ft/s, which corresponds to a Reynolds number of approximately  $2.0 \times 10^6/\text{ft}$  and a maximum dynamic pressure of 125 psf. Force balance and surface pressure measurements were acquired at Reynolds number based on model mean aerodynamic chord of  $0.8 \times 10^6$ ,  $1.6 \times 10^6$ , and  $2.4 \times 10^6$ , which corresponded to freestream Mach number of 0.09, 0.18, and 0.27. The model angle of attack was varied from  $-6^\circ$  to  $25^\circ$ . The specific angle-of-attack schedule was adjusted depending upon the model configuration. Woodard et al. (Ref. 81) describe the details of the experimental setup at the WSU facility for these tests. Table IV contains the matrix of test conditions for both the F1 and WSU facilities.

TABLE IV.—MATRIX OF REYNOLDS AND MACH NUMBER CONDITIONS

Reynolds number <sup>a</sup>	Mach number				
	0.09	0.18	0.23	0.27	0.34
$0.8 \times 10^6$	WSU <sup>b</sup>				
$1.6 \times 10^6$	F1 <sup>c</sup>	WSU			
$2.4 \times 10^6$				WSU	
$2.7 \times 10^6$	F1	F1			
$4.0 \times 10^6$	F1	F1	F1	F1	
$6.8 \times 10^6$		F1	F1	F1	F1
$9.6 \times 10^6$		F1			
$11.9 \times 10^6$			F1		

<sup>a</sup>Based upon the model mean aerodynamic chord.

<sup>b</sup>Wichita State University model.

<sup>c</sup>ONERA F1 model.

Load measurements were performed using a six-component force balance located beneath the test-section floor at both facilities. This study utilized a reflection plane model, and the force balance was used to measure the lift, drag, and pitching moment. Further details regarding the uncertainties in lift, drag, and pitching moment can be found in Broeren et al. (Ref. 82) and Woodard et al. (Ref. 81) for the F1 and WSU facilities, respectively. These references also describe the data corrections applied to the aerodynamic performance data ( $\alpha$ ,  $C_L$ ,  $C_M$ ,  $C_D$ , and  $C_p$ ), and the data acquisition process, which was slightly different between the two facilities. The magnitude of the correction to the angle of attack applied to the WSU wind tunnel data has been reduced relative to initial papers and reports related to this project (Refs. 81 and 83 to 85). Lee et al. (Refs. 86 and 87) have conducted an extensive comparison of the aerodynamic data acquired at the WSU wind tunnel and the data acquired at the ONERA F1 facility. Overall, the results agree very well for both the clean and iced wing configurations. The largest differences were observed in drag

coefficient, where there appeared to be a small offset between the facilities.

## 2.4.2 Wind Tunnel Models

The two semispan models fabricated for these wind tunnel tests were based on 8.9- and 13.3-percent-scale versions of the CRM65 wing. The 8.9-percent-scale model is referred to as the “WSU model” and the 13.3-percent-scale model is referred to as the “F1 model,” reflecting the facilities for which they were designed. Table V summarizes the geometric parameters of the wings. The F1 model is exactly 50 percent larger than the WSU model. The full-scale, original CRM geometry has a realistic cruise configuration loading applied to the wing, resulting in a wing shear similar to dihedral (Ref. 37). To simplify the design of the removable leading-edge segments (described below), this shearing or “bending” of the wing was removed from the model geometry, resulting in an unsheared wing with a straight leading edge across the span of the model. The wing retains the twist and taper of the original CRM. A planform view of the F1 model is shown in Figure 15 with key dimensions.

TABLE V.—SUMMARY OF 8.9- AND 13.3-PERCENT-SCALE CRM65 SEMISPAN WING GEOMETRIC PARAMETERS

Wing parameter	F1 <sup>a</sup> value (13.3 percent)	WSU <sup>b</sup> value (8.9 percent)
Span, $b$	7.5 ft (90.00 in.)	5.0 ft (60.00 in.)
Mean aerodynamic chord (MAC)	2.08 ft (25.01 in.)	1.39 ft (16.67 in.)
Area (geometric)	13.55 ft <sup>2</sup> (1,951.0 in <sup>2</sup> )	6.01 ft <sup>2</sup> (865.3 in <sup>2</sup> )
Volume	2.090 ft <sup>3</sup> (3,604.5 in <sup>3</sup> )	0.617 ft <sup>3</sup> (1,069.0 in <sup>3</sup> )
Aspect ratio <sup>c</sup>	8.3	8.3
Taper ratio	0.23	0.23
Root chord	3.38 ft (40.50 in.)	2.25 ft (27.00 in.)
Tip chord	0.77 ft (9.28 in.)	0.52 ft (6.19 in.)
Root, $\alpha$	4.4°	4.4°
Tip, $\alpha$	-3.8°	-3.8°
1/4-chord sweep angle	35°	35°
Leading edge sweep angle	37.2°	37.2°
Location of rotation center <sup>d</sup>	$x = 29.05$ in., $z = 0$	$x = 19.37$ in., $z = 0$
Location of moment center <sup>d</sup>	$x = 35.80$ in., $z = 0$	$x = 23.87$ in., $z = 0$
Location of $0.25 \times \text{MAC}$ <sup>d</sup>	$x = 26.23$ in., $z = 0$	$x = 17.49$ in., $z = 0$

<sup>a</sup>ONERA F1 model.

<sup>b</sup>Wichita State University model.

<sup>c</sup>Whereas the other parameters in this table are defined specifically for this model, the aspect ratio is defined for a complete airplane configuration using the formula  $(2 \times \text{semispan})^2 / (2 \times \text{area of one wing})$ .

<sup>d</sup>(0, 0, 0) is the wing root-section leading edge at zero angle of attack.

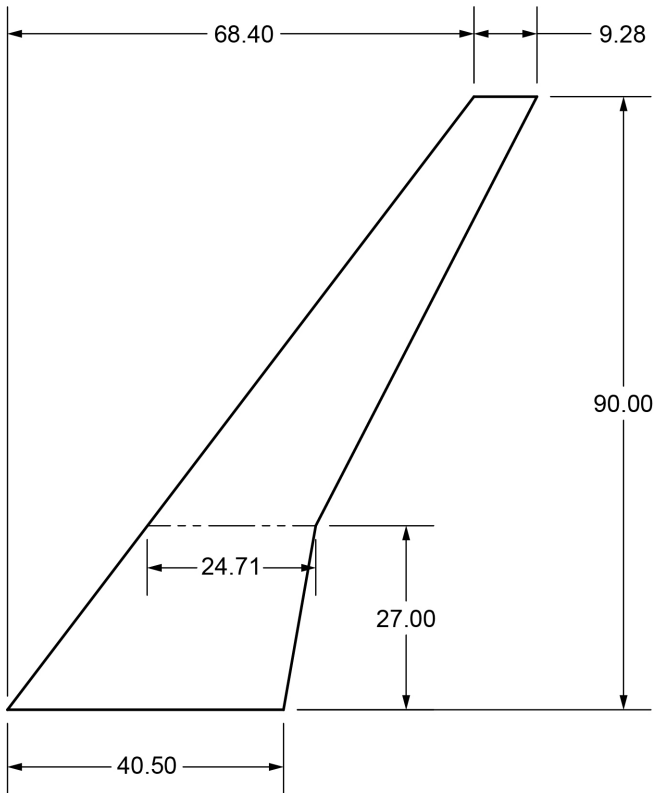


Figure 15.—13.3-percent-scale (F1 model) CRM65 semispan wing planform with key dimensions labeled in inches.

Figure 16 shows photographs of the wing models installed in their respective wind tunnels with circular splitter plates. An artificial ice shape is mounted to the leading edge of the F1 model, and the WSU model is shown in the clean configuration. Below the circular splitter plate shown in the images, a streamlined shroud isolates the wing spar from any aerodynamic loads. With this arrangement, both the splitter plate and shroud were nonmetric, meaning the aerodynamic forces were only measured on the wing itself. The designs of the splitter plate and shroud were specifically investigated during a preliminary test campaign utilizing the WSU model prior to the design and fabrication of the F1 model (Refs. 81 and 83). Prior to this, a series of smaller scale investigations on various splitter plate designs were performed at the University of Illinois (Ref. 88).

The models were designed and built with removable leading edges that allowed artificial ice shapes to be added to the wing. The main components of each model were the main element (including a spar that attached to the force balance), a full-span clean leading edge, and a partial-span leading edge used for mounting ice shapes. An open channel exists inside the model between the main element and any of the leading-edge components for routing pressure tubing out through the base of the model to the data acquisition system. The partial-span

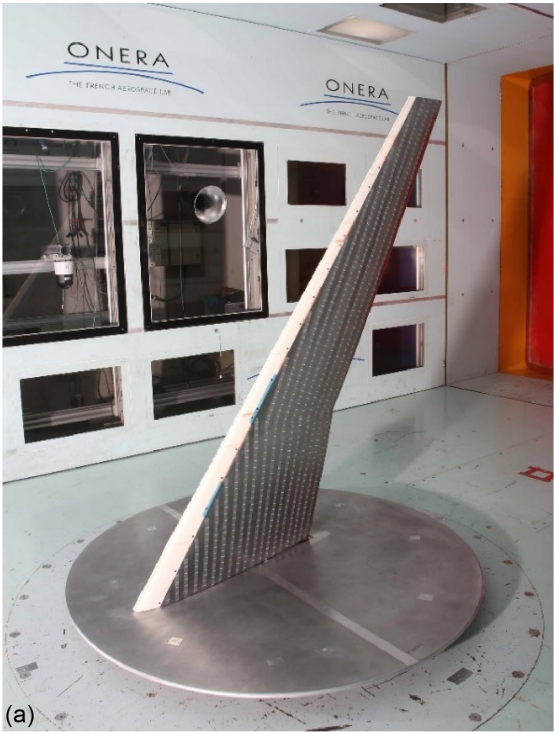


Figure 16.—Subscale CRM65 semispan wing models installed in their respective wind tunnels. (a) 13.3-percent-scale CRM65 semispan wing installed in ONERA F1 test section. (b) 8.9-percent-scale CRM65 semispan wing installed in WSU test section.

removable leading edge extended from the root to 83 percent of the semispan for the F1 model and from the root to 50 percent of the semispan for the WSU model. Both contained a portion of the airfoil contour on the lower surface. Artificial ice shapes were attached to these removable leading edges and covered the entire upper surface. Outboard of this partial-span leading edge, the artificial ice shapes were attached directly to the main element. The model is too thin at the outboard portion of the wing to support the addition of a full-span removable leading edge. This design does not adversely affect the efficiency or repeatability of the artificial ice-shape configuration changes.

The artificial ice shapes were created using a rapid prototype manufacturing (RPM) technique called stereolithography (SLA). The SLA process utilizes an ultraviolet (UV) laser to solidify liquid polymer resins. The majority of the artificial ice shapes were manufactured from the Somos<sup>®</sup> (Royal DSM N.V.) NeXt polymer. Some of the early ice shapes were 3D printed using Accura 60. The tolerances are advertised to be approximately  $\pm 0.005$  in. for this process for either polymer. The Somos<sup>®</sup> NeXt material was selected due to desirable advertised properties associated with the stability of the printed parts. The stability of the materials was important because the project required artificial ice shapes to be in storage for over 1 year between tests. Early work with SLA products proved challenging with regard to long-term storage. Mitigating exposure to water vapor in the air and UV radiation has been shown to drastically improve the lifetime of the parts for repeat testing. The process for creating an artificial ice shape involves adding the full-span ice shape to the necessary wing geometry and then dividing the ice shape into sections. The leading edge was divided into three segments for the F1 model and two segments for the WSU model. All segments were approximately 37.5 in. long. Pressure taps were installed in each of these segments at the same locations as on the clean removable leading edge. The pressure tap holes were included in the RPM design, and then stainless steel tubes were glued into each hole and plumbed to a quick disconnect inside the channel between the removable leading edge and the main element.

The pressure taps in the models were primarily distributed in streamwise rows across the span of the model. The F1 model contained 243 pressure taps in its clean configuration, and the WSU model contained 219. The taps in the main element of the model were plumbed with stainless steel tubing from their location on the surface and extending out the root of the model. The routing of the taps in the removable leading edges required a more complicated design. The stainless steel tubing in both the clean leading edge and in the RPM ice leading edges transitioned to plastic tubing and then connected to a Scanivalve (Scanivalve Corporation) quick-disconnect fitting. The use of these fittings allowed relatively quick model reconfigurations between clean and various RPM leading edges.

### 2.4.3 Swept-Wing Performance Parameters

A large number of cases for comparison were developed over the course of this project. Performance parameters were extracted from the data to compare the impacts of ice-shape configurations and fidelity variations as well as Reynolds and Mach number effects. Figure 17(a) shows lift and pitching moment coefficient data plotted against angle of attack, and Figure 17(b) shows lift coefficient plotted against drag coefficient. Most of the aerodynamic performance data presented in the numerous publications associated with this project are plotted in this way. Figure 17 includes only one data set in order to clarify the performance parameters, but generally, several data sets are plotted together. The traditional aerodynamic performance parameters of maximum lift coefficient,  $C_{L,max}$ , stall angle,  $\alpha_{stall}$  (defined as the angle of attack at  $C_{L,max}$ ), and minimum drag coefficient,  $C_{D,min}$ , were used throughout this program. However, those parameters are not sufficient to describe the deleterious impact of ice accretions on swept wings. For example,  $\alpha_{stall}$  increases when ice shapes are installed on the wing for most configurations. As such, additional performance parameters have been adapted for application to these swept-wing icing tests. Broeren et al. (Ref. 83) provide a detailed description of the performance parameters and their application to this study. The three additional performance parameters are summarized here. To more completely capture the stall progression on the swept wing, the performance parameter “usable” or “inflection” lift is defined based on past work by Furlong and McHugh (Ref. 89). This lift coefficient is defined to be coincident with the first local minimum in the pitching moment coefficient calculated about the quarter-chord of the mean aerodynamic chord. As the flow separation increases inboard from the wing tip, the pitching moment about the quarter-chord of the mean aerodynamic chord eventually begins to increase, indicating a substantial flow separation. As shown in Figure 17, the first local minimum in the pitching moment coefficient nearly corresponds to the angle of attack where the lift coefficient diverges from the linear range. These lift parameters are specifically denoted as  $C_{L,use}$  and  $\alpha_{use}$ . Additional parameters can also be extracted from the drag data. The minimum drag value is a convenient parameter for comparing the ice-shape fidelity variations; it occurs near zero lift, so the influence of induced drag is minimized. However, an aircraft does not operate at zero lift, so another point of comparison at higher lift coefficient is desirable. Lynch and Khodadoust (Ref. 90) suggest a process for determining this drag coefficient, and Broeren et al. (Ref. 83) explain the implementation for this particular swept wing. A lift coefficient equal to 0.6 was identified as the reference value for determining the drag coefficient, and this associated drag value is denoted as  $C_{D,0.6}$  to indicate that it is the drag coefficient when  $C_L = 0.6$ .

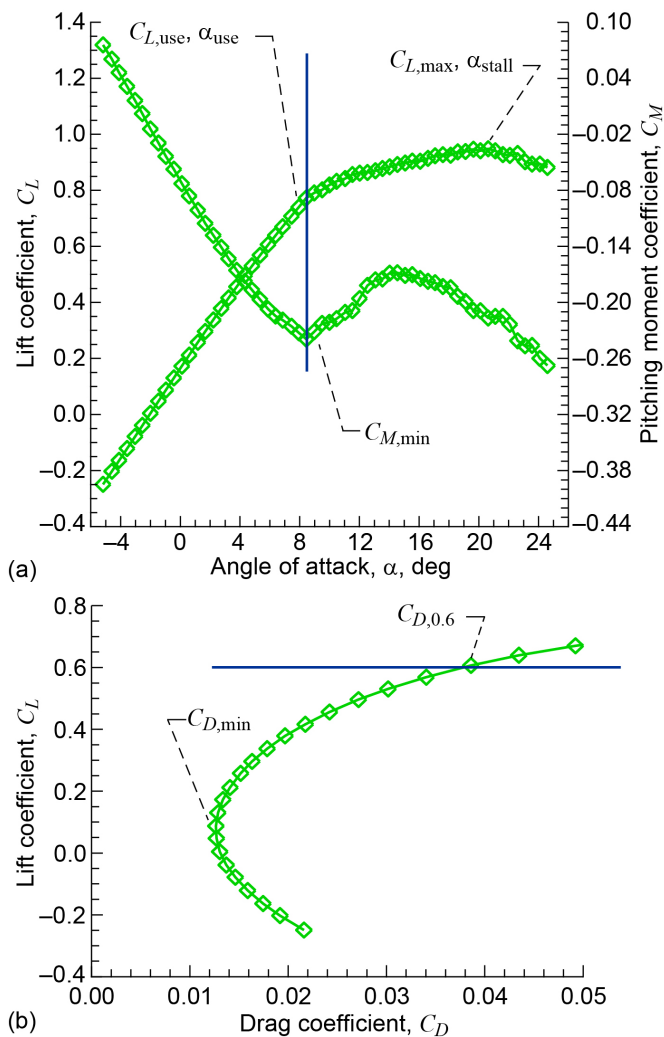


Figure 17.—Example aerodynamic performance data illustrating performance parameters utilized in configuration comparisons throughout project. (a) Lift coefficient versus angle of attack. (b) Lift coefficient versus drag coefficient.

#### 2.4.4 Flow Visualization

Two flow visualization methods were utilized during the aerodynamic testing. Surface oil flow visualization was conducted for selected 8.9-percent-scale model configurations at WSU, and mini-tuft flow visualization was conducted for both the 8.9-percent-scale model configurations at WSU and the 13.3-percent-scale model configurations at ONERA F1.

Fluorescent mini-tuft flow visualization was employed during most of the angle-of-attack sweeps performed during the F1 test campaigns. The mini-tuft material was 0.006-in.-diameter fluorescent monofilament fishing line. The tufts were approximately 1.2 in. long and were applied to the model upper surface using 0.002-in.-thick tape. Continuous UV blacklight was used to illuminate the mini-tufts during the angle-of-attack sweeps. The tuft motion was recorded using three high-definition video cameras oriented at different viewing angles.

The videos were annotated in real time with the model angle of attack. Comparison of force balance data with and without the tufts located downstream of the upper-surface boundary-layer trip showed little to no effect of the tufts on the lift, drag, and pitching moment (Ref. 82). The upper-surface trip consisted of CAD Cut (Web Industries, Inc.) trip dots, height 0.0031 in., located between 2.5 and 3.0 percent of the local streamwise chord.

Fluorescent mini-tuft flow visualization was also employed during two of the WSU test campaigns for selected configurations. The mini-tuft material was 0.0019-in.-diameter fluorescent monofilament. The tufts were approximately 1 in. long and were applied to the model upper surface using cyanoacrylate adhesive. The tufts were positioned in streamwise rows with little streamwise spacing between each tuft. Each of these streamwise rows was approximately 2 in. from the next row in the spanwise direction. A UV blacklight flashlamp was used to illuminate the mini-tufts during the angle-of-attack sweeps. A digital camera triggered the flash lamp to collect one image at each angle of attack. Comparison of force balance data with and without the tufts showed little to no effect of the tufts on the lift, drag, and pitching moment.

In the low-Reynolds-number facility at WSU, surface oil flow visualization was employed for select configurations at select angles of attack. The local airflow shear forces move the oil along the surface, illustrating patterns on the model. These patterns can be interpreted to identify the location of separated flow, flow reattachment, and vortices. The flow visualization experiments were performed separately from the aerodynamic performance sweeps. Because the performance data had already been collected, these specific configurations and angles of attack could be efficiently identified before running the flow visualization tests. In preparation for these tests, the upper surface of the model was covered with black contact paper (flow visualization was only performed on the upper surface). Fluorescent dye and mineral oil were mixed and then painted onto the model using sponge paint rollers. The model was set to the desired angle of attack before starting the fan. For most of these cases, the wind tunnel fan ran for 2 min. When the airflow stopped, the model angle of attack was rotated to a standard location so it would appear in the same portion of the image frame for all angles of attack. UV blacklights were placed inside the test section to illuminate the oil, and the still images were acquired. After taking the image for a particular angle of attack, the oil was redistributed with the same paint rollers to once again uniformly cover the upper surface. The model was set to the next angle of attack and the process was repeated. The data acquisition for each angle of attack for a given configuration was relatively efficient. However, the entire process (starting with covering the model with contact paper) had to be repeated for each different ice-shape configuration.

#### 2.4.5 Wake Survey Measurements

In addition to the aerodynamic performance data and flow visualization collected for the clean and iced wing, additional measurements were made in the wake downstream of the wing for a subset of cases. These wake survey data were acquired at  $Re = 1.6 \times 10^6$  and  $M = 0.18$  conditions in the WSU facility only. Measurements were made using five-hole pressure probes that allow determination of the flow velocity in all three dimensions. From this information, the spanwise distribution of lift and drag was calculated along with wake vorticity. More complete details regarding these measurements can be found in Lum et al. (Ref. 85). The process of acquiring a full wake survey for one configuration was extremely time consuming, so this was performed for a limited number of cases.

#### 2.4.6 Artificial Ice Shapes

Numerous sets of artificial ice shapes were developed based on the IRT test results. The ice shapes with the highest geometric fidelity were generated directly from the 3D scans of the experimental ice accretion. The method used to generate a full-span, high-fidelity ice shape involved interpolating or morphing between the scanned sections of the Inboard, Midspan, and Outboard CRM65 ice shapes using the weighted averaging function in Geomagic Studio (3D Systems, Inc.) Ref. 91) as described by Camello et al. (Refs. 92 and 93). An extrapolation method was also developed to generate artificial ice shapes at the root and tip of the wing using the artificial ice shapes at the Outboard and Inboard model stations and results from the LEWICE3D ice-prediction code. The full-span ice shapes that were developed from the 3D scans contained all of the highly 3D properties of the original ice shape, including ice scallops, feathers, and roughness. Due to the nature of the ice-shape generation process, a repeated pattern was introduced across the span of the wing. Such ice shapes are designated as “3D high fidelity,” meaning they are the most detailed ice shapes available based on current understanding and technology. Lee et al. (Ref. 94) summarize the process by which laser scans of ice shapes were transformed into wind tunnel model ice shapes and discuss the limitations of current methods for ice-shape reproduction.

Various lower fidelity representations were also created based on the full-span high-fidelity shapes. The ice shapes described as “3D smooth” were built by taking section cuts

along the span, smoothing those cuts, and then lofting them to build a new, full-span ice shape. These 3D smooth ice shapes are spanwise smooth in the sense that no scallops or discontinuities are represented, but they are 3D such that the ice thickness and location vary across the span. Some past publications have described these lower fidelity ice shapes as “2D smooth” (Refs. 22, 84, 85, 93, and 95), but that naming convention might imply, incorrectly, that the cross section of the ice shape does not vary across the span. The ice shapes detailed in this work and described as 3D smooth have substantial spanwise variation because they are derived directly from the high-fidelity ice shapes; they simply do not have the discontinuities present in the high-fidelity ice shapes. An additional category of lower fidelity ice shapes, “3D simple” ice shapes, has been developed to investigate the aerodynamic impact of specific ice-shape features and locations. These ice shapes could be based on backward-facing steps or other simple shapes. The cross-sectional geometry is a constant across the span, but the step height and location could change with span. Broeren et al. (Refs. 96 and 97) provide details on the design of specific 3D simple ice shapes that have been tested over the course of this project.

The 3D smooth ice shapes drastically reduce the complexity of the original ice shape by creating a shape without any of the local features present in the highly 3D representation. To investigate the aerodynamic sensitivity to the spanwise features, artificial ice shapes of another type, with a different fidelity, were developed. Some past publications have referred to these ice shapes as “artificial scallops” (Refs. 87 and 98), as they somewhat recreate the scallops or lobster tails evident in the actual ice accretion, but scallops are only one example of the highly 3D features present in a swept-wing ice shape. This work uses the more general category of “3D discontinuous,” indicating that highly 3D features such as discontinuities have been added to otherwise continuous ice shapes. The concept for these ice shapes is straightforward in that material is simply removed from the 3D smooth ice shape, resulting in a spanwise pattern. Details regarding the design of these ice shapes can be found in Woodard and Bragg (Ref. 99). Examples of each of these fidelities of ice shape are shown in Figure 18; each example shows only a small segment of the span that is representative of the entire ice shape. Table VI lists the five ice-shape fidelity configurations and summarizes their key characteristics.

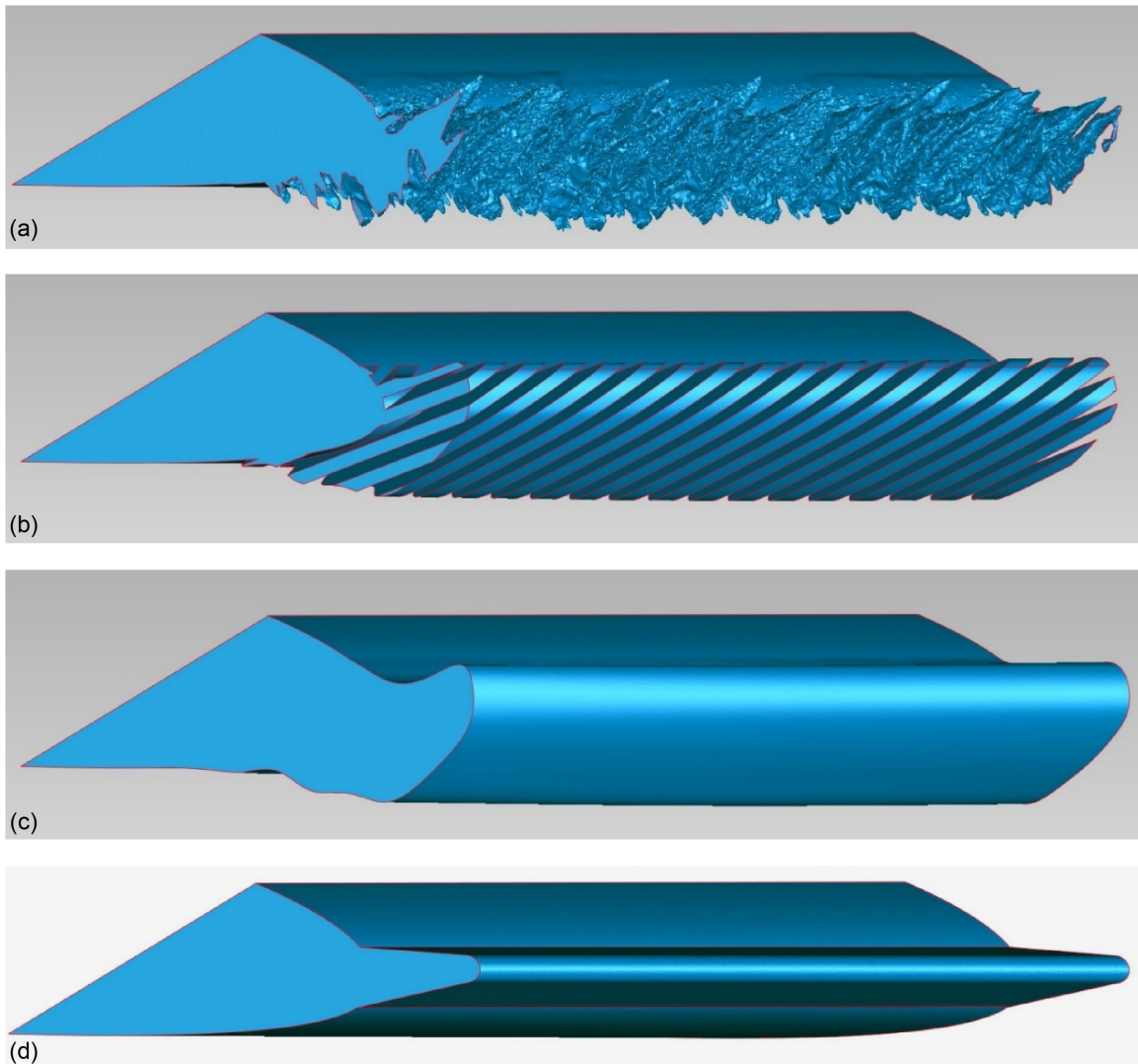


Figure 18.—Renderings of artificial ice shapes illustrating fidelity variations. (a) High fidelity. (b) 3D discontinuous. (c) 3D smooth. (d) 3D simple.

TABLE VI.—ICE-SHAPE FIDELITY NOMENCLATURE

Name	Description	Examples
3D high fidelity	Ice shapes created using an interpolation methodology, capturing all details possible	
3D discontinuous <sup>a</sup>	Ice shapes created by removing material from 3D smooth ice shapes to create spanwise discontinuities	
3D smooth <sup>b</sup>	2D sections varying with span; spanwise smooth; sections based on icing codes or experimentally determined	MCCS <sup>c</sup> , LEWICE3D
3D simple	2D sections varying with span; spanwise smooth; sections not entirely defined experimentally or computationally	Rectangle, triangle, spoiler
2D	Constant 2D section	

<sup>a</sup>In certain past publications, 3D discontinuous ice shapes were referred to as “artificial scallop” (Refs. 87 and 98).

<sup>b</sup>In certain past publications, 3D smooth ice shapes were referred to as “2D smooth” (Refs. 22, 84, 85, 93, and 95).

<sup>c</sup>Maximum combined cross section.

Additional ice-shape geometry variations were developed and tested within these categories. The 3D smooth geometry was based upon the high-fidelity geometry morphed from the 3D scans of the IRT ice accretion. Additional variations of 3D smooth geometry were also developed based upon LEWICE3D simulation results. Broeren et al. (Refs. 96 and 97) and Woodard et al. (Ref. 98) summarize the design of the LEWICE3D-based ice shapes. In naming the LEWICE3D-based ice shapes, IFB was used to indicate that the simulations were performed for the CRM65 airplane iced-flight baseline, and IRT indicates that the simulations were performed for the hybrid model geometry as installed in the IRT. Many of the lower fidelity ice shapes were tested in both the smooth condition and with roughness applied to the surface. Surface roughness was typically composed of silicon carbide grains adhered to the surface with epoxy. The grit was added with complete coverage for all of the configurations. The most common grit size for the WSU and F1 models was 60 and 46 grit, respectively, based on the FAA recommended roughness size of 3 mm for a full-scale aircraft (Ref. 100). In one case, hemispherical roughness elements having a full-scale height of 3 mm were incorporated into a 3D smooth solid model and fabricated as a part of the rapid-prototyping process. More details on the grit sizing and trade studies can be found in Woodard et al. (Refs. 98 and 101).

#### 2.4.7 Configurations Tested

Six test campaigns were performed, four at the WSU wind tunnel and two at the ONERA F1 wind tunnel. The WSU campaigns were performed during the following time periods:

- Campaign 1: February to March 2016
- Campaign 2: May to June 2016
- Campaign 3: May to June 2018
- Campaign 4: February to March 2019

The ONERA F1 test campaigns were performed during these time periods:

- Campaign 1: May 2017
- Campaign 2: November 2018

Table VII gives the specific configurations tested during each campaign at each wind tunnel. The name given to each ice shape is listed along with the fidelity representation. (Ice-shape names are discussed further in Sec. 3.1.2.) The table indicates which measurements were performed during each campaign, as many of the configurations were tested during multiple campaigns. Force balance and surface pressure data were always acquired together. Surface oil flow visualization and wake surveys were performed only in the WSU facility. Details regarding the specific geometric characteristics of the ice-shape configurations are provided in the references cited in Section 2.4.6.

## 2.5 Phase VII: 3D Ice-Accretion and Computational Flow-Field Simulation

The computational simulation research in Phase VII was performed in parallel with the activities described in Sections 2.2 to 2.4. A large number of flow-field and ice-accretion simulations were carried out in Phase III, as described in Section 2.3. Those simulations were critical to the development and testing of the hybrid icing models and the posttest analysis of the resulting ice-accretion geometries. Fujiwara and Bragg (Ref. 95) extended these simulations to develop an integrated 3D computational icing analysis approach applicable to airplane conceptual design. Additional activities focused on computational aerodynamic simulation of the clean and iced swept wing to support and compare with the aerodynamic testing performed in Phases IV, V, and VI. For example, some CFD computations were carried out for the clean-wing configuration at the WSU flow conditions and used for comparison with the experimental data (Ref. 83). These simulations were performed with a transition model instead of making a fully turbulent flow assumption or predefining a transition location. The transition model takes into account Tollmien–Schlichting and crossflow instabilities and is described in Reference 102. Figure 19 compares the transition location obtained from the CFD simulations with the surface oil flow visualization results obtained at WSU.

TABLE VII.—SUMMARY OF CONFIGURATIONS TESTED AT BOTH FACILITIES INCLUDING MEASUREMENTS COMPLETED DURING EACH TEST CAMPAIGN

Ice-shape configuration	Low-Re testing (WSU <sup>a</sup> )											High-Re testing (F1 <sup>b</sup> )					
	Force balance and surface pressures				Mini-tufts			Oil flow visualization			Wake surveys		Force balance and surface pressures		Mini-tufts		
	Campaign				Campaign			Campaign			Campaign		Campaign		Campaign		
Clean	1	2	3	4	1				2			2	3	1	2	1	
Venetian blind, high fidelity	1				1												
Venetian blind, 3D smooth	1				1												
Venetian blind, 3D smooth + grit	1				1												
Max. scallop, high fidelity	1	2	3	4	1				2		4	2	3	1	2	1	2
Max. scallop, 3D smooth	1		3		1		3		1		4	2		1		1	
Max. scallop, 3D smooth + grit	1	2	3		1		3		1			2		1		1	
Max. scallop, 3D smooth + smaller grit			3				3								2		2
Max. scallop, 3D smooth + larger grit			3				3								2		2
Max. scallop, 3D smooth + hemisphere grit			3				3								2		2
Max. scallop, LEWICE3D IFB <sup>c</sup>			3				3							1			
Max. scallop, LEWICE3D IFB + grit			3				3								2		2
Max. scallop, LEWICE3D IRT <sup>d</sup>			3				3										
Max. scallop, LEWICE3D IRT + grit			3				3								2		2
Max. scallop, 3D discontinuous, small gap			3				3			3			3		2		2
Max. scallop, 3D discontinuous, medium gap			3				3			3			3		2		2
Max. scallop, 3D discontinuous, large gap			3				3										
Max. scallop, 3D discontinuous, normal to leading edge				4											2		2
Max. scallop, 3D discontinuous, streamwise				4						4					2		2
Max. scallop, 3D discontinuous, curved				4						4					2		2
Small gap scallop, high fidelity	1				1									1		1	
Small gap scallop, 3D smooth	1				1												
Small gap scallop, 3D smooth + grit	1				1												
Incomplete scallop, high fidelity		2		4					2					1	2	1	2
Low AoA <sup>e</sup> scallop, high fidelity	1	2			1												
Low AoA scallop, 3D smooth	1				1												
Low AoA scallop, 3D smooth + grit	1				1												
Streamwise/rime, high fidelity	1	2			1				1			2		1		1	
Streamwise/rime, 3D smooth	1				1									1		1	
Streamwise/rime, 3D smooth + grit	1	2	3		1		3		2			2		1		1	
WB33, high fidelity		2	3				3			3				1		1	
WB33, 3D smooth			3				3							1		1	
WB33, 3D smooth + grit			3				3			3				1		1	
WB33, LEWICE3D IFB			3				3										
WB33, LEWICE3D IFB + grit			3				3								2		2
3D simple horn ice, baseline height, baseline angle (q = 10°)			3				3								2		2
3D simple horn ice, baseline height, baseline angle (q = 10°) + grit			3				3			3			3		2		2
3D simple horn ice, half height, baseline angle (q = 10°)			3				3										
3D simple horn ice, half height, baseline angle (q = 10°) + grit				4													
3D simple horn ice, baseline height, q = 25° angle			3				3										
3D simple horn ice, baseline height, q = 25° angle + grit			3				3			3							
3D simple horn ice, half height, q = 25° angle			3				3										
3D simple horn ice, half height, q = 25° angle + grit			3				3										
3D simple horn ice, baseline height, q = 40° angle				4							4						
3D simple horn ice, baseline height, q = 25° angle + grit				4											2		2
3D simple horn ice, half height, q = 25° angle + grit															2		2

<sup>a</sup>Wichita State University.

<sup>b</sup>ONERA F1 facility.

<sup>c</sup>Iced flight baseline.

<sup>d</sup>Icing Research Tunnel.

<sup>e</sup>Angle of attack.

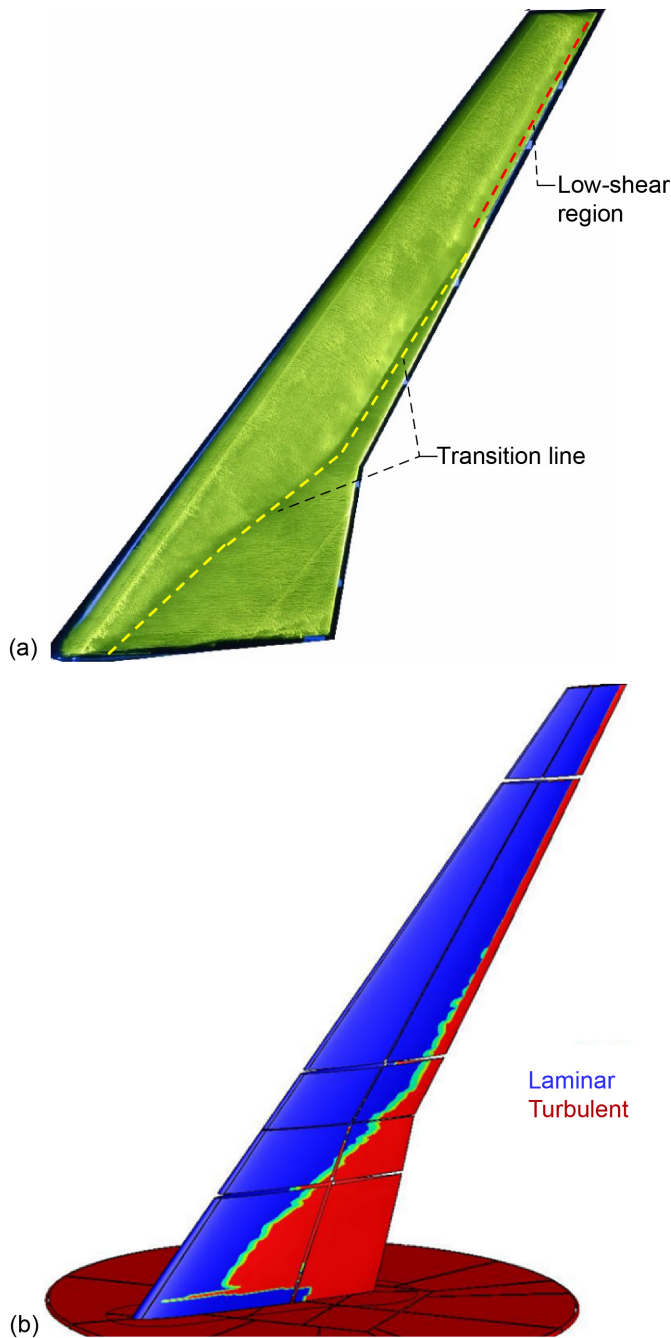


Figure 19.—Comparison of surface oil flow visualization and CFD result at  $\alpha_{\text{geo}} = 0^\circ$ ,  $\text{Re} = 1.6 \times 10^6$ ,  $M = 0.18$ . (a) Surface oil flow visualization. (b) CFD result (free transition).

The development of the 3D-ice-shape scanning capability paved the way for potential CFD simulations based upon the highly 3D ice-accretion geometries. An initial attempt was published in 2014 for an ice shape on a NACA 23012 straight-wing model (Ref. 103). Stebbins et al. (Refs. 104 and 105) later performed simulations with a 3D smooth ice shape on the 8.9-percent-scale wing as tested in the 7- by 10-ft wind tunnel

at WSU. As part of this research, a literature review of CFD studies of iced lifting surfaces was performed to summarize the current state of the art (Refs. 106 and 107).

In a parallel effort, ONERA investigated the use of the immersed boundary conditions (IBC) method to take the exact ice shape into account without having to mesh it explicitly (Refs. 108 to 111). A source term method was introduced to accurately account for the ice-shape boundaries. This IBC technique was developed in the ONERA elsA code (Ref. 112), and the validation phase for an application to iced-wing shapes was carried out in the current project, according to the following sequence:

1. Use of a 2D configuration for preliminary evaluation
2. Development and/or improvement of tools for ice-shape problems
3. 3D application for the 3D smooth maximum scallop ice-shape configuration tested in F1
4. Comparison with “standard” RANS computations in 3D flow

These results are reported in Section 3.4.

### 3.0 Key Results and Findings

Detailed results from this research effort have already been published in numerous reports and papers cited in Section 2.0. This section describes the key findings that answer the original three research objectives stated in Section 1.3:

1. *Generate a database of 3D swept-wing ice-accretion geometries for icing-code development and validation and for aerodynamic testing.* Section 3.1 reports key results associated with the ice-accretion testing and the development of a database of 3D swept-wing ice-accretion geometries.
2. *Develop a systematic understanding of the aerodynamic effect of icing on swept wings, including Reynolds and Mach number effects, important flow-field physics, and fundamental differences from 2D geometries.* Section 3.2 provides a summary of this effort’s contributions to the systematic understanding of iced swept-wing aerodynamics.
3. *Determine the effect of ice-shape geometric fidelity on aerodynamic simulation of swept-wing icing effects.* The aerodynamic classification of swept-wing ice shapes is revisited in Section 3.3 and is used to help summarize the effect of ice-shape geometric fidelity on swept-wing performance. Section 3.4 reports results and findings related to the computational aerodynamic simulation of the iced swept wing.

### 3.1 Database of 3D Ice-Accretion Geometry

The work required to successfully complete this objective was described in Section 2.3. This section reports key findings from the extensive hybrid model design effort (Sec. 3.1.1), the posttest comparison of experimental ice shapes with those generated from NASA and ONERA ice-accretion codes (Secs. 3.1.2 and 3.1.3), and the development of artificial ice shapes used for subsequent aerodynamic testing (Sec. 3.1.4).

#### 3.1.1 Hybrid Model Design

Prior to this research effort, there was no publicly available and systematic research study of icing wind tunnel testing of large-scale swept-wing geometries. Traditional aerodynamic wind tunnel testing relies on scale-model geometries, with aerodynamic effects being accounted for by addressing Reynolds and Mach numbers. In ice-accretion testing, maintaining the full-scale geometry of the icing surface of interest is critical to generating representative, full-scale ice shapes. Icing conditions can, to some extent, be scaled to account for changes in geometric size and other factors; however, for this research effort, maintaining a full-scale leading-edge geometry was considered a high priority due to the lack of relevant data in the public domain.

The design of the hybrid IRT models, where the full-scale leading edge was matched to a specifically designed and tailored afterbody and flap, was carried out with a variety of 2D and 3D computational tools for aerodynamic and icing simulations. The high levels of maturity and confidence in these tools were critical to successfully defining the model geometries in a relatively short period of time. The result was a highly integrated computational and experimental research effort where the computational simulations were used to understand experimental limitations such as the effect of the wind tunnel walls on airflow, drop trajectories, and ice accretions. The computational simulations provided a high degree of confidence that the icing wind tunnel experiments would yield ice shapes representative of icing flight conditions.

The hybrid model design process emphasized the need for proper configuration controls of the geometry. Even simplified 3D cruise wing geometries—without an engine pylon, chines, fairings, and other features of real wings—require a well-defined system to track the geometry and mark section cuts. Minor changes to the geometry in critical areas like the leading edge can lead to discrepancies in the highlight and attachment point locations. This situation is described in more detail by Broeren et al. (Ref. 68), where attachment point locations were updated after the 2015 IRT test campaigns were completed. Therefore, deliberate geometric controls must be implemented

when defining hybrid model geometries from the full-scale reference wing.

While both 2D and 3D tools were used in the hybrid model design process, many additional 3D simulations were required to refine the model design in the presence of the wind tunnel walls. Figure 20 illustrates the 3D nature of the upper-surface flow field on each of the three models. This is particularly evident on the Inboard model, where a large decrease in surface pressure along the leading edge indicates the spanwise flow from the bottom section at the test-section floor to the top section at the test-section ceiling. Also evident for all three models is the strong 3D flow interaction with the test-section ceiling at the top of each model. This wall interference caused an increase in the local flow angle of attack near the ceiling. These results emphasize the need to perform efficient 3D flow simulations at the outset of the process. The 2D tools have limited value for large models where wind tunnel walls produce 3D flow effects that must be taken into account.

Matching the location of the attachment line on the swept wing between the full-scale flight baseline wing and the hybrid model in the icing wind tunnel was a key parameter for matching the resulting ice shapes. In this work, the location of the attachment line was defined as the location associated with the maximum pressure coefficient. Using the pressure coefficient was convenient because it was easily obtained from the CFD simulations and also relatively easy to measure experimentally.

For the hybrid models, the attachment line location was a strong function of spanwise station, varying from the floor to the ceiling of the test section. This was a direct result of the spanwise flow and wall interference described in connection with Figure 20. Therefore, the attachment line could technically only be matched to the full-scale flight baseline at the vertical centerline of the icing tunnel test section, 36 in. above the test-section floor. Fujiwara et al. (Refs. 62 and 63) considered numerous computational design approaches to minimize the spanwise variation in attachment line location on the hybrid models. These design approaches included a gap between the top of the model at the test-section ceiling; wing twist; segmented flaps deflected at different angles; and changes in model aspect ratio. Although some of these methods did improve the spanwise uniformity of the attachment line, numerous tradeoffs limited the practical value. For example, adding wing twist was very effective, but this would have seriously complicated the mechanical design of the test articles and also introduced an artificial change in the ice-shape geometry to contend with. In the end, it was decided that the change in the attachment line location over the region of interest (approx. 12 in. in model span) was not large enough to impose significant complications to the test article design and fabrication.

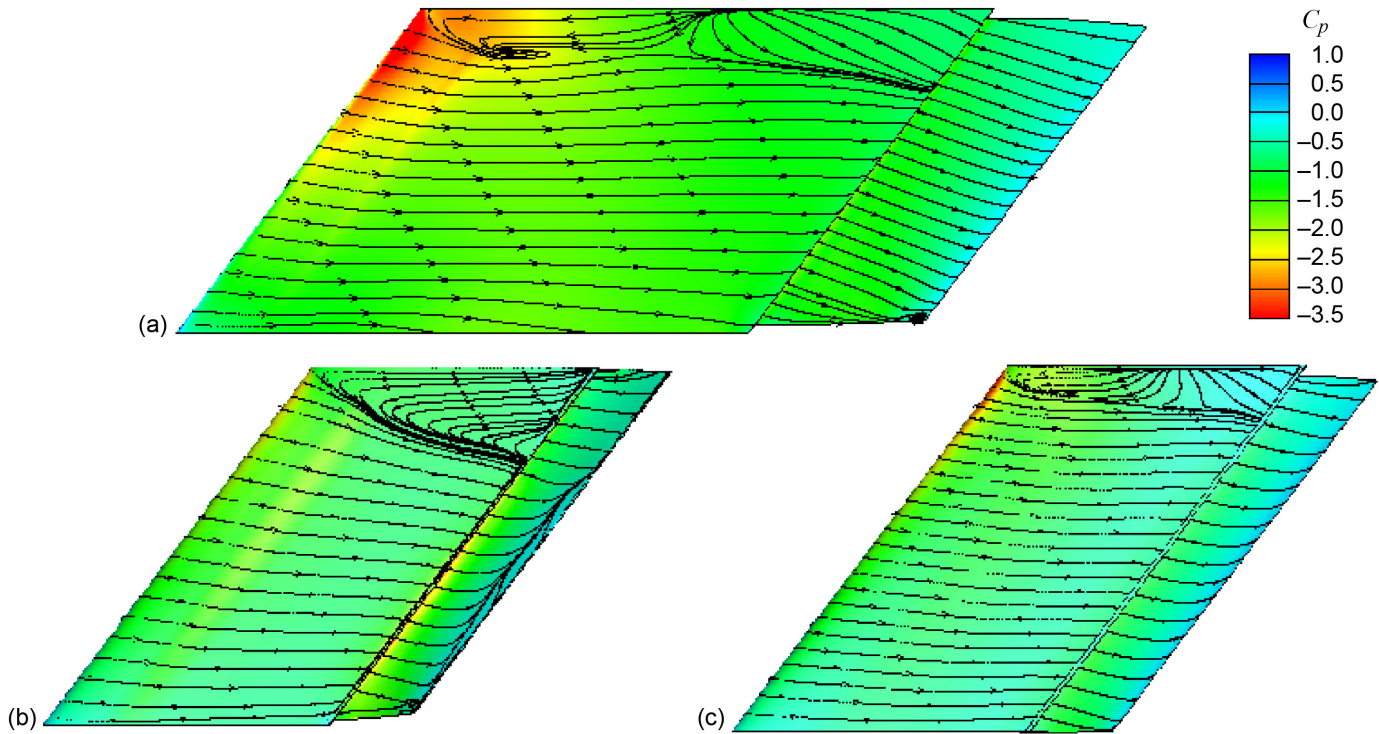


Figure 20.—Upper-surface-pressure coefficient contours and surface-flow streamlines from 3D RANS OVERFLOW simulations of hybrid models in presence of IRT test-section walls, after Reference 74. (a) Inboard. (b) Midspan. (c) Outboard.

Another consideration for hybrid model ice-accretion testing is the variation in overall model lift during the ice-accretion test. The hybrid model is designed to provide an attachment line that matches the full-scale airplane for a specific flight condition at the selected spanwise location. The hybrid shape and flap are designed to match the attachment line location of a potentially much larger wing chord and thus provide reduced tunnel blockage. The reduced chord and hybrid design often impose more severe adverse pressure gradients on the upper surface. Thus, especially as ice accretes, the model is susceptible to flow separation, which could cause a change in circulation and attachment line location. Therefore, while the model design considers the influence of the test section and tunnel walls, it should also consider the influence of the ice itself—or include a method to mitigate this effect. If the ice accretion has an impact on the attachment line (lift loss equates to the attachment line rotating upward) during the accretion test condition, the ice shape itself could accrete in a more conservative location as a function of time. While this phenomenon was recognized during this research, addressing it was deemed beyond the scope of the program.

### 3.1.2 Comparison of Experimental and Computational Ice-Shape Results

The ice-accretion results illustrate the extensive integration of computational and experimental tools. A subset of the

computational simulations described in Section 2.3 was conducted upon completion of the IRT testing. These posttest simulations were performed using the final model geometries as installed in the IRT test section along with the actual icing run conditions during the testing. As an example, Table VIII lists some of the icing conditions run on each of the three hybrid models. The first column lists the name given to the particular ice shape based upon its appearance; these names are discussed later in this section. Angle of attack and speed were identical for each case, representing a holding condition where the speed was scaled down to 130 kn from the flight reference speed of 232 kn. The flow simulations were performed at this condition using the OVERFLOW solver in RANS mode and 3D, as described in Section 2.3, where the test-section walls were included to account for model installation effects.

The flow solution was then used as input for subsequent LEWICE3D simulations for the icing conditions shown in Table VIII. The first four cases (Run IDs 3, 4, 5, and 6) represent a variation in temperature with all other conditions fixed. This type of parametric “temperature sweep” was designed to support comparison between experimental and computational results and was developed for research purposes. Run IDs 9 and 23 were directly scaled from App. C conditions, with Run ID 9 at a very cold temperature ( $-20.3\text{ }^{\circ}\text{C}$ ) and Run ID 23 at a temperature much closer to freezing ( $-5.4\text{ }^{\circ}\text{C}$ ). Air density was equivalent to an altitude approximately 1,400 ft

above sea level, as the IRT does not have altitude simulation capability.

The IRT test conditions were also used for posttest analysis of the CRM65 airplane icing scenarios. The first step was to relate the IRT test conditions back to the flight reference conditions shown in Table IX. The airplane angle of attack of  $3.7^\circ$  and reference speed of 232 kn were identical for all cases. The altitude associated with this holding condition was 10,000 ft above sea level. Icing scaling methods were used to determine the resulting values of static temperature, MVD, LWC, and exposure time. The temperature sweep noted for Table VIII is preserved in Table IX. Also, the exposure times associated with Run IDs 9 and 23 were set to 45 min to be consistent with airplane holding in App. C Continuous Maximum conditions. Following a similar workflow, a single flow solution using OVERFLOW (as described in Sec. 2.3) was obtained for this flight condition and then used as input to LEWICE3D for the various icing scenarios listed in Table IX. The results of the posttest CFD simulations were directly compared with the experimental results. An illustrative example is given in Figure 21 for the Midspan model. Plotted are the CFD and experimental pressure coefficients for the three rows of pressure taps at  $y = 18, 36,$  and  $54$  in. above the test-section floor. The 36-in. location represents the vertical center of the test section, halfway between the floor and ceiling. The  $x$  locations for the pressures are shown in inches relative to the model center of rotation. Because the leading edge of the model was swept back from the floor ( $y = 0$  in.) to the ceiling ( $y = 72$  in.), the  $x$  locations increase with the  $y$  location. The data show the increasing suction pressure on the leading edge working from  $y = 18$  in. outboard to  $y = 54$  in., consistent with the 3D CFD results presented in Figure 20. These pressure profiles exhibit a distinctive slope change on the lower surface (e.g., at  $x \approx -16$  in. for  $y = 36$  in.) that can be attributed to the transition from the full-scale leading-edge geometry to the aft section. This change in geometry can be seen in Figure 10 at  $x/c_{FS} \approx 0.12$ . There were also slope changes on the upper surface, such as at  $x \approx -25$  in. and  $-20$  in. for  $y = 36$  in. The changes in the pressure distribution were attributed to variations in the airfoil model surface coordinates resulting from the hybrid design process and transition from the full-scale leading edge to the aft section. The pressures measured on the flap indicated relatively high values of suction pressure due to the large flap angle of  $25^\circ$ . These pressures also indicate a full recovery to near-zero values of  $C_p$  at the trailing edge, suggesting little or no flow separation on the flap. The overall

agreement between the experimental data and CFD simulation results is generally good, with the largest differences occurring near the upper-surface suction peaks.

Given the importance of matching the attachment location between the CRM65 airplane CFB flight condition and the hybrid model in the IRT, the pressure data were heavily scrutinized near the highlight at the test-section centerline ( $y = 36$  in. above the floor). In this case, the  $C_p$  data are plotted as a function of the wrap distance, as shown in Figure 22. For the purposes of this work, the attachment location was defined as the location of maximum surface pressure. The target location shown in Figure 22 was at  $s = -1.34$  in. and was determined from the CRM65 airplane CFD simulation. Also shown for comparison with the experimental data is the pressure coefficient from the IRT model CFD. These data are the same as in Figure 21. The agreement here is considered to be very good, given all of the constraints associated with the hybrid model design, the effect of the tunnel walls, and accuracy of the 3D CFD. These results illustrate the value of pretest and posttest CFD simulations to ensure that the hybrid model performance in the IRT is consistent with the design approach taken at the outset.

TABLE VIII.—ICING RESEARCH TUNNEL RUN CONDITIONS FOR INBOARD, MIDSPAN, AND HYBRID MODELS

Run ID—Name	Angle of attack	Speed, kn	$T_{static}$ , °C	MVD, $\mu\text{m}$	LWC, $\text{g}/\text{m}^3$	Time, min
3—Venetian blind	$3.7^\circ$	130	-6.1	25	1.0	29
4—Maximum scallop	$3.7^\circ$	130	-8.6	25	1.0	29
5—Small gap	$3.7^\circ$	130	-11.0	25	1.0	29
6—Incomplete scallop	$3.7^\circ$	130	-13.5	25	1.0	29
9—Streamwise/rime	$3.7^\circ$	130	-20.3	25	0.6	23
23—WB33 direct App. C	$3.7^\circ$	130	-5.4	28	0.9	45

TABLE IX.—CRM65 AIRPLANE ICING FLIGHT CONDITIONS

Run ID—Name	Angle of attack	Speed, kn	$T_{static}$ , °C	MVD, $\mu\text{m}$	LWC, $\text{g}/\text{m}^3$	Time, min
3—Venetian blind	$3.7^\circ$	232	-8.0	20	0.55	29.2
4—Maximum scallop	$3.7^\circ$	232	-10.0	20	0.55	29.3
5—Small gap	$3.7^\circ$	232	-12.0	20	0.55	29.3
6—Incomplete scallop	$3.7^\circ$	232	-14.0	20	0.55	29.3
9—Streamwise/rime	$3.7^\circ$	232	-12.4	20	0.17	45
23—WB33 direct App. C	$3.7^\circ$	232	-6.0	20	0.51	45

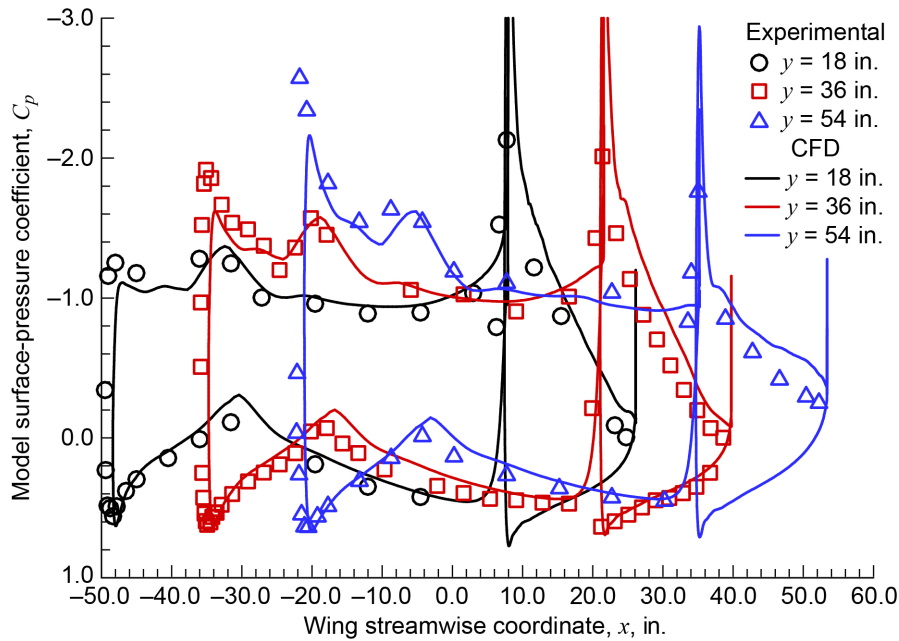


Figure 21.—Experimental and CFD surface-pressure distribution on Midspan model at  $\alpha = 3.7^\circ$ ,  $\delta = 25^\circ$ , 130 kn.

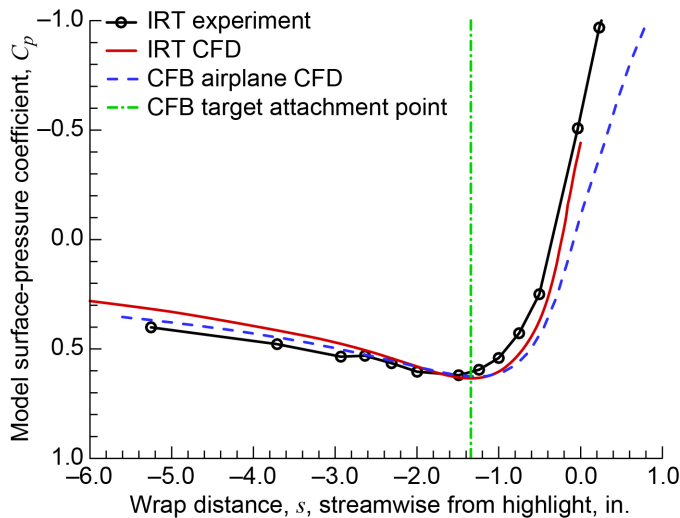


Figure 22.—Midspan model surface-pressure distribution plotted against streamwise wrap distance near attachment point at  $\alpha = 3.7^\circ$ ,  $\delta = 25^\circ$ , 130 kn.

A series of icing simulations were performed for each of the three hybrid models as installed in the IRT and for the CRM65 airplane at the relevant flight conditions. The parallel version of LEWICE3D with TRAJMC3D (version 2.4.80, released on April 27, 2014) was used for one set of simulations for the hybrid models as installed in the IRT. This set is referred to as “UW LEWICE3D IRT” because the results were generated at the University of Washington for the IRT models. A version of LEWICE3D modified within the Boeing Company was also

used for the IRT hybrid model simulations and for simulations of the CRM65 airplane. These two sets are referred to as “BC LEWICE3D IRT” and “BC LEWICE3D IFB,” respectively. All of the icing simulations utilized the 3D RANS CFD solutions described in the previous paragraph as input to LEWICE3D. The icing conditions are shown in Table VIII and Table IX. Three different drop distributions were used. The UW LEWICE3D IRT simulations used a 10-bin distribution based upon measurements by Papadakis et al. (Ref. 113). The BC LEWICE3D IRT simulations used a 7-bin distribution based upon the IRT 2015 cloud calibration (Ref. 69). The BC LEWICE3D IFB simulations used a Langmuir D 7-bin distribution. More information about these distributions can be found in Reference 76. LEWICE3D also allows the user to select an “ice density” value that attempts to account for the voids in the highly 3D accretions. Unless stated otherwise, an ice density value of  $450 \text{ kg/m}^3$  was used for all of the simulations described in this report. For the maximum scallop ice-shape conditions, a second set of simulations was performed with a density of  $350 \text{ kg/m}^3$ . Fujiwara, Bragg, and Broeren (Ref. 75) describe the effects of ice density variations on the resulting ice shape. For the run conditions tabulated in Table VIII and Table IX, the ice-accretion simulation results are shown in Figure 23 to Figure 29 along with photographs of the IRT ice accretions and the MCCS cuts derived from the 3D scans, as described in Section 2.2.

Run ID 3 results are shown in Figure 23. This “Venetian blind” ice accretion was so named because of the resemblance between the feather formations on the upper surface of the Inboard model

and the slats of a Venetian blind window treatment. All three photographs illustrate the large and highly 3D features associated with this set of icing conditions. The ice-shape cross-section plots reveal some important trends. First, there is excellent agreement between the BC LEWICE3D IFB results and the BC LEWICE3D IRT results for the Midspan and Outboard models. This agreement provides assurance that the hybrid model performance was consistent with the design approach taken at the outset. For all three models, the UW LEWICE3D IRT results differ significantly from the other two BC LEWICE3D results. This difference was not investigated in detail but is related to certain changes incorporated into LEWICE3D within the Boeing Company to improve the modeling of ice accretion at higher speeds. Comparison with the IRT MCCA shape yields another set of observations. For the Midspan and Outboard models, the UW LEWICE3D IRT results matched the upper-surface horn thickness fairly well, whereas the BC LEWICE3D simulations resulted in a much shorter upper-surface ice horn but had a larger angle located farther downstream on the upper surface that matched the IRT MCCA horn angle better. In the case of the Inboard model, none of the simulation results matched the experimental MCCA very well, with one exception: the angle and location of the upper-surface horn from the BC LEWICE3D IRT simulation were well matched to those of the IRT MCCA, thus illustrating a potential improvement in the Boeing Company version of LEWICE3D.

The Run ID 4 results are shown in Figure 24. This “maximum scallop” ice accretion was so named because of the clearly defined scallop (or lobster tail) features shown in the photographs. As noted earlier in this section, the only change in icing conditions between these results and those for Run ID 3 (Figure 23) was a reduction in static temperature from  $-6.1$  to  $-8.6$  °C (for the IRT conditions) that led to the formation of the distinct scallop features. These conditions resulted in an increase in the overall size of the MCCA profiles on each of the models as compared with the results shown in Figure 23. Beginning with the Outboard model results, trends similar to those noted for Figure 23 were observed. There was excellent agreement between the BC LEWICE3D IFB and BC LEWICE3D IRT simulation results. The angle and location of the upper-surface horn were fairly well matched to the experimental data, although the horn itself was significantly smaller. In contrast, the upper-surface horn thickness of the UW LEWICE3D IRT result was similar to that of the experimental IRT MCCA result, but the angle was significantly lower. Similar trends were observed on the Midspan model but with slightly less favorable comparisons. Once again, the worst overall agreement between the simulation and experimental results occurred on the Inboard model.

An additional set of UW LEWICE3D and BC LEWICE3D simulations was performed for the Run ID 4 maximum scallop conditions using an ice density value of  $350 \text{ kg/m}^3$ . These

results are shown in Figure 25. A comparison with the results in Figure 24 indicates that the main effect of the decrease in ice density was to increase the ice volume, which was apparent from the increase in ice horn thickness. The angle was not significantly affected. This increase in horn thickness provided a slightly better comparison with the IRT MCCA results, and therefore, the LEWICE3D-based artificial ice shapes developed for aerodynamic testing were based upon these results with the ice density set to  $350 \text{ kg/m}^3$ .

The Run ID 5 results shown in Figure 26 represent a further reduction in static temperature to  $-11.0$  °C (for the IRT conditions), which had the effect of reducing the size of the scallop features and closing some of the large gaps between these features. For the Outboard model it can again be seen that there was good agreement between the BC LEWICE3D IFB and IRT simulations. However, in this case, the upper-surface horn angle did not compare well with the IRT MCCA results, the former being at a lower angle relative to the latter. For the Midspan model, the BC LEWICE3D IRT results had a better match of upper-surface horn angle to the IRT MCCA results. Interestingly, on the Inboard model, all three of the LEWICE3D simulation results compare favorably among each other, but not particularly well with the IRT MCCA.

The results of a further decrease in temperature to  $-13.5$  °C (for the IRT conditions) are reported in Figure 27 for Run ID 6. The effect of this decrease on the ice accretion can clearly be seen in the photographs, where the ice is much more solid and does not exhibit the clearly defined scallop type features observed at the warmer temperatures. Once again on the Outboard model, the BC LEWICE3D IFB and IRT results agree very well. For the Midspan model, there is a greater difference between the BC LEWICE3D IFB and IRT simulations, whereas the former agrees fairly well with the UW LEWICE3D IRT result. For the Inboard model, the results of all three LEWICE3D simulations are consistent. With respect to comparison of the LEWICE3D simulation results with the experimental data, the overall size of the ice shape is better matched than in the preceding figures for the Midspan and Outboard models; this is most likely attributable to the colder temperature, which minimizes the surface water flow that must be predicted computationally. For the Inboard model, however, the experimental comparison was still poor.

The Run ID 9 results shown in Figure 28 were for a rime ice condition that was based upon an App. C Continuous Maximum condition for holding flight. As indicated in the photographs, the cold temperature and lower LWC resulted in a much more solid rime-type ice. However, on the Inboard model, the ice accretion was still characterized by large individual feather features. As expected for this set of conditions, there was much better agreement among the various cross-section results. It can be noted for the Inboard model that the LEWICE3D simulations all resulted in shapes that were slightly smaller than the IRT MCCA.

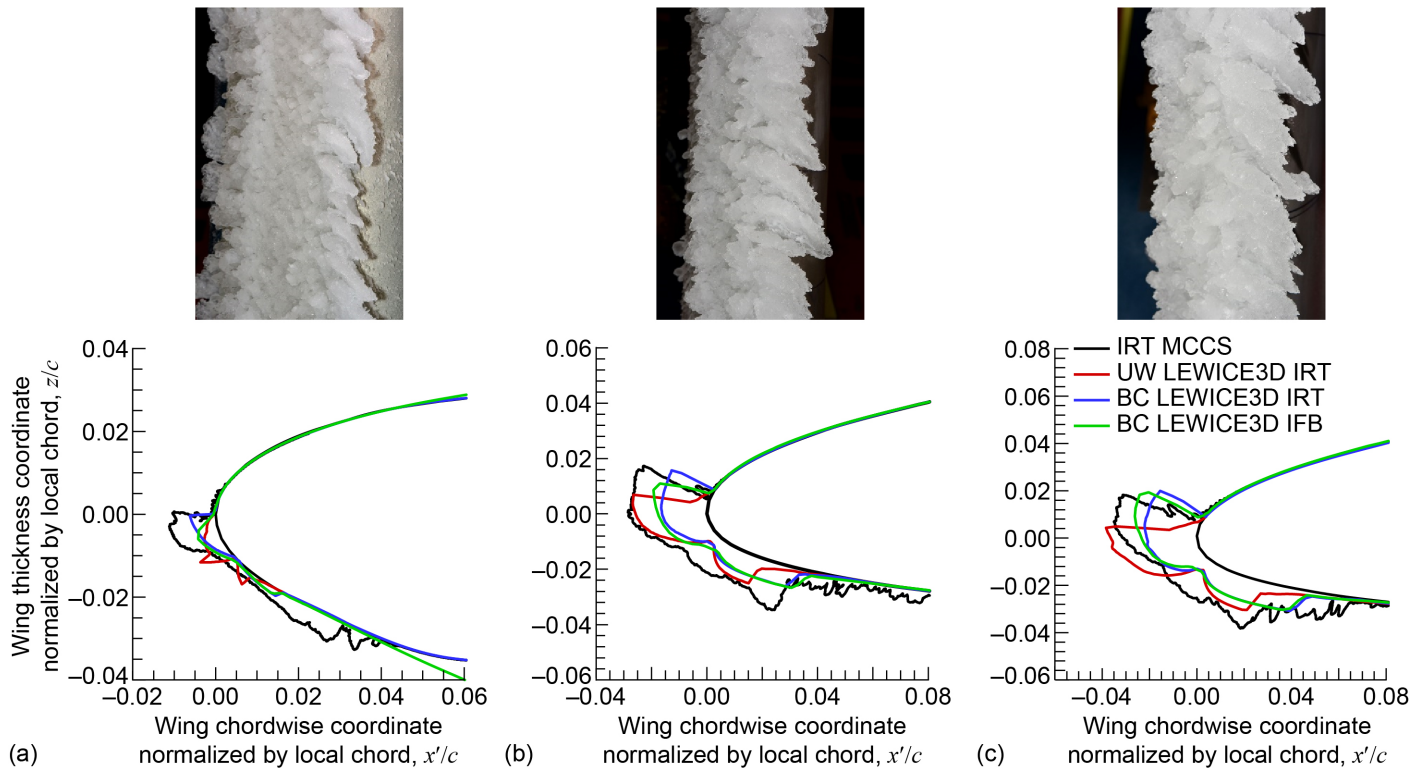


Figure 23.—Run ID 3 Venetian blind ice-accretion comparison of ice accretion photographs (top) and simulation results (bottom) for three hybrid models and stations of CRM65 wing. (a) Inboard. (b) Midspan. (c) Outboard.

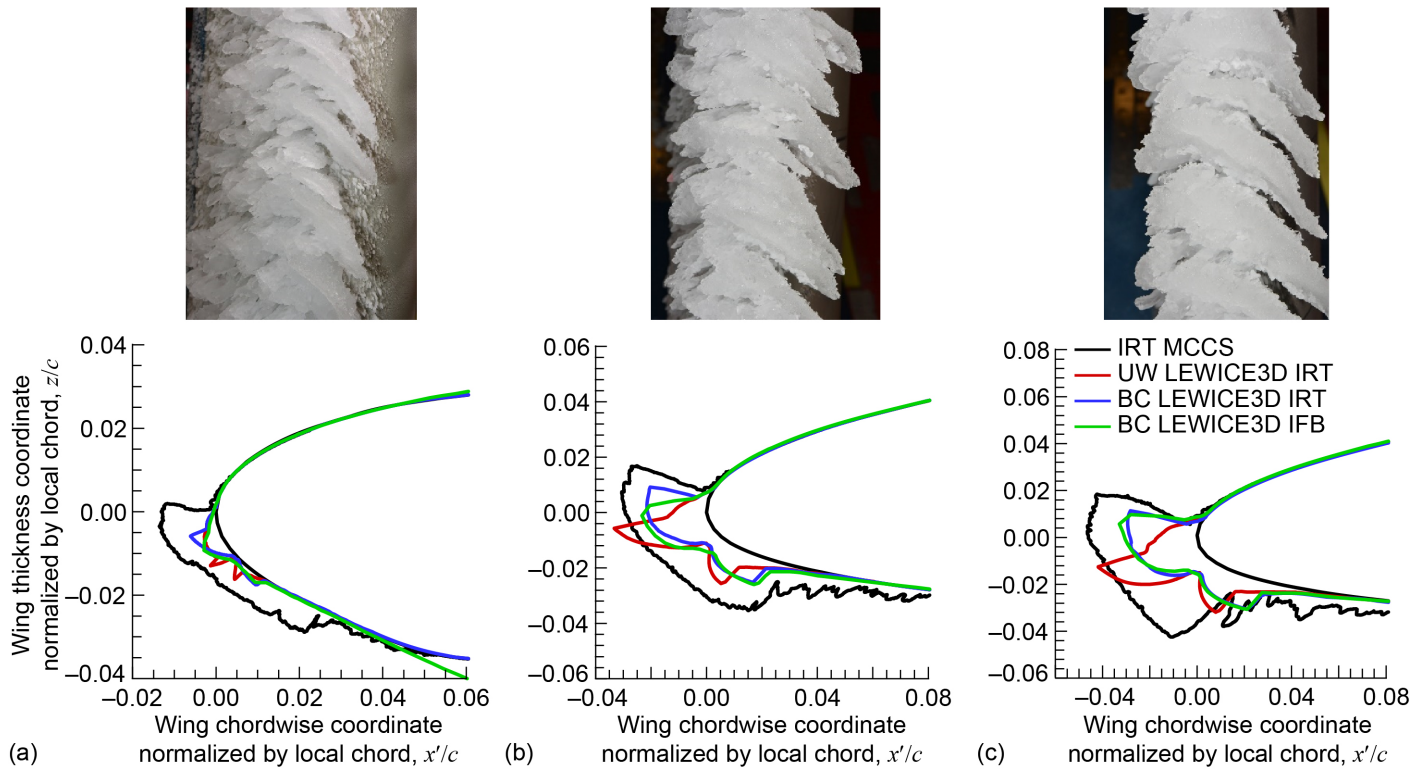


Figure 24.—Run ID 4 maximum scallop ice-accretion comparison of ice accretion photographs (top) and simulation results (bottom) for three hybrid models and stations of CRM65 wing. (a) Inboard. (b) Midspan. (c) Outboard.

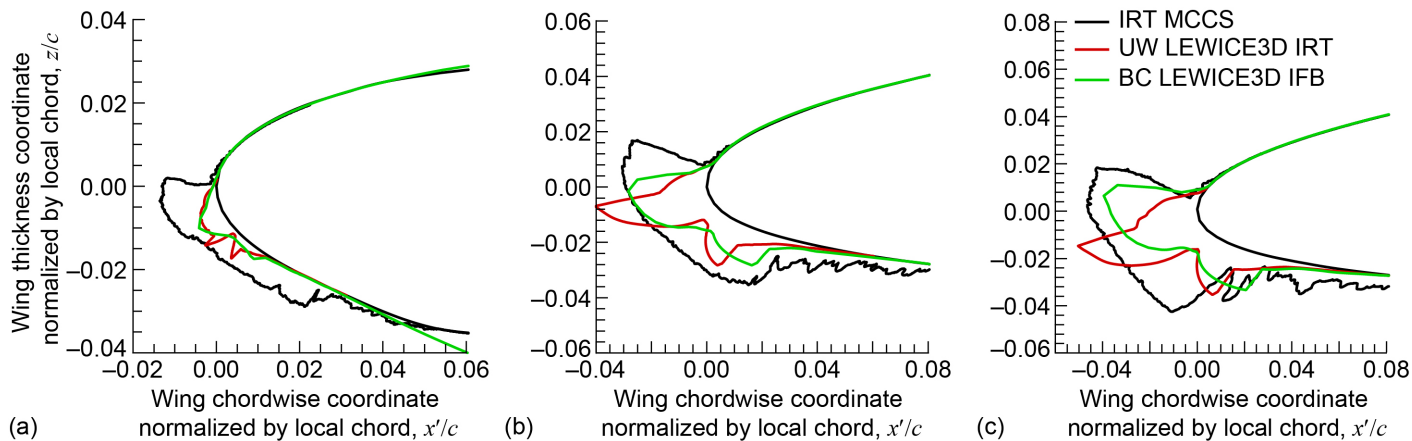


Figure 25.—Run ID 4 maximum scallop comparison of IRT experimental MCCS and LEWICE3D simulation results with ice density = 350 kg/m<sup>3</sup> for three hybrid models and stations of CRM65 wing. (a) Inboard. (b) Midspan. (c) Outboard.

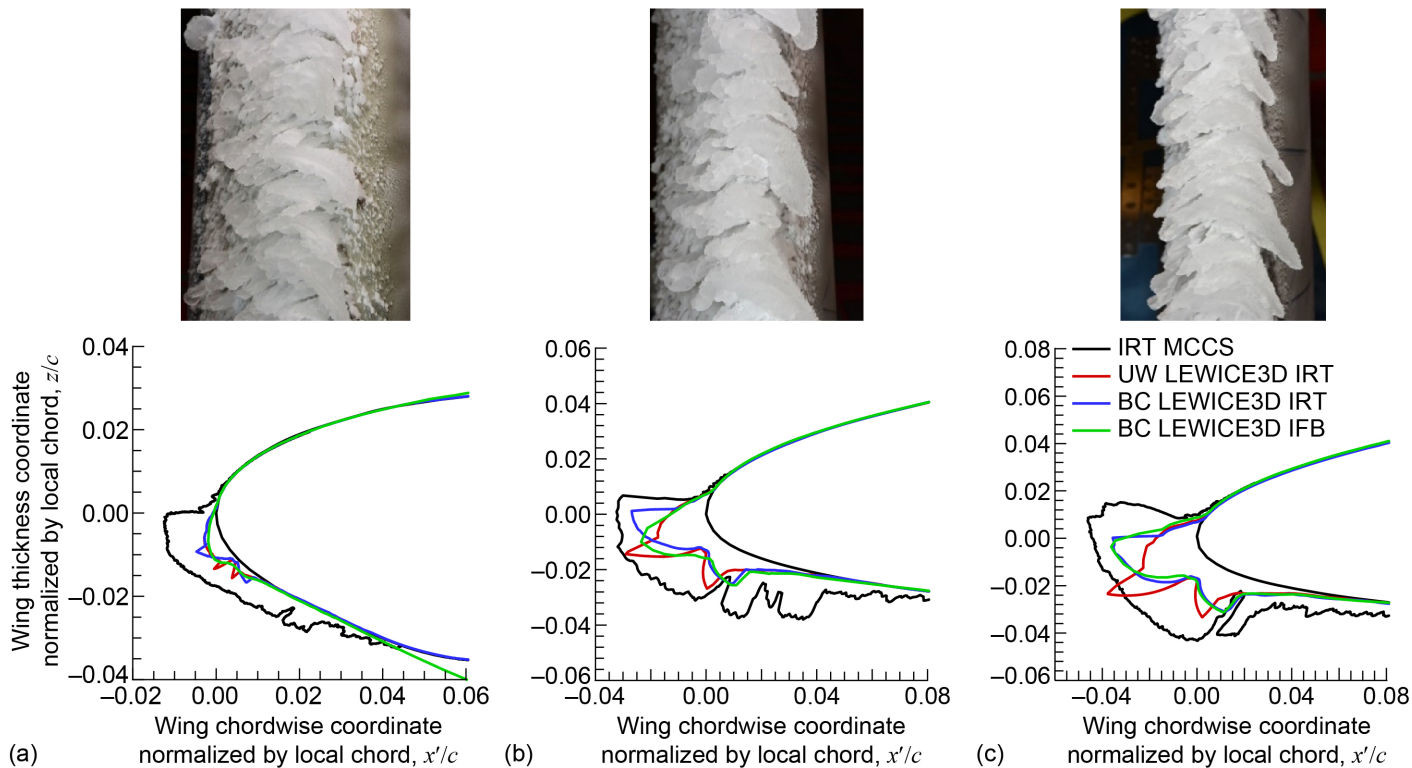


Figure 26.—Run ID 5 small gap scallop comparison of ice-accretion photographs (top) and simulation results (bottom) for three hybrid models and stations of CRM65 wing. (a) Inboard. (b) Midspan. (c) Outboard.

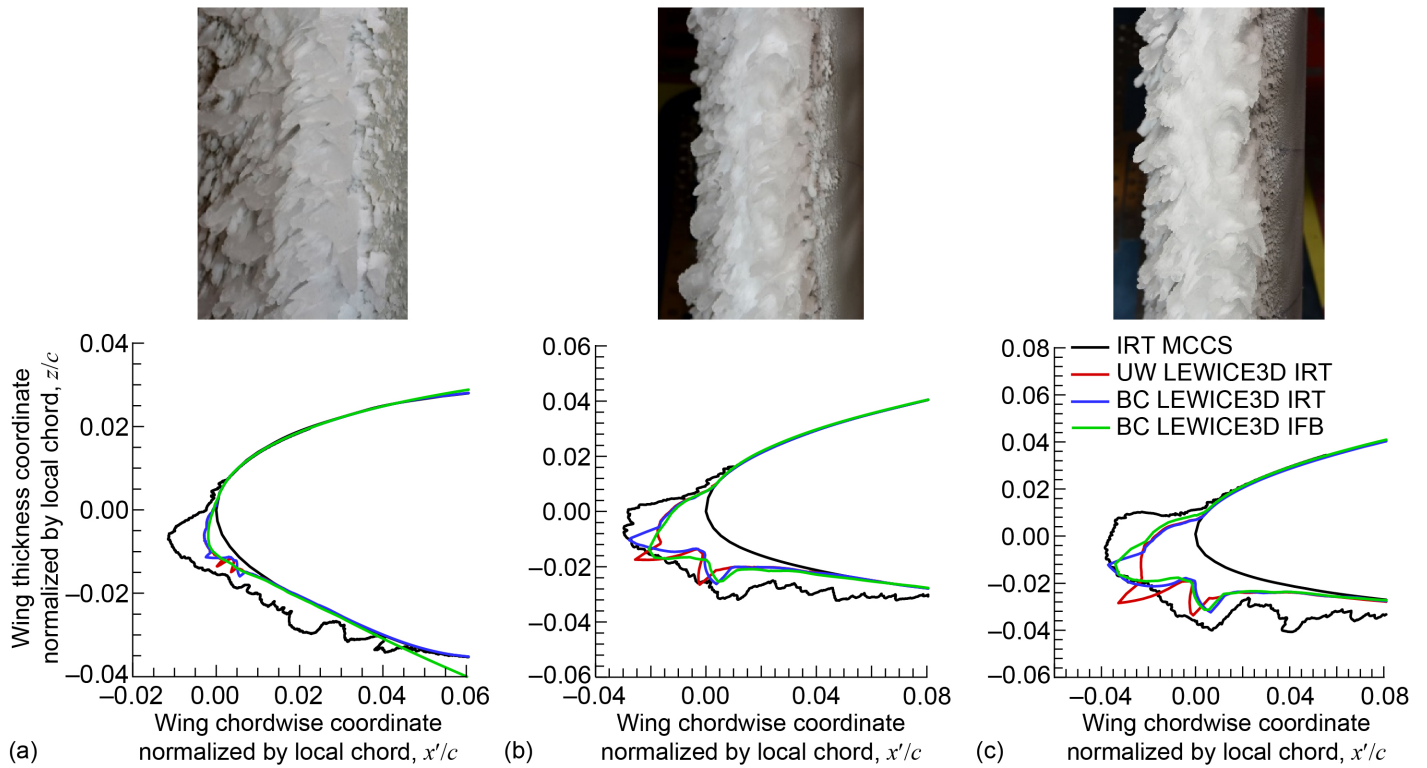


Figure 27.—Run ID 6 incomplete scallop comparison of ice-accretion photographs (top) and simulation results (bottom) for three hybrid models and stations of CRM65 wing. (a) Inboard. (b) Midspan. (c) Outboard.

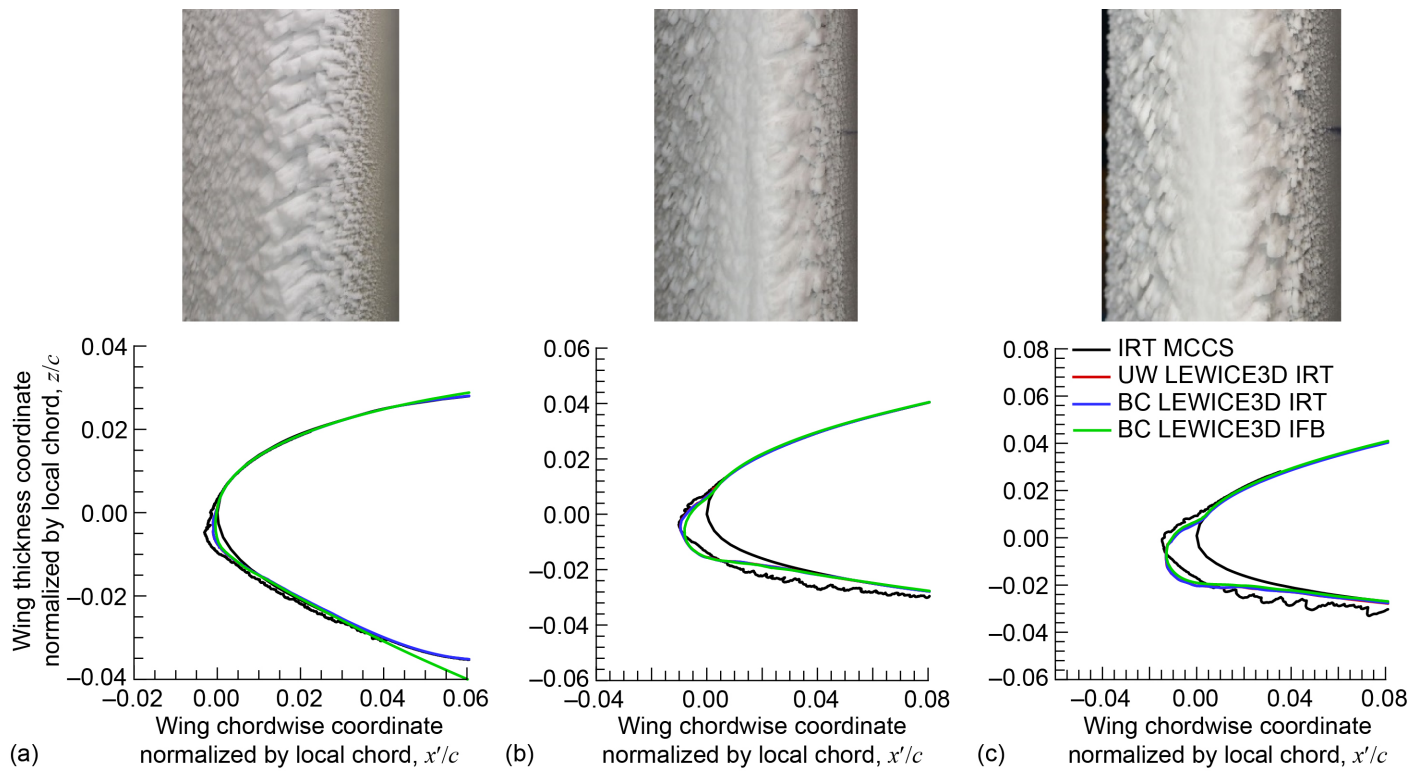


Figure 28.—Run ID 9 streamwise/rime comparison of ice-accretion photographs (top) and simulation results (bottom) for three hybrid models and stations of CRM65 wing. (a) Inboard. (b) Midspan. (c) Outboard.

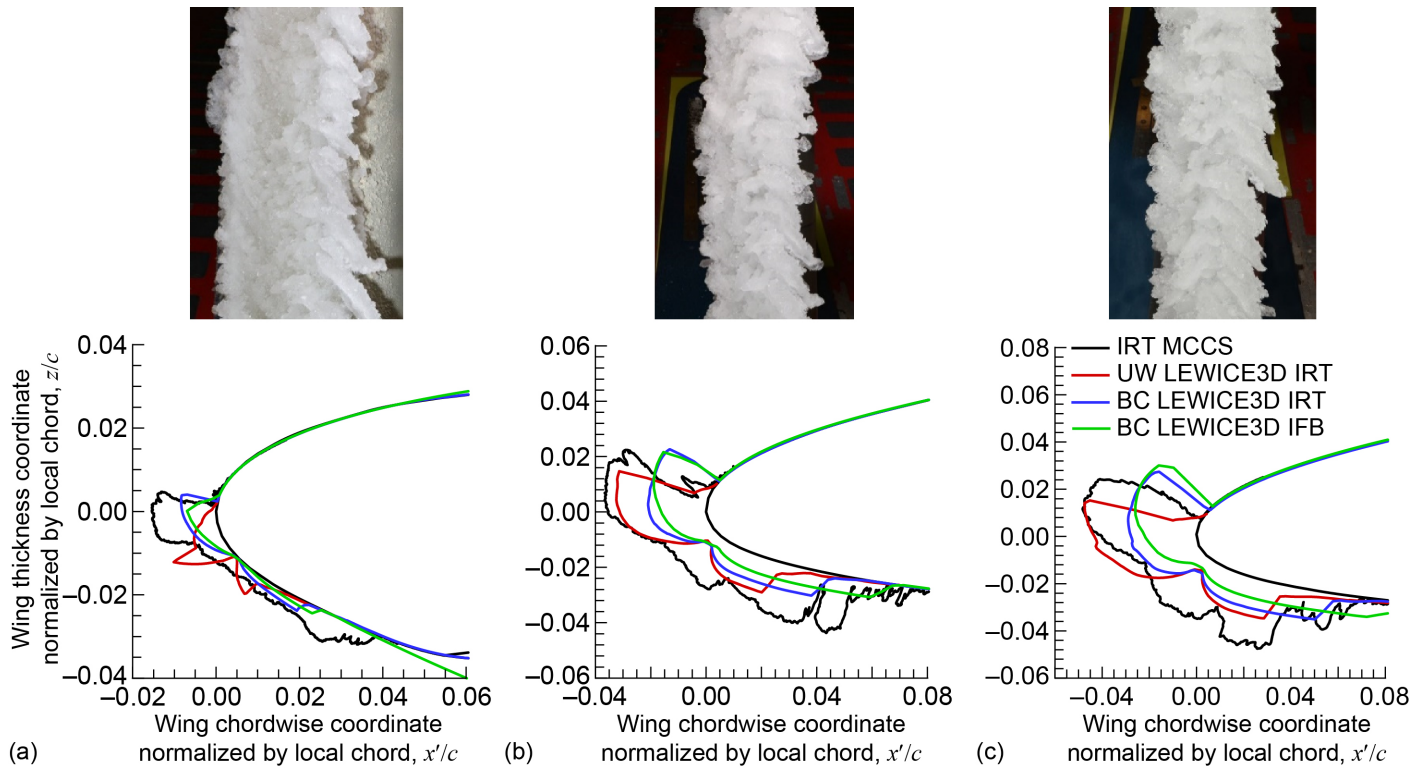


Figure 29.—Run ID 23 WB33 comparison of ice-accretion photographs (top) and simulation results (bottom) for three hybrid models and stations of CRM65 wing. (a) Inboard. (b) Midspan. (c) Outboard.

The Run ID 23 results shown in Figure 29 were also based upon an App. C Continuous Maximum condition at a warmer temperature. The resulting ice accretion was similar in some respects to that for Run ID, 3 shown in Figure 23. This was considered to be a glaze, horn-type ice shape with large 3D features. The cross-section plots clearly illustrate the large horn that formed on the upper surface in these conditions. The computational results were similar to those identified for Run ID 3, where there was generally excellent agreement between the BC LEWICE3D IRT and IFB results. For the Midspan and Outboard models, the UW LEWICE3D IRT results matched the upper-surface horn thickness fairly well, whereas the BC LEWICE3D IRT and IFB simulations resulted in a smaller upper-surface horn with a larger angle that exceeded the angle of the IRT MCCS ice shape. For the Inboard model, the BC LEWICE3D IRT and IFB simulations were better matched with the IRT MCCS ice shape for horn angle.

ONERA ran IGLOO3D computations on a subset of the same ice-accretion database, as described by Radenac et al. (Refs. 77 and 78). The aerodynamic computations with elsA were qualified by satisfactorily comparing against experimental measurements of pressure. The agreement between the heat transfer coefficient produced by LEWICE3D and IGLOO3D was also verified for Run ID 9 conditions of Table VIII for the Midspan hybrid model. Agreement was found to be good

except in the vicinity of the separation line, where the IGLOO3D result was fully turbulent but the LEWICE3D result had a small laminar area. Regarding drop trajectory simulations, a 10-bin distribution based upon measurements by Papadakis et al. (Ref. 113) was used for IGLOO3D. This distribution is identical to the one used for the UW LEWICE3D IRT simulations described earlier in this section. LEWICE3D and IGLOO3D also produced very similar collection efficiency despite slight differences in impingement limits and maximum collection efficiency. These discrepancies may be due to differences in mesh refinements and aerodynamic solutions.

An investigation of the Inboard model is presented in Reference 77; this report, like Reference 78, focuses primarily on the Midspan model. Figure 30 to Figure 33 show a comparison among IGLOO3D results (three cuts were defined in the spanwise direction to check the uniformity of the predicted ice shape), UW LEWICE3D IRT results, and the experimental ice shapes for Run IDs 5, 6, 9, and 23 of Table VIII. The ice density of IGLOO3D was manually adjusted to  $450 \text{ kg/m}^3$ , except for one simulation of Run ID 23 that will be discussed later in this section. Regarding the experimental ice shapes, all the scanned points are reported in the figures. The outer envelope of these points is comparable to the MCCS shown in Figure 23 to Figure 29. An average ice shape, also shown in the figures, was derived from the scan data

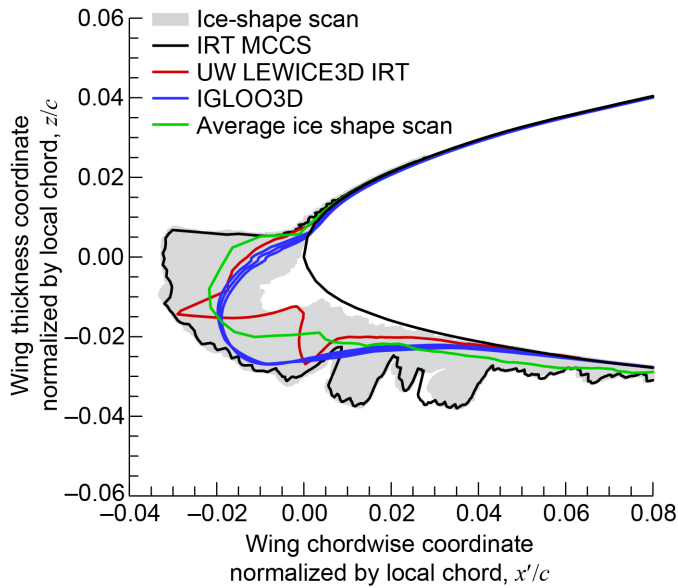


Figure 30.—Run ID 5 small gap scallop ice-shape comparison of IGLOO3D, LEWICE3D, and IRT experimental results for Midspan hybrid model.

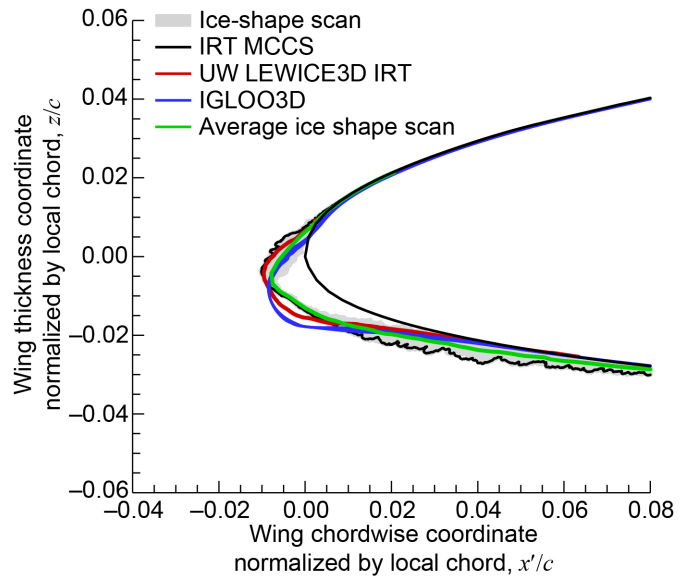


Figure 32.—Run ID 9 streamwise/rime ice-shape comparison of IGLOO3D, LEWICE3D, and IRT experimental results for Midspan hybrid model.

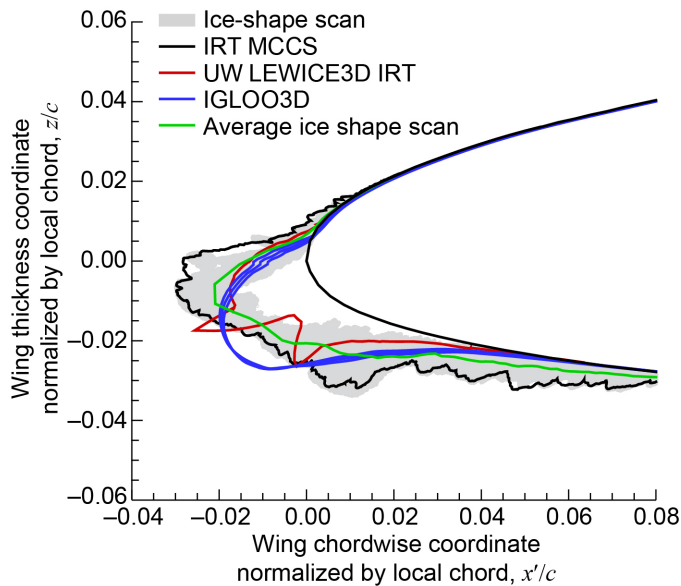
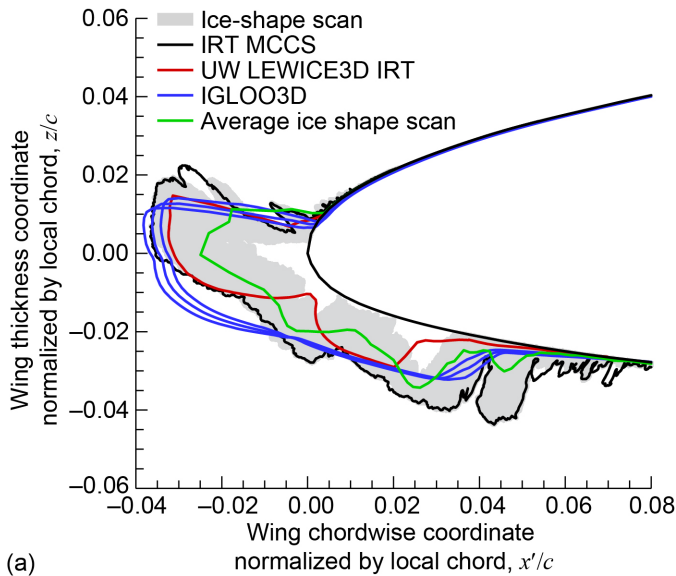


Figure 31.—Run ID 6 incomplete scallop ice-shape comparison of IGLOO3D, LEWICE3D, and IRT experimental results for Midspan hybrid model.

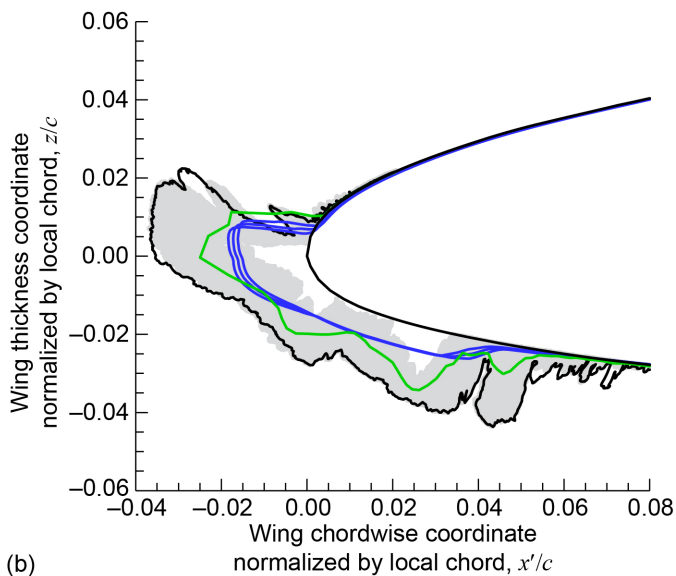
as follows: First, the local normal ice thickness relative to the clean wing surface was computed for each point in the ice scan. Next, the cross section was uniformly discretized in the  $z$ -direction into 100 points. Each of these points was treated as the center of a spanwise-running bin. Finally, the average ice thickness was determined as the arithmetic mean of the local normal thickness values in each bin.

Except in the vicinity of the attachment line, the numerically predicted ice shapes were generally more similar to the average ice shape than to the MCCA, as shown in Figure 30 to Figure 33. For Run IDs 5 and 6 (Figure 30 and Figure 31), LEWICE3D produced glaze ice, as shown by the presence of typical ice horns. Such glaze ice shapes were expected, but IGLOO3D produced rime ice. The laminar–turbulent transition modeling and the roughness size modeling are two possible reasons for this discrepancy. None of the computations captured the characteristic ice shapes obtained experimentally (with a scallop-like structure in the spanwise direction). The simple control-volume, bulk-flow approach of the Messinger model used for these simulations does not allow for producing the spanwise variations of ice thickness.

For the streamwise/rime ice case Run ID 9 (Figure 32), the agreement between IGLOO3D, LEWICE3D, and the experiments was good, but the simulations predicted too much ice at the attachment line. For Run ID 23 (Figure 33), IGLOO3D and LEWICE3D both predicted glaze ice. For this case, it was better to employ the baseline ice density ( $917 \text{ kg/m}^3$  in glaze conditions) rather than the manually adjusted bulk density ( $450 \text{ kg/m}^3$ ) to capture the average ice shape. The average ice shape (location of the upper-surface ice horn and overall distribution of ice) is better predicted by IGLOO3D when an ice density of  $917 \text{ kg/m}^3$  was used. Only the voids in the scallop-like structure are not captured. This suggests that the manually adjusted bulk ice density is more suited to match the MCCA (and to model the voids in the highly 3D structure on the maximum ice thickness).



(a)



(b)

Figure 33.—Run ID 23 WB33 ice-shape comparison of IGLOO3D, LEWICE3D, and IRT experimental results. (a) Ice density =  $450 \text{ kg/m}^3$ . (b) Ice density =  $917 \text{ kg/m}^3$ .

### 3.1.3 Ice-Shape Comparison

The ice-shape comparisons shown in the previous section yielded a number of observations and recommendations related to the evaluation or validation of ice-prediction tools such as LEWICE3D and IGLOO3D. In a number of cases, there were significant differences in the ice shapes generated from the numerical tools. To better understand the sources of these differences, comparisons of surface pressure, collection efficiency, heat transfer coefficient, and ice density models should be performed. Preliminary comparisons are shown by Radenac et al. (Ref. 78), but a more systematic and detailed comparison is required and was simply beyond the scope of this

research effort. In some cases, particularly for warmer temperatures, the simulation-based ice shapes tended to underpredict the experimental ice shapes defined by the MCCS. For the IGLOO3D simulations with an ice density of  $450 \text{ kg/m}^3$ , the code results better matched the average ice-shape cross section. These observations are consistent with the inability of the icing codes to account for the numerous voids and individual feather or scallop features of the experimental ice accretion. This suggests that an alternate approach to ice-accretion modeling may be required if it is necessary to capture these features in the simulation.

Another common trend in the comparison of the simulation and experimental ice shape results was that the poorest agreement occurred for the Inboard model. This trend may indicate some type of systematic problem with the numerical models, an effect of the large model on the icing cloud in the IRT, or some combination of these factors. The Inboard model was nearly twice the size of the Midspan and Outboard models and operated at a higher local angle of attack. It is possible that these conditions had an upstream influence on the icing cloud, such as to alter the calibrated value of LWC. The large leading-edge radius associated with the Inboard model may introduce additional challenges for the local roughness and heat transfer numerical simulation models that have typically been developed with and based on correlation of data from smaller radius leading-edge geometries.

The ice-shape comparisons also provide a strong motivation for the aerodynamic research that addressed the other major objectives of this research effort. The comparisons described in this section were largely qualitative, using terminology such as “good” and “poor.” In addition, the experimental ice accretions were highly 3D, whereas the icing code results were primarily 2D; it is therefore very important to understand the effect of this additional three-dimensionality on the aerodynamics. It was also observed in some cases that the codes might be able to match the thickness, angle, or location of an upper-surface ice horn, but typically not all three geometric attributes. Understanding more about the aerodynamic impact of such features is critical to evaluating the overall efficacy of an ice-accretion code. The question this kind of analysis seeks to answer is a simple one: “How good is good enough?” In other words, “How closely must a predicted ice shape match experiment?” The aerodynamic portion of this research effort was designed to address this and related questions. The major outcomes are reported in Sections 3.2 and 3.3.

### 3.1.4 Generation of Artificial Ice Shapes

The ice-shape geometries described in the preceding section were used to generate artificial ice shapes for aerodynamic testing. The 3D high-fidelity artificial ice shapes were based upon the 3D scans and were created using a morphing process

described in Section 2.4.6 and in References 92 and 94. The lower fidelity 3D smooth ice shapes were created based upon lofted section cuts of the experimental ice shapes (similar to the MCCS) and, in some cases, for the computational ice shapes. This process yielded several important results.

For the high-fidelity ice shapes, implementation of the morphing process introduced a repeated pattern along the span of the wing. This discontinuity may have triggered the repeating flow patterns observed in some of the surface oil flow visualization results described in Section 3.2.3. It may be important to blend the intersection between morphed segments to minimize any such discontinuities, but this would probably require manually contouring the ice shape at the intersections and could be very time consuming. A risk-mitigation approach may be more practical, where at least one ice shape with the intersections blended is created and tested to see how it compares with the original, nonblended ice shape. Another option would be to investigate new processes for generating a full-span ice shape that would not require creating segments of quasi-repeated ice shapes. One observation here is that the Geomagic software did not allow for much user control of the weighted averaging process used during the morphing. A more advanced or more capable software might have allowed for greater preservation of the surface textures and features. The high-fidelity artificial ice-shape geometries were also limited, to a certain extent, by the available computing power. If higher levels of detail are needed in the artificial ice shapes, then faster computers with more memory are required. There could also be file-size limitations on the manufacturing side; this must also be investigated to ensure that the ice-shape manufacturer can handle very large geometry files.

The artificial ice shapes tested on the WSU model were composed of two spanwise segments; on the F1 model, they were composed of three spanwise segments. The junction between these artificial ice-shape segments had butt joints, and the junction between the segments and the wing surface had lap joints. The butt joints may have allowed some air leakage in spite of extensive efforts to seal the joints with clax (clay combined with wax), modeling clay, and tape. This was primarily an issue with the lower fidelity artificial ice shapes, where anomalies were observed in the surface oil flow visualizations. Therefore, it is recommended to incorporate lap joints for the mating segments of the artificial ice shapes where possible. (It is very difficult to create lap joints in high-fidelity shapes, but this should rarely be necessary.) A related problem involved mating of the SLA parts to each other and to machined model surfaces. The lower accuracy of the SLA parts required significant fit-checking and hand work to establish a proper fit. These issues might have been avoided with more accurate rapid prototyping or additive manufacturing methods. Another issue with SLA is the long-term stability of the finished parts when

exposed to UV light and humidity. Exposure to humidity can result in significant dimensional changes to the finished parts, including bending and warping. Considerable effort was dedicated to minimizing these effects. This included storing the ice-shape segments in Mylar® (DuPont Teijin Films™) polyester film bags to eliminate UV exposure and sealing desiccant inside to minimize humidity. These efforts, while sometimes time consuming and cumbersome, greatly extended the useful life of the artificial ice shapes.

As noted in Section 2.4.6, hemispherical roughness features were incorporated into 3D smooth ice shapes. The hemispherical geometry does not strictly satisfy the recommendations for roughness particle density from FAA AC 25-25A (Ref. 100). A cone geometry was investigated. This geometry matched the recommendation exactly, but modeling the array of cone geometries proved very difficult and was also hampered by limitations with available computing power. Additionally, in 3D printing trials, the cones were found not to be as sharp as desired at the scale needed for aerodynamic testing. The cones did not appear significantly different from the hemispheres when printed.

## **3.2 Understanding of Iced Swept-Wing Aerodynamics**

This section summarizes the key elements of this research effort that have greatly improved the understanding of iced swept-wing aerodynamics. This specifically includes the effects of Reynolds and Mach numbers, key flow-field features, and significant differences from 2D iced-airfoil aerodynamics. However, it is important to bear in mind that this understanding was built on what is, in many ways, a preliminary set of data. This and other limitations are addressed first.

### **3.2.1 Assumptions and Limitations of the Study**

In analyzing these results, it is important to recognize several limitations of the current study and, consequently, of this data set. Swept-wing geometry is very complex. To define a swept wing, parameters such as sweep angle, twist, planform shape, aspect ratio, taper ratio, and airfoil sections are needed. The aerodynamic performance of a swept wing depends on and is unique to the specific values of these parameters. A simple example is the dependence of the leading-edge vortex on the wing sweep. The effect of ice accretion and ice-accretion fidelity on the formation of the leading-edge vortex, or the delay in this formation, was shown to be an important feature in the iced aerodynamic performance of the CRM65 wing. Wings of other sweep angles are expected to have different sensitivity to the leading-edge vortex formation and will thus be affected differently by leading-edge ice shapes. In addition, this study was limited to an examination of the effect of ice-accretion

shapes on one specific and relatively simple swept-wing geometry; the CRM65 swept-wing configuration tested in this study had no engine or pylon, no flaps or control surfaces, and no wingtip devices. Lynch and Khodadoust (Ref. 90) point out in their extensive review of aircraft and wing icing aerodynamics that the proper assessment of 3D icing effects relies on an understanding of the spanwise variation in stall initiation on the clean wing. They note that 3D wings have a spanwise location that is critical to stall initiation. The addition of wing-mounted engines, nacelles, and pylons can also modify the stall behavior. Therefore, it is important to know the critical section, span-load distribution, baseline wing stalling characteristics, and how ice accretion affects the stall progression relative to the critical section. All of this will vary from aircraft to aircraft and even with different configurations of the same aircraft.

The number and types of ice shapes tested were also limited. Most of this analysis is built upon two large, leading-edge ice shapes. Other icing conditions and ice shapes could potentially yield different results and different conclusions. So while the current study contributes a wealth of data and an extremely valuable data set of ice shapes and aerodynamic results, it is not comprehensive in terms of swept-wing geometry or ice shapes. Care must be used in extrapolating results beyond the range of parameters tested.

### 3.2.2 Reynolds and Mach Number Effects

Aerodynamic performance testing was conducted at the ONERA F1 wind tunnel to exploit the capability of this pressure tunnel to achieve higher Reynolds number than could be obtained in an atmospheric 7- by 10-ft wind tunnel. In addition, the ONERA F1 wind tunnel allows for the capability to vary Reynolds and Mach number independently to quantify these effects on the iced swept-wing aerodynamics. Angle-of-attack sweeps were performed over a Reynolds number range of  $1.6 \times 10^6$  to  $11.9 \times 10^6$  and a Mach number range of 0.09 to 0.34. Force balance and surface pressure data were acquired. Mini-tuft flow visualization was also performed during the performance sweeps. Five different ice-shape configurations were investigated, and for three of these configurations, lower fidelity simulations were also built and tested. The effect of Reynolds and Mach number based on these tests is presented in detail in Broeren et al. (Ref. 82) and Woodard et al. (Ref. 101).

The conclusions regarding the effect of Reynolds and Mach number on aerodynamic performance were based upon the analysis of four parameters defined in Section 2.4.3: maximum lift coefficient  $C_{L,max}$ , usable lift coefficient  $C_{L,use}$ , minimum drag coefficient  $C_{D,min}$ , and drag coefficient at a lift coefficient equal to 0.6,  $C_{D,0.6}$ . The usable lift coefficient was based upon an analysis of the wing pitching moment as indicative of stall progression on the wing. This parameter was developed, in part,

because in many cases for the iced-wing configurations, the stalling angle associated with maximum lift was higher than the clean-wing stall angle. This represents a fundamental difference from past research on straight wings or airfoils with large, leading-edge artificial ice shapes, where the stall angle was typically lower than the clean value.

Figure 34 and Figure 35 show the effect of Reynolds and Mach number on the clean-wing  $C_L$ ,  $C_M$ , and  $C_D$  versus angle of attack for three Reynolds number and four M. Clear dependence of the aerodynamic performance on Reynolds and Mach number is seen particularly at high  $\alpha$  for lift and moment. Less dependence is seen for drag, especially versus Mach number. Figure 36 and Figure 37 show  $C_L$ ,  $C_M$ , and  $C_D$  versus angle of attack for four Reynolds and Mach numbers on the CRM65

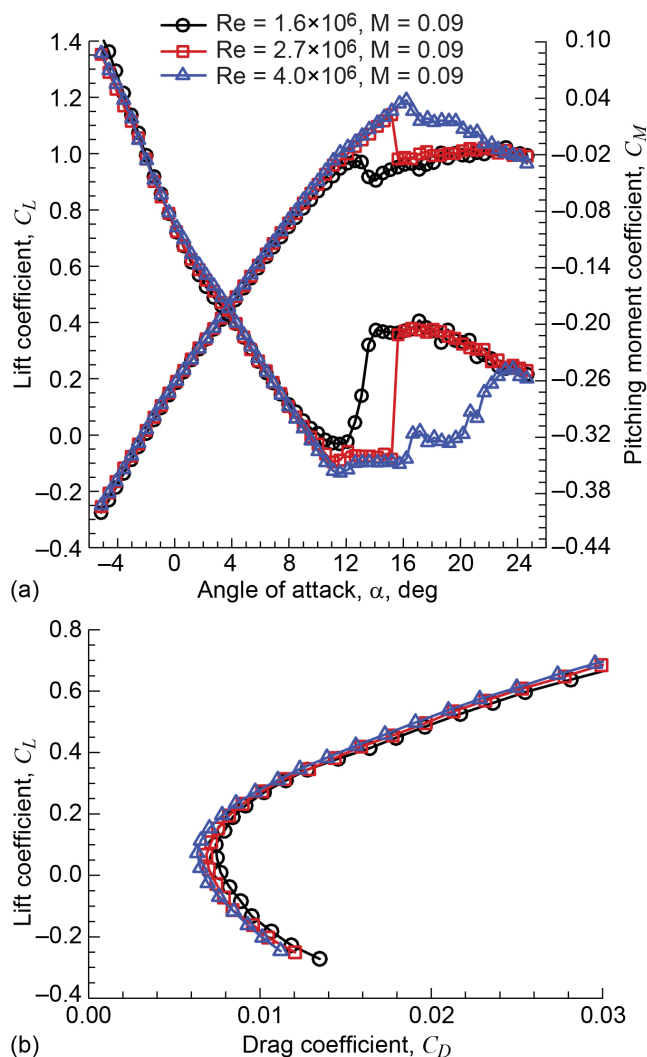
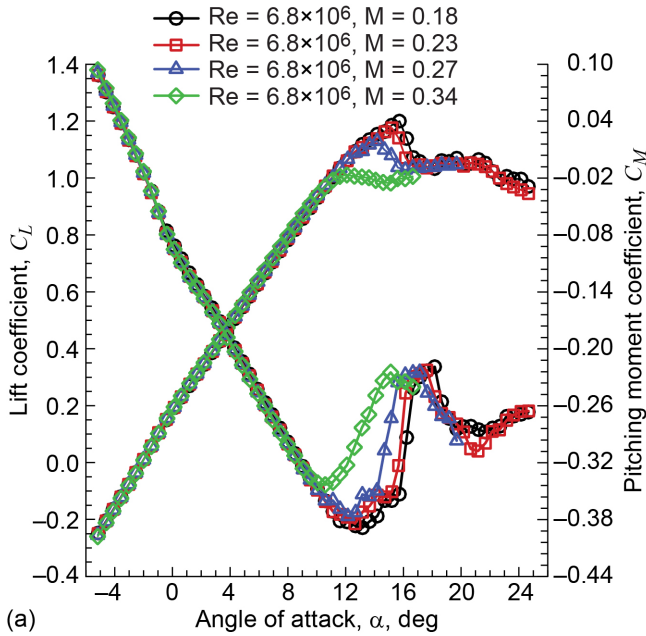
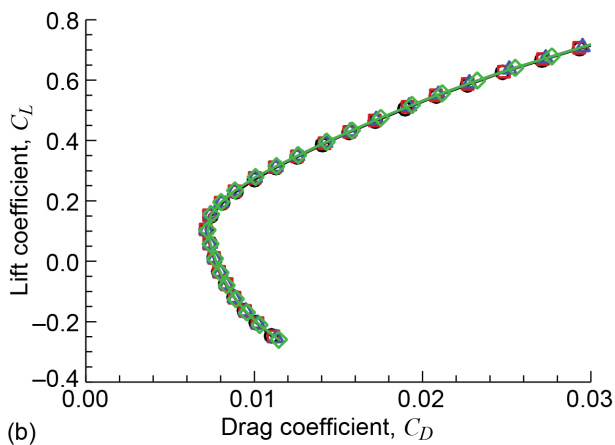


Figure 34.—Effect of Reynolds number of clean CRM65 wing performance at M = 0.09. Data from F1 wind tunnel with 13.3-percent-scale model. (a) Lift and pitching moment coefficients plotted versus angle of attack. (b) Lift coefficient plotted versus drag coefficient.

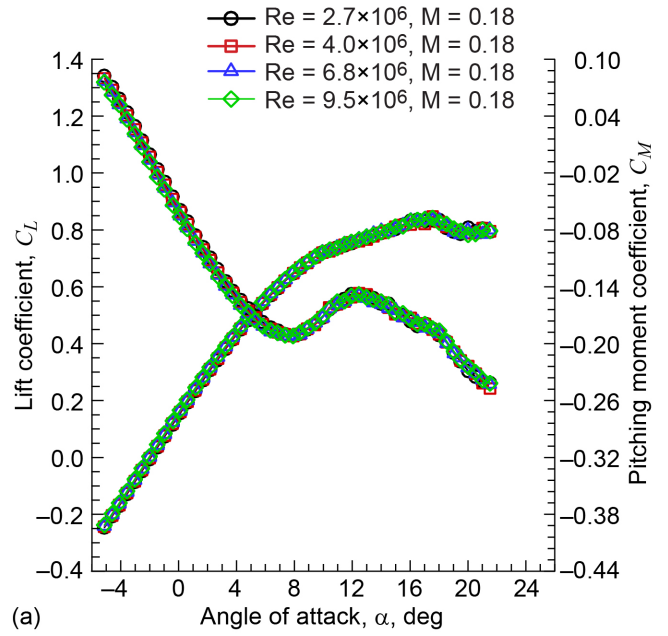


(a)

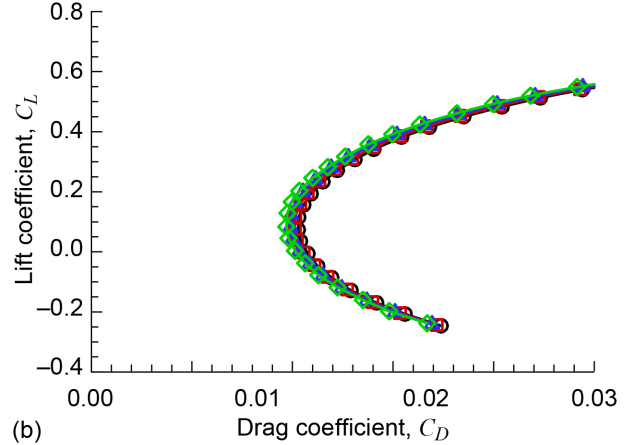


(b)

Figure 35.—Effect of Mach number of clean CRM65 wing performance at  $Re = 6.8 \times 10^6$ . Data from F1 wind tunnel with 13.3-percent-scale model. (a) Lift and pitching moment coefficients plotted versus angle of attack. (b) Lift coefficient plotted versus drag coefficient.



(a)



(b)

Figure 36.—Effect of Reynolds number on CRM65 wing performance with 3D high-fidelity maximum scallop artificial ice shape at  $M = 0.18$ . Data from F1 wind tunnel with 13.3-percent-scale model. (a) Lift and pitching moment coefficients plotted versus angle of attack. (b) Lift coefficient plotted versus drag coefficient.

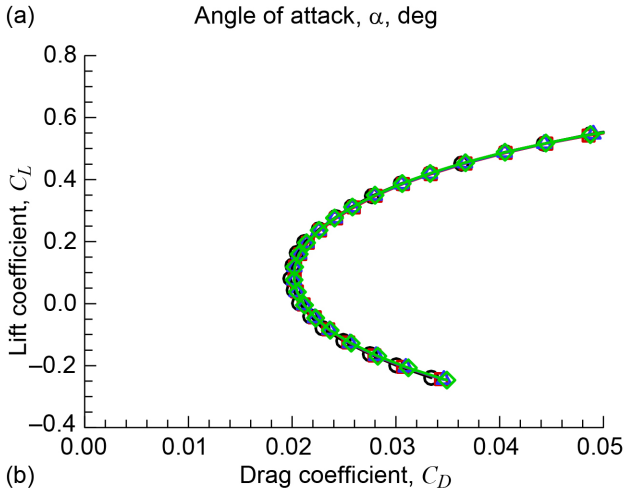
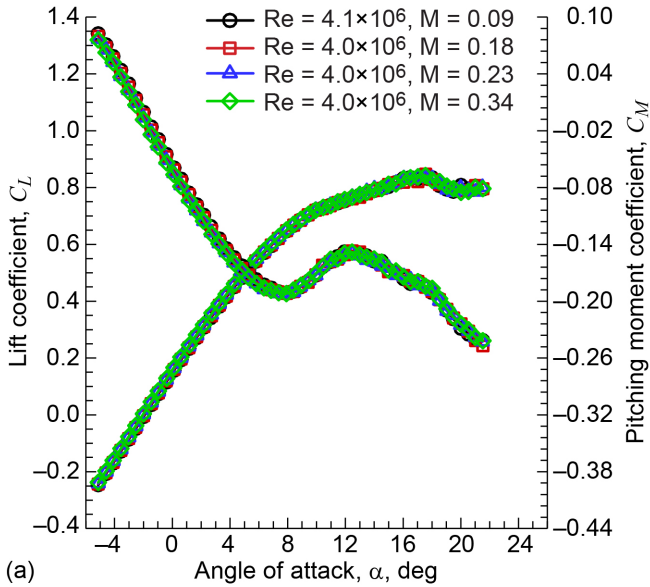


Figure 37.—Effect of Mach number on CRM65 wing performance with 3D high-fidelity maximum scallop artificial ice shape at  $Re = 4.0 \times 10^6$ . Data from F1 wind tunnel with 13.3-percent-scale model. (a) Lift and pitching moment coefficients plotted versus angle of attack. (b) Lift coefficient plotted versus drag coefficient.

with the maximum scallop high-fidelity ice shape. Here very little effect of Reynolds and Mach number is seen except for a small effect on  $C_D$  with Reynolds number. These trends of significant Reynolds and Mach number effects on the clean model and very little Reynolds and Mach number effects on the iced model are consistent with many 2D iced-airfoil studies.

The effect of Reynolds and Mach number on the CRM65 is documented using the four performance-based parameters and shown in Figure 38 and Figure 39. These figures show performance data from the clean model and from the model with three fidelities of the maximum scallop ice shape. The data for various Mach number are shown with identical colors and

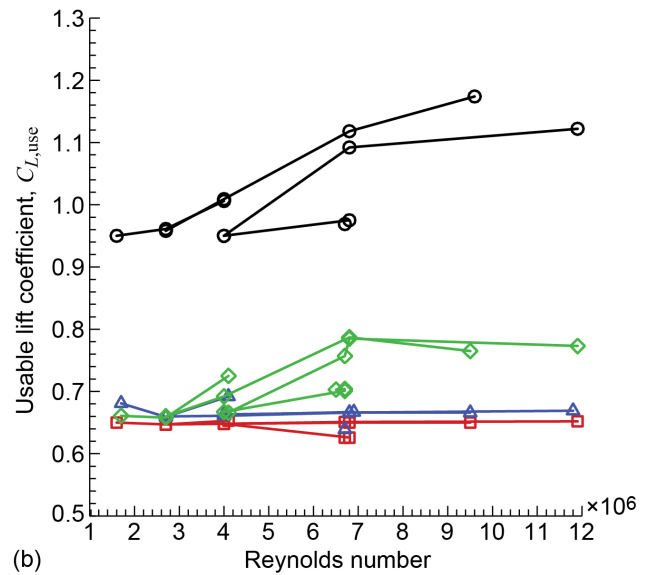
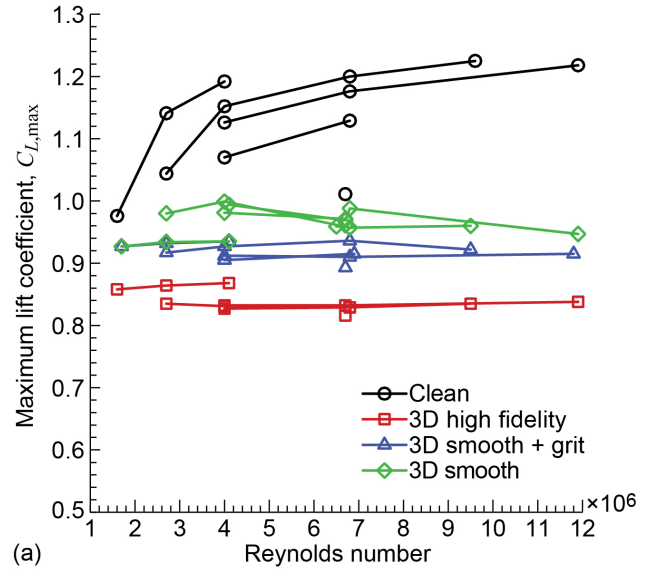


Figure 38.—Effect of Reynolds number on maximum and usable lift coefficients ( $C_{L,max}$  and  $C_{L,use}$ ) for clean and iced wing with maximum scallop artificial ice shapes having various levels of geometric fidelity at  $M = 0.09$  to  $0.34$ . Data from F1 wind tunnel with 13.3-percent-scale model. (a) Effect on  $C_{L,max}$ . (b) Effect on  $C_{L,use}$ .

symbols. Table IV of this report and Reference 82 contain more detailed information about the Mach number trends in these plots. Results for the clean-wing configuration show a strong dependence of  $C_{L,max}$  and  $C_{L,use}$  on both Reynolds number and Mach number (Figure 38). Because of this dependence, it is difficult to extrapolate the clean-wing lift performance to flight Reynolds and Mach numbers for airplane holding conditions. Almost no effect of Mach number was observed for  $C_{D,min}$  and  $C_{D,0.6}$  (Figure 39). The Reynolds number effects on the drag parameters were fairly weak, especially at higher Reynolds

number, and may allow for extrapolation to flight Reynolds number for holding conditions. The clean-wing configuration results also show that both Reynolds number and Mach number must be respected when making comparisons with smaller scale model wind tunnel tests at the lower range of Reynolds and Mach number.

Results for the iced-wing configurations with the 3D high-fidelity artificial ice shape exhibited consistent Reynolds and Mach number trends, as also shown in Figure 38 and Figure 39. The lift-based parameters  $C_{L,max}$  and  $C_{L,use}$  showed little to no dependence upon Reynolds number and Mach number greater than 0.18. These results agree with the past research on iced airfoils. It should be noted for completeness, however, that the typical Reynolds numbers for a CRM65-size airplane are significantly higher. As discussed in Section 2.3.1, the icing scenarios were based upon flaps-up holding operations. Wiberg et al. (Ref. 65) provide a summary of the corresponding Reynolds and Mach numbers that range from  $24.8 \times 10^6$  to  $32.9 \times 10^6$  and 0.35 to 0.46, respectively. Therefore, the maximum Reynolds number for the present data was at least a factor of 2 lower than the flight reference conditions. At the maximum Mach number of 0.34, Reynolds number was nearly a factor of 4 lower than the flight reference conditions. However, the maximum Mach number of 0.34 was significantly closer to the flight reference conditions. The observed lack of Reynolds and Mach number dependence in the present data suggests that the present results may be extrapolated to flight in holding conditions. Furthermore, testing conducted with artificial ice shapes on smaller scale models at the lower range of Reynolds and Mach number can yield very meaningful results with the caveat that possible Mach number effects should be considered for  $M < 0.18$ . In terms of drag-based parameters, there was no Mach number effect, and only small Reynolds number effects where both  $C_{D,min}$  and  $C_{D,0.6}$  decreased slightly with increased Reynolds number.

The effect of ice-shape fidelity was also investigated, and the 3D smooth and 3D smooth + grit configurations are also shown in Figure 38 and Figure 39. The 3D smooth, lower fidelity ice shape did not contain any ice roughness features. These roughness features were simulated on the 3D smooth + grit ice shape, where 46-grit-size silicon carbide grains were added to the baseline 3D smooth ice shape. In general, the Reynolds and Mach number trends in both lift and drag coefficients for the wing with the lower fidelity artificial ice-shape configurations were consistent with the results for the wing with the high-fidelity artificial ice shapes. Under some conditions, the wing performance with the 3D smooth configurations did exhibit more Reynolds number dependence than was observed when grit was added and for the high-fidelity artificial ice shapes. This can be seen in Figure 38 and Figure 39, where all the lift and drag parameters are relatively independent of Reynolds number for

the 3D smooth + grit case but more Re-dependent in the 3D smooth configuration. Neither configuration shows much Mach number dependence. This suggests that the addition of grit roughness to smooth shapes is important for both extrapolation of data to higher Reynolds number and comparison with smaller scale model tests.

Also evident from Figure 38 and Figure 39 is the effect of ice-shape fidelity. The data show that the wing with the 3D high-fidelity ice shape resulted in the most conservative performance degradations—the lowest values of  $C_{L,max}$  and  $C_{L,use}$  and the highest

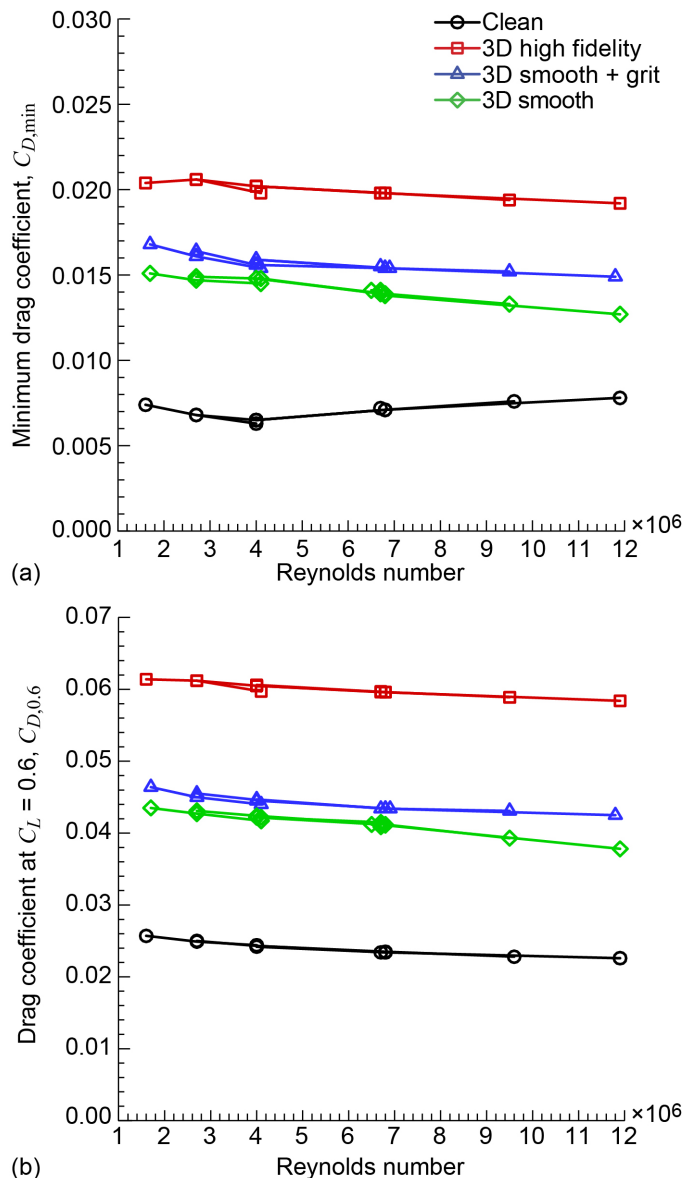


Figure 39.—Effect of Reynolds number on minimum and  $C_L = 0.6$  drag coefficients ( $C_{D,min}$  and  $C_{D,0.6}$ ) for clean and iced wing with maximum scallop artificial ice shapes having various levels of geometric fidelity at  $M = 0.09$  to 0.34. Data from F1 wind tunnel with 13.3-percent-scale model. (a) Effect on  $C_{D,min}$ . (b) Effect on  $C_{D,0.6}$ .

values of  $C_{D,min}$  and  $C_{D,0.6}$ . The effect of grit added to the 3D smooth configuration was fairly small for all of the parameters with the exception of  $C_{L,usc}$  at  $Re > 6.0 \times 10^6$ . The effects of ice-shape fidelity on the wing aerodynamic performance are summarized in Section 3.3.3.

In summary, these tests have demonstrated that while Reynolds and Mach number effects are important for quantifying the clean-wing performance, there is very little to no effect for the iced-wing performance with 3D, high-fidelity artificial ice shapes or 3D smooth ice shapes with grit roughness. These conclusions are consistent with the large volume of past research on iced airfoils, although some differences were noted for the associated stalling angle of the iced swept wing and for various lower fidelity versions of the leading-edge ice accretion.

### 3.2.3 Key Flow-Field Features—Type I and Type II Flows

It is well known that swept wings without leading-edge devices, as tested here with the CRM65, develop a leading-edge separation spanwise vortex at higher angle of attack (Ref. 114). From earlier research at low Reynolds number (e.g., Bragg, Kerho, and Khodadoust (Ref. 23); Kwon and Sankar (Ref. 24); Khodadoust and Bragg (Ref. 25); Diebold, Monastero, and Bragg (Ref. 48); and Diebold (Ref. 49)), it is also known that horn ice shapes that promote separation will generate leading-edge vortices at lower angles of attack. This is the dominant flow feature found for the CRM65 wing with ice shapes over the Reynolds number range tested.

The effect of fidelity was significant for the maximum scallop ice shapes, as the highly 3D scallop features influenced the development of the dominant leading-edge vortex flow. The initial testing of the maximum scallop ice shape was performed with two fidelities: the high-fidelity shape based on the scanned ice accretion and the 3D smooth shape developed from the method described in Section 2.4.6. The high-fidelity scallop shape has quasi-periodic protuberances (scallops) on the leading edge across the span that provide alternating vane-like structures separated by regions of reduced ice thickness (gaps), as shown in Figure 18. The 3D smooth shape (also shown in Figure 18) removes these 3D features as the cross sections are lofted to create the 3D smooth geometry. Later testing also included lower fidelity shapes consisting of discontinuous shapes and simple geometry horns (Ref. 99). The majority of the testing was on horn shapes that represented various degrees of fidelity of scallop ice accretions.

Based on these data, there appear to be two key flow-field features that result from highly 3D and nominally 3D horn-ice-shape geometry. The two flow-field features result from differences in the formation and development of the leading-edge vortex that dominates these flow fields at moderate to high angle of attack. These two flow-field types are referred to here as “Type I” and “Type II.” More detailed analyses of Type I and Type II

flows are given in Broeren et al. (Ref. 97), Lee et al. (Ref. 94), and Woodard and Bragg (Ref. 99).

Type I flow fields are dominated by spanwise-running leading-edge vortices generated by flow separation from the leading-edge ice accretion. Similar flow fields are well known and can occur on clean swept wings as documented by Poll (Ref. 114) and others. A Type I flow field is roughly the 3D extension of the separation bubble widely studied in the horn ice airfoil case (Bragg et al. (Refs. 4 and 5)). It may be one single vortex from root to tip or, more often, multiple leading-edge vortices as a result of the spanwise-varying leading-edge ice-accretion geometry and its interaction with the highly 3D swept-wing flow field. The Type I flow field was common for low-fidelity ice shapes that did not have complex 3D features such as scallops. The fully developed Type II flow field lacks the leading-edge spanwise vortex seen for the more uniform spanwise 3D horns. In the surface oil flow visualization, this flow field was observed to exhibit multiple streamwise-running streaks of oil that often appeared to emanate from the spanwise gaps in the scallop geometry. These features dominate the flow field through the usable-lift coefficient and angle-of-attack range, suppressing the leading-edge vortices for all or significant spanwise portions of the wing. Initially these streaks were referred to as “jets” (Refs. 115 and 116), but subsequent research efforts (Refs. 36, 94, 97, and 99), including Yoshida’s fundamental study of a swept backward-facing step (Ref. 117), showed these features are related to streamwise vorticity.

Figure 40 shows surface oil flow visualization for cases demonstrating Type I and Type II flow fields. Figure 40(a) illustrates the flow field over the wing upper surface with a simple 3D horn ice shape for  $\alpha = 4.3^\circ$ ; the inset provides a closeup of the wing region indicated. The dashed line indicates the leading-edge vortex reattachment line running parallel to the leading edge, clearly indicating the presence of the vortex. Well upstream of the dashed reattachment line, the oil is seen to pool, indicating the secondary separation line as the vortex induces flow upstream that again separates from the wing surface before reaching the leading edge. Figure 40(b) shows the medium gap discontinuous shape, which is a lower fidelity representation of the maximum scallop ice shape. Here the streamwise streaks are seen from the root to the tip and are shown more clearly in the inset to the right of the full upper-surface visualization. No evidence of a leading-edge vortex is seen in the medium gap discontinuous ice-shape configuration visualization as it appears to be suppressed by the flow field, represented by the streamwise streaks.

The Type I leading-edge vortex is the manifestation of a leading-edge separation that should be observable in the wing surface pressure distributions. Figure 41 shows the surface pressure distribution at  $\alpha = 6.4^\circ$  for the six streamwise-running pressure rows on the swept wing with the maximum scallop high-fidelity, 3D smooth, and 3D smooth plus grit ice shapes.

As expected, the resulting surface pressures reflect the impact of the flow separation and vortex through the constant pressure plateaus seen on the surface under the vortex. (Vortex reattachment actually occurs downstream of the pressure plateau as the pressure recovers to a level close to the unseparated value.) For each of the four pressure rows of normalized spanwise location  $y/b = 0.28, 0.44, 0.60,$  and  $0.81$ , the pressure plateau is readily seen in the leading-edge upper-surface distributions in Figure 41. For the high-fidelity case that exhibits a Type II flow field, a pressure spike is seen at the leading edge of all the pressure distributions shown. This indicates that the Type II flow field suppresses or delays the leading-edge separation and vortex, and the flow does not experience large-scale separation as it flows around these leading-edge ice shapes. Thus, the Type I and Type II flow fields represent fundamentally different flow fields, even though in this case they are generated by different fidelities of the same ice accretion.

The aerodynamic performance of the maximum scallop high-fidelity and 3D smooth shapes is shown in Figure 42. As expected, the aerodynamic performance is affected by the flow-field differences between Type I and Type II. The Type I flow field of the lower fidelity 3D smooth shapes has a higher, nonconservative maximum lift and a lower, nonconservative drag. This is especially notable because lower fidelity representations of the ice shapes are very desirable, but these differences in performance are large enough to be of concern for some applications. Thus, the performance differences between Type I and Type II flow fields from this and many other results are significant enough to warrant careful consideration as ice shapes are simulated and concerns of “How good is good enough?” are weighed.

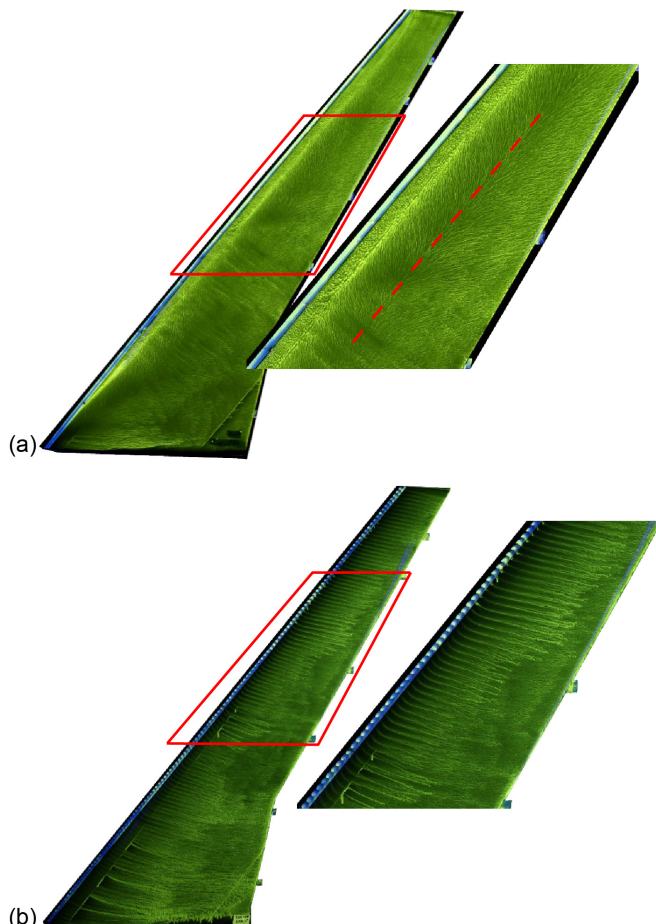


Figure 40.—Surface oil flow visualization images of swept-wing upper surface at  $\alpha = 4.3^\circ$ ; from WSU wind tunnel on 8.9-percent-scale model. (a) Simple 3D horn ice, Type I flow field. (b) 3D discontinuous ice shape, Type II flow field.

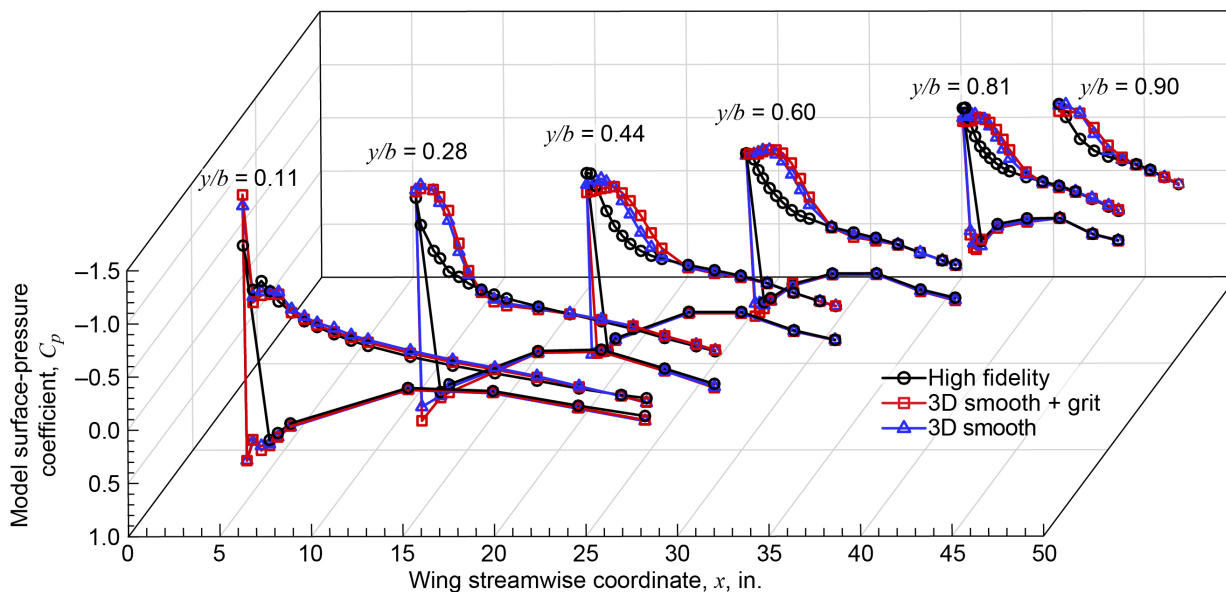


Figure 41.—Comparison of surface pressure coefficient for various fidelities of maximum scallop ice shape on swept wing at  $\alpha = 6.4^\circ$ . Data from WSU wind tunnel on 8.9-percent-scale model at  $Re = 1.6 \times 10^6$  and  $M = 0.18$ .

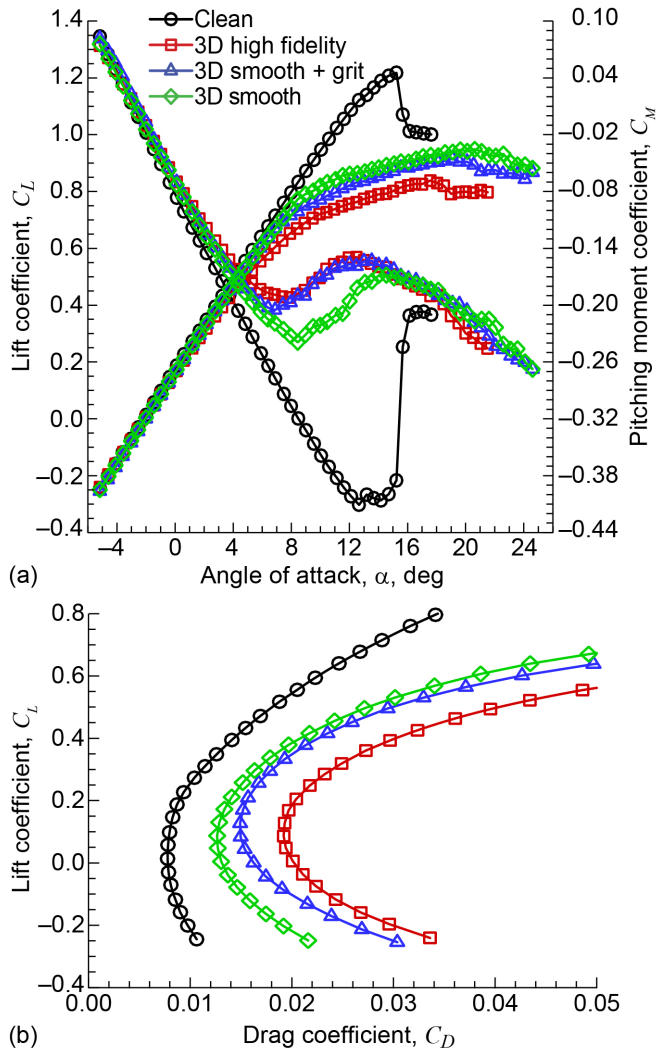


Figure 42.—Aerodynamic performance comparison, various fidelity representations of maximum scallop ice shape. Data from ONERA F1 wind tunnel on 13.3-percent-scale model at  $Re = 11.9 \times 10^6$ ,  $M = 0.23$ . (a) Lift and pitching moment coefficients plotted versus angle of attack. (b) Lift coefficient plotted versus drag coefficient.

This research was not designed to gather detailed flow-field data; much more research would be needed to fully understand Type I and Type II flows. Detailed flow-field studies of ice airfoils conducted over many years led to a complete understanding of the aerodynamic details. Further studies of iced swept wings are needed to develop a similar level of understanding in order to simulate ice shapes more accurately. Several observations from this effort deserve further research and could potentially lend some insight into the flow field:

- Streaks appear to be the result of streamwise vorticity—co-rotating and sometimes counter-rotating pairs.
- The streaks usually correspond to the large changes in spanwise geometry, such as scallop horns or simple geometry

discontinuities. This suggests a vortex-generator-type flow generation of the vorticity.

- In some cases, there are fewer streaks than features and the density of streaks changes with angle of attack. This suggests a shear-layer instability formation of counterrotating streamwise vortices, as was seen in iced airfoil flow fields.
- At higher angle of attack, both streaks and evidence of a leading-edge vortex behind the ice shape are sometimes seen in the flow visualization; thus, Type I and Type II flow fields are not mutually exclusive.
- Surface roughness attached to low-fidelity shapes can in some cases result in Type II flow fields.

### 3.2.4 Differences From 2D Iced Airfoil Aerodynamics

This research effort illuminated many differences from the well-established 2D airfoil ice-accretion and aerodynamic testing methods as well as differences in the ice accretions themselves and the resulting aerodynamic effect. The geometric complexity and scale of the CRM65 wing required previously undocumented ice-accretion testing methods. Swept hybrid models were developed using 3D CFD design methods. The resulting ice accretion for the three spanwise stations required the development of new morphing techniques to produce the 3D full semispan ice shapes. None of these techniques were required for the 2D airfoil case. The most important differences from 2D were in the complexity of the iced-wing flow fields.

The highly swept, twisted, and tapered CRM65 wing produced a complex 3D flow field even without leading-edge ice. The clean model leading-edge separation, spanwise vortex, and extensive spanwise flow on the surface have no parallel in 2D flows. This complex flow field drives the stalling process and is highly Reynolds number and Mach number dependent. With the 3D ice shapes, the fidelity and three-dimensionality of the ice shape have significant effect on the flow field and can support or suppress the leading-edge separation vortex and alter the overall aerodynamic performance. This led to the identification of Type I and Type II flow fields and expansion of the horn classification to include 3D horns and highly 3D horns (see Sec. 3.3). The complex 3D stalling process had a large and important effect on the wing pitching moment. This led to identifying the nose-up break in the pitching moment as a key parameter in evaluating the aerodynamic effect of ice shapes on the wing. The usable lift and usable angle of attack are set by this process. In 2D, iced airfoils almost always have an early stall and thus lower stall angle of attack. This was not true for iced swept wings, which often have a higher stall or maximum-lift angle of attack. For the simple and 3D smooth swept-wing ice shapes tested, Reynolds number effects were reduced with surface roughness. In general, these shapes on the swept wing were not as effective as the equivalent 2D airfoil ice shapes in reproducing the high-fidelity ice aerodynamics.

### 3.3 Ice-Shape Classification and Effect of Fidelity on Swept-Wing Performance

Aerospace professionals usually think of ice shapes in terms of the accretion process, assigning labels such as rime ice, glaze ice, or mixed accretions. These labels are extremely useful when the objective is to understand or document the ice accretion on an aircraft. However, aircraft performance and safety in icing conditions depends primarily on the aerodynamics of the iced surfaces (lift, drag, moments, etc.), and these depend on the flow-field physics. It is thus useful to classify ice shapes into a small set of shapes based on real ice-accretion geometries, taking into account their effect on the flow-field physics that govern the aerodynamics. This smaller set of simplified shapes can be varied parametrically, allowing for better understanding of iced-surface aerodynamics. Understanding these sensitivities can help engineers design ice simulations of reduced geometric fidelity and complexity that mimic the actual ice or a high-fidelity simulation.

In this section, the swept-wing ice-shape classification system developed in this research is briefly described. A much more detailed discussion is provided by Bragg et al. (Ref. 36), where airfoil ice-shape classification is presented as background and the swept-wing ice-shape classifications are developed. Following the description of the classification system, the effect of ice-shape fidelity on swept-wing aerodynamics is presented in the context of this classification.

#### 3.3.1 Swept-Wing Ice-Shape Classification

The initial effort to classify swept-wing ice shapes was presented by Broeren, Diebold, and Bragg (Ref. 34) in 2013. It relied heavily on the airfoil classification system that was developed after extensive systematic and fundamental experimental studies. The initial swept-wing classification system made use of only limited data on iced swept-wing aerodynamics and fundamental flow physics that existed before this project began. Thus, it followed the airfoil classification

system, and four classifications were proposed for swept wings: roughness, streamwise ice, horn ice, and spanwise-ridge ice.

Using the 2013 swept-wing ice-shape classification, the scalloped ice shapes tested in this study would be classified as horn shapes regardless of fidelity. However, as seen in the surface oil flow visualization and as described by the surface pressures, the flow fields are different depending on the level of three-dimensionality in the ice shapes—that is, whether the ice shape supports the formation of the leading-edge vortex (Type I) or suppresses it (Type II). Consistent with the philosophy of grouping ice shapes in consideration of the flow physics, these two different flow fields should be grouped into two different ice-shape classifications. The horn classification thus became two classifications:

1. 3D leading-edge horn
2. Highly 3D leading-edge horn

Only a small number of shapes have been tested, and the study of the flow-field physics is also limited, so the understanding of the characteristics of these two classifications is far from complete. The 3D leading-edge horn-ice shape classification is characterized by the horn size, location, and angle, as in the 2D airfoil case. The variation and rate of change of this horn in the spanwise direction is small with respect to the size of the horn. For the highly 3D leading-edge horn, however, characterization is more difficult and uncertain. The location and size of the horn in a spanwise averaged sense is expected to be important to the flow field and aerodynamics of the wing, but the rapid changes in the horn or ice shape in the spanwise direction are more difficult to characterize. In studying the high-fidelity maximum scallop shape from this research program, Woodard et al. (Refs. 98 and 99) developed some basic parameters to develop lower fidelity, 3D discontinuous representations of this shape. These parameters are given in Table X along with key parameters for the other proposed swept-wing ice-shape classifications.

TABLE X.—PROPOSED SWEEP-WING ICE-SHAPE CLASSIFICATION

Classification	Key parameters
Roughness	Roughness height, location, and density
Streamwise ice	Shape thickness, roughness height, and density
3D leading-edge horn ice	Horn height, location, angle, and roughness
Highly 3D leading-edge horn ice	Spanwise averaged horn height, location, angle, spanwise variation of horn geometry, and roughness
Spanwise-ridge ice	Location and height

Tests of the one streamwise ice shape in this research program produced a Type II flow field for the high-fidelity shape and a Type I flow field for the 3D smooth low-fidelity version of this shape (Bragg et al. (Ref. 36) and Camello et al. (Refs. 84 and 93)). The argument could be made to remove streamwise ice from the classification system and include this streamwise shape, and potentially all streamwise shapes, into the two new categories of horn shapes. Clearly, many streamwise shapes have a geometry that can be viewed as a horn shape on the leading edge, oriented at a low angle roughly into the incoming relative wind. It was concluded that one case was not enough to make this change, however. The flow-field physics on additional examples of this shape may later suggest other classification solutions. For example, airfoil streamwise shapes have been tested that were very conformal to the leading edge, increasing camber and effectively acting as a leading-edge device. A future streamwise shape on a swept wing may also demonstrate these physics, so the streamwise classification has been retained for now. Similarly, no spanwise-ridge shapes were tested as part of this project, but this classification was retained because it is thought to be important, with flow physics that are potentially different from the other classifications.

### 3.3.2 Ice-Shape Fidelity Effects on Aerodynamics

In discussing ice-shape fidelity, aircraft icing researchers and engineers will often pose the question, “How good is good enough?” What is usually meant by this is how accurately the ice-shape geometry must be predicted by a computer code, or simulated for a wind tunnel or flight test, to generate sufficiently accurate aerodynamics for design or certification uses.

“How good is good enough?” first requires an answer to the question, “Good enough for what purpose?” The level of ice-shape fidelity required for a specific research purpose may be quite different than that required for an aircraft certification action or aircraft design analysis. Instead of trying to answer the question, “How good is good enough?”, this research effort addressed a related question: “What is the effect of the level of fidelity on the aerodynamic simulation of swept-wing icing?” Ice-shape fidelity data were used to examine the impact of fidelity level on the aerodynamic performance of the CRM65 swept wing. It was hoped that this analysis, focused on a specific use of iced aerodynamics, could be useful in future efforts toward determining “How good is good enough?”

This section provides an overall summary of the findings from all ice shapes tested in this research program before focusing discussion on the WB33, maximum scallop, and streamwise configurations. The findings from all of the ice shapes tested can be summarized as follows:

- For the horn ice shapes (which includes the scalloped shapes), aerodynamic results on the lower fidelity 3D smooth shapes based on the outermost surface geometry always generated nonconservative performance degradation as compared with the high-fidelity ice shapes.
- This result also applies to the 3D smooth horn shapes with added roughness.
- For the horn ice shapes (which includes the scalloped shapes), none of the lower fidelity versions reproduced the drag accurately. Typical differences were in the range of 20 to 40 percent lower than the high-fidelity configuration. Drag may not be a primary concern for these large ice shapes, but in situations where drag is a concern, the highly 3D ice features cannot be neglected.
- The opposite trend in drag was observed for the streamwise ice shape where the 3D smooth results were conservative.
- For all configurations, the addition of roughness to 3D smooth shapes and simple 3D horn shapes was required to minimize Reynolds and Mach number effects.
- The 3D ice features of the high-fidelity horn ice configurations are important to the iced-wing flow field and resulting integrated performance.
- Currently, only an initial understanding of the role of the 3D ice features in the flow-field development and corresponding aerodynamic performance is available.
- This results in a limited ability to identify the important ice-shape geometric parameters that must be quantified and reproduced in lower fidelity horn ice shapes.

With the exception of one streamwise ice accretion, the high-fidelity ice shapes and their low-fidelity simulations tested in this research program were all horn shapes. Two of these horn ice shapes, the WB33 configuration and the maximum scallop, are discussed here in more detail (Secs. 3.3.2.1 and 3.3.2.2, respectively) because multiple levels of fidelity, LEWICE3D shapes, and simple horn shapes were tested. The streamwise shape is also discussed in detail (Sec. 3.3.2.3). A brief summary of the effects of fidelity on the aerodynamics is provided for each shape, and a table with quantitative values of the primary comparison parameters is also provided.

#### 3.3.2.1 WB33 Configuration

The WB33 ice shape was investigated for numerous lower fidelity configurations in addition to the high-fidelity shape. These lower fidelity configurations included 3D smooth shapes based upon LEWICE3D simulations and several simple 3D horn configurations. Table XI, Table XII, and Table XIII provide a summary of the effect of these various fidelities upon the lift- and drag-based performance parameters. Findings of these tests include the following:

- The 3D smooth and LEWICE3D geometries with grit roughness reproduced  $C_{L,max}$  and  $C_{L,use}$  of the high-fidelity geometry to within about 5 percent.
- The 3D smooth and LEWICE3D geometries with grit roughness reproduced  $\alpha_{stall}$  and  $\alpha_{use}$  degradation to within 3°.
- This agreement is attributed to the dominance of the Type I flow field, which can be represented by 3D leading-edge horn shapes with added grit roughness.
- The 3D smooth and LEWICE3D geometries with and without grit roughness resulted in values of the drag parameters that were 22 to 40 percent lower than for the 3D high-fidelity configuration.
- Simple 3D horn geometries with grit roughness also represented the basic aerodynamics and could be used to conduct more parametric studies to understand the tradeoffs associated with horn height, angle, and location.

TABLE XI.—SUMMARY OF LIFT PERFORMANCE PARAMETERS FOR WING WITH ICE SHAPES BASED ON WB33 ICING CONDITIONS AT  $Re = 11.9 \times 10^6$ ,  $M = 0.23$

Ice-shape fidelity	$C_{L,max}$			$C_{L,use}$		
	$C_{L,max}$	$\Delta C_{L,max}^a$	Percent $\Delta C_{L,max}^b$	$C_{L,use}$	$\Delta C_{L,use}^a$	Percent $\Delta C_{L,use}^b$
Clean	1.218	-----	-----	1.122	-----	-----
3D high fidelity	0.860	-----	-----	0.650	-----	-----
3D smooth	0.937	0.077	9.00	0.705	0.055	8.5
3D smooth + grit	0.906	0.046	5.30	0.670	0.020	3.1
LEWICE3D + grit	0.904	0.044	5.10	0.638	-0.012	-1.8
Simple horn, $k/c = 0.0355$ , $\theta = 10^\circ$	0.898	0.038	4.40	0.640	-0.010	-1.5
Simple horn, $k/c = 0.0355$ , $\theta = 10^\circ + \text{grit}$	0.898	0.039	4.50	0.633	-0.017	-2.6
Simple horn, $k/c = 0.0355$ , $\theta = 40^\circ + \text{grit}$	0.830	-0.030	-3.50	0.521	-0.129	-20.0
Simple horn, $k/c = 0.0177$ , $\theta = 40^\circ + \text{grit}$	0.865	0.005	0.58	0.581	-0.069	11.0

<sup>a</sup> $\Delta C_L$  = low fidelity – high fidelity.

<sup>b</sup>Percent  $\Delta C_L$  = (low fidelity – high fidelity)/high fidelity.

TABLE XII.—SUMMARY OF ANGLE-OF-ATTACK PERFORMANCE PARAMETERS FOR WING WITH ICE SHAPES BASED ON WB33 ICING CONDITIONS AT  $Re = 11.9 \times 10^6$ ,  $M = 0.23$

Ice-shape fidelity	$\alpha_{stall}$		$\alpha_{use}$	
	$\alpha_{stall}$	$\Delta \alpha_{stall}^a$	$\alpha_{use}$	$\Delta \alpha_{use}^a$
Clean	15.2°	-----	12.7°	-----
3D high fidelity	17.0°	-----	7.4°	-----
3D smooth	20.6°	3.6°	7.5°	0.1°
3D smooth + grit	18.6°	1.6°	6.9°	-0.5°
LEWICE3D + grit	19.6°	2.6°	6.4°	-1.0°
Simple horn, $k/c = 0.0355$ , $\theta = 10^\circ$	19.1°	2.1	6.4°	-1.0°
Simple horn, $k/c = 0.0355$ , $\theta = 10^\circ + \text{grit}$	18.0°	1.0°	6.3°	-1.1°
Simple horn, $k/c = 0.0355$ , $\theta = 40^\circ + \text{grit}$	16.5°	-0.5°	4.8°	-2.6°
Simple horn, $k/c = 0.0177$ , $\theta = 40^\circ + \text{grit}$	18.1°	1.1°	5.8°	-1.6°

<sup>a</sup> $\Delta \alpha$  = low fidelity – high fidelity.

TABLE XIII.—SUMMARY OF DRAG PERFORMANCE PARAMETERS  
FOR WING WITH ICE SHAPES BASED ON WB33  
ICING CONDITIONS AT  $Re = 11.9 \times 10^6$ ,  $M = 0.23$

Ice-shape fidelity	$C_{D,min}$			$C_{D,0.6}$		
	$C_{D,min}$	$\Delta C_{D,min}^a$	Percent $\Delta C_{D,min}^b$	$C_{D,0.6}$	$\Delta C_{D,0.6}^a$	Percent $\Delta C_{D,0.6}^b$
Clean	0.0078	-----	-----	0.0226	-----	-----
3D high fidelity	0.0205	-----	-----	0.0585	-----	-----
3D smooth	0.0134	-0.0071	-35	0.0424	-0.0161	-28
3D smooth + grit	0.0153	-0.0052	-25	0.0457	-0.0128	-22
LEWICE3D + grit	0.0124	-0.0081	-40	0.0441	-0.0144	-25
Simple horn, $k/c = 0.0355$ , $\theta = 10^\circ$	0.0090	-0.0115	-56	0.0420	-0.0165	-28
Simple horn, $k/c = 0.0355$ , $\theta = 10^\circ +$ grit	0.0099	-0.0106	-52	0.0483	-0.0102	-17
Simple horn, $k/c = 0.0355$ , $\theta = 40^\circ +$ grit	0.0115	-0.0090	-44	0.1041	0.0456	78
Simple horn, $k/c = 0.0177$ , $\theta = 40^\circ +$ grit	0.0097	-0.0108	-53	0.0734	0.0149	26

<sup>a</sup> $\Delta C_D$  = low fidelity – high fidelity.

<sup>b</sup>Percent  $\Delta C_D$  = (low fidelity – high fidelity)/high fidelity.

### 3.3.2.2 Maximum Scallop Configuration

The maximum scallop configuration was tested in the high-fidelity shape and the lower fidelity 3D smooth shape. LEWICE3D and several discontinuous horn configurations were tested based on the maximum scallop icing conditions and 3D smooth shape, respectively. Table XIV, Table XV, and Table XVI provide a summary of the effect of these various fidelities upon the lift- and drag-based performance parameters. In general, the 3D smooth configurations were unable to reproduce the Type II flow-field features, thus resulting in poorer agreement in the performance-based parameters. As noted earlier in this section, the addition of roughness did result in some limited observation of the Type II features, but the Type I flow field was consistently more dominant. For the 3D discontinuous configurations, the flow field was consistently Type II at angles of attack lower than  $\alpha_{use}$ , which may account for the fairly uniform values of this parameter. However, for angles of attack higher than  $\alpha_{use}$ , the flow field was not defined and could not be classified as either Type I or Type II (Ref. 99). Findings of these tests are included here for the roughness sensitivity study, LEWICE3D-based artificial ice shapes, and 3D discontinuous shapes.

Roughness sensitivity study:

- Hemisphere roughness and grit roughness with the same height resulted in similar aerodynamic impact.
- Variations in grit size had a more significant impact on drag than on lift.

- These results suggest that the precise size and shape of roughness applied to 3D smooth shapes is not critical to reproducing the aerodynamics of the high-fidelity configuration.
- The 3D smooth configuration with each roughness configuration reproduced  $C_{L,max}$  to within about 10 percent or less of the high-fidelity configuration and reproduced  $C_{L,use}$  to within about 4 percent or less of the high-fidelity configuration.
- The 3D smooth configuration with each roughness configuration reproduced  $\alpha_{stall}$  to within  $1.5^\circ$  beyond the high-fidelity configuration and reproduced  $\alpha_{use}$  to within  $1^\circ$  earlier than the high-fidelity configuration.

LEWICE3D-based artificial ice shapes:

- The two versions of the LEWICE3D ice shapes (one based upon the BC LEWICE3D IFB and one based upon UW LEWICE3D IRT in Figure 25) had different horn thicknesses and angles, but similarities in the values of the performance-based parameters when grit roughness was applied.
- Both BC LEWICE3D IFB and UW LEWICE3D IRT (with grit) configurations reproduced  $C_{L,max}$  to within about 14 percent of the high-fidelity configuration and reproduced  $C_{L,use}$  to within about 22 percent or less of the high-fidelity configuration.
- Both BC LEWICE3D IFB and UW LEWICE3D IRT (with grit) configurations reproduced  $\alpha_{stall}$  to within  $3.5^\circ$  or less

beyond the high-fidelity configuration and reproduced  $\alpha_{use}$  to  $0.5^\circ$  or less beyond the high-fidelity configuration.

3D discontinuous ice shapes:

- The lift-based parameters for nearly all configurations compared better with the high-fidelity configuration than did those of the 3D smooth ice shape from which they were designed.
- Three of the five 3D discontinuous configurations resulted in conservative  $C_{L,max}$  degradations that ranged from 0.5 to 7.0 percent lower than for the high-fidelity configuration.
- Four of the five 3D discontinuous configurations resulted in conservative  $C_{L,use}$  degradations that ranged from 3.5 to 15.5 percent lower than for the high-fidelity configuration.
- Despite these variations in  $C_{L,max}$  and  $C_{L,use}$ , the corresponding values of  $\alpha_{stall}$  and  $\alpha_{use}$  were all within  $1.6^\circ$  or less of the high-fidelity values.

### 3.3.2.3 Streamwise Ice Configuration

For this configuration, the high-fidelity shape and the lower fidelity 3D smooth shape with and without grit roughness were tested. Table XVII, Table XVIII, and Table XIX provide a

summary of the effect of these various fidelities upon the lift- and drag-based performance parameters. Findings of these tests include the following:

- The 3D smooth configuration with grit resulted in conservative  $C_{L,max}$  degradation that was 5.1 percent lower than for the high-fidelity configuration.
- The 3D smooth configuration with grit resulted in nonconservative  $C_{L,use}$  degradation that was 13 percent higher than for the high-fidelity configuration.
- The results in angle-of-attack parameters for the 3D smooth configuration with grit were consistent with the above-listed  $C_{L,max}$  and  $C_{L,use}$  trends where  $\alpha_{stall}$  was  $4.1^\circ$  lower and  $\alpha_{use}$  was  $2.5^\circ$  higher than for the high-fidelity configuration.
- The high-fidelity configuration exhibited a combination of Type I and Type II flow-field features for angles of attack less than  $\alpha_{use}$  but became Type I dominant for angles of attack greater than  $\alpha_{use}$ .
  - The 3D smooth configuration with grit resulted in conservative  $C_{D,min}$  and  $C_{D,0.6}$  degradation that was about 9 to 10 percent higher than for the high-fidelity configuration.

TABLE XIV.—SUMMARY OF LIFT PERFORMANCE PARAMETERS FOR WING WITH ICE SHAPES BASED ON MAXIMUM SCALLOP ICING CONDITIONS AT  $Re = 11.9 \times 10^6$ ,  $M = 0.23$

Ice-shape fidelity	$C_{L,max}$			$C_{L,use}$		
	$C_{L,max}$	$\Delta C_{L,max}^a$	Percent $\Delta C_{L,max}^b$	$C_{L,use}$	$\Delta C_{L,use}$	Percent $\Delta C_{L,use}^b$
Clean	1.218	-----	-----	1.122	-----	-----
3D high fidelity	0.838	-----	-----	0.652	-----	-----
3D smooth	0.947	0.109	13.0	0.773	0.120	19.0
3D smooth + 20 grit	0.907	0.069	8.2	0.668	0.016	2.5
3D smooth + 46 grit	0.915	0.077	9.2	0.669	0.017	2.6
3D smooth + 80 grit	0.924	0.086	10.3	0.678	0.026	4.0
3D smooth + hemispheres	0.924	0.086	10.3	0.677	0.025	3.8
3D smooth BC LEWICE3D IFB	0.977	0.139	16.6	0.823	0.171	26.2
3D smooth BC LEWICE3D IFB + 46 grit	0.959	0.121	14.4	0.757	0.105	16.1
3D smooth UW LEWICE3D IRT + 46 grit	0.955	0.117	14.0	0.794	0.142	21.8
Small gap 3D discontinuous	0.834	-0.004	-0.5	0.629	-0.023	-3.5
Medium gap 3D discontinuous	0.821	-0.017	-2.0	0.551	-0.101	-15.5
Normal to leading edge medium gap 3D discontinuous	0.854	0.016	1.9	0.618	-0.034	-5.2
Streamwise medium gap 3D discontinuous	0.843	0.005	0.6	0.653	0.001	0.2
Curved streamwise medium gap 3D discontinuous	0.779	-0.059	-7.0	0.573	-0.079	-12.1

<sup>a</sup> $\Delta C_L$  = low fidelity – high fidelity.

<sup>b</sup>Percent  $\Delta C_L$  = (low fidelity – high fidelity)/high fidelity.

TABLE XV.—SUMMARY OF ANGLE-OF-ATTACK PERFORMANCE  
PARAMETERS FOR WING WITH ICE SHAPES BASED ON  
MAXIMUM SCALLOP ICING CONDITIONS AT  $Re = 11.9 \times 10^6$ ,  $M = 0.23$

Ice-shape fidelity	$\alpha_{stall}$		$\alpha_{use}$	
	$\alpha_{stall}$	$\Delta\alpha_{stall}^a$	$\alpha_{use}$	$\Delta\alpha_{use}^a$
Clean	15.2°	-----	12.7°	-----
3D high fidelity	17.6°	-----	7.9°	-----
3D smooth	19.6°	2.0°	8.4°	0.5°
3D smooth + 20 grit	18.6°	1.0°	6.9°	-1.0°
3D smooth + 46 grit	19.1°	1.5°	6.9°	-1.0°
3D smooth + 80 grit	19.1°	1.5°	6.9°	-1.0°
3D smooth + hemispheres	19.1°	1.5°	6.9°	-1.0°
3D smooth LEWICE3D IFB	19.1°	1.5°	8.9°	1.0°
3D smooth LEWICE3D IFB + 46 grit	19.6°	2.0°	7.9°	0.0°
3D smooth LEWICE3D IRT + 46 grit	21.1°	3.5°	8.5°	0.5°
Small gap 3D discontinuous	18.6°	0.9°	7.9°	0.0°
Medium gap 3D discontinuous	17.5°	-0.1°	6.3°	-1.6°
Normal to leading edge medium gap 3D discontinuous	17.6°	0.0°	7.8°	-0.1°
Streamwise medium gap 3D discontinuous	17.5°	-0.1°	7.4°	-0.5°
Curved streamwise medium gap 3D discontinuous	18.0°	0.4°	7.8°	-0.1°

<sup>a</sup> $\Delta\alpha$  = low fidelity – high fidelity.

TABLE XVI.—SUMMARY OF DRAG PERFORMANCE PARAMETERS FOR WING WITH  
ICE SHAPES BASED ON MAXIMUM SCALLOP ICING CONDITIONS AT  $Re = 11.9 \times 10^6$ ,  $M = 0.23$

Ice-shape fidelity	$C_{D,min}$			$C_{D,0.6}$		
	$C_{D,min}$	$\Delta C_{D,min}^a$	Percent $\Delta C_{D,min}^b$	$C_{D,0.6}$	$\Delta C_{D,0.6}^a$	Percent $\Delta C_{D,0.6}^b$
Clean	0.0078	-----	-----	0.0226	-----	-----
3D high fidelity	0.0192	-----	-----	0.0584	-----	-----
3D smooth	0.0127	-0.0065	-33.9	0.0378	-0.0206	-35.3
3D smooth + 20 grit	0.0168	-0.0024	-12.5	0.0454	-0.0130	-22.3
3D smooth + 46 grit	0.0149	-0.0043	-22.4	0.0425	-0.0159	-27.2
3D smooth + 80 grit	0.0142	-0.0050	-26.0	0.0412	-0.0172	-29.5
3D smooth + hemispheres	0.0147	-0.0045	-23.4	0.0414	-0.0170	-29.1
3D smooth LEWICE3D IFB	0.0107	-0.0085	-44.3	0.0300	-0.0284	-48.6
3D smooth LEWICE3D IFB + 46 grit	0.0123	-0.0069	-35.9	0.0313	-0.0271	-46.4
3D smooth LEWICE3D IRT + 46 grit	0.0124	-0.0068	-35.4	0.0280	-0.0304	-52.1
Small gap 3D discontinuous	0.0151	-0.0041	-21.4	0.0693	0.0109	18.7
Medium gap 3D discontinuous	0.0136	-0.0056	-29.2	0.0786	0.0202	34.6
Normal to leading edge medium gap 3D discontinuous	0.0211	0.0019	9.9	0.0587	0.0003	0.5
Streamwise medium gap 3D discontinuous	0.0132	-0.0060	-31.3	0.0415	-0.0169	-28.9
Curved streamwise medium gap 3D discontinuous	0.0164	-0.0028	-14.6	0.1033	0.0449	76.9

<sup>a</sup> $\Delta C_D$  = low fidelity – high fidelity.

<sup>b</sup>Percent  $\Delta C_D$  = (low fidelity – high fidelity)/high fidelity.

TABLE XVII.—SUMMARY OF LIFT PERFORMANCE PARAMETERS FOR WING WITH ICE SHAPES BASED ON STREAMWISE ICING CONDITIONS AT  $Re = 11.9 \times 10^6$ ,  $M = 0.23$

Ice-shape fidelity	$C_{L,max}$			$C_{L,use}$		
	$C_{L,max}$	$\Delta C_{L,max}^a$	Percent $\Delta C_{L,max}^b$	$C_{L,use}$	$\Delta C_{L,use}^a$	Percent $\Delta C_{L,use}^b$
Clean	1.218	-----	-----	1.122	-----	-----
3D high fidelity	0.957	-----	-----	0.777	-----	-----
3D smooth	1.058	0.101	10.6	0.861	0.083	10.7
3D smooth + grit	0.908	-0.049	-5.1	0.882	0.104	13.4

<sup>a</sup> $\Delta C_L$  = low fidelity – high fidelity.

<sup>b</sup>Percent  $\Delta C_L$  = (low fidelity – high fidelity)/high fidelity.

TABLE XVIII.—SUMMARY OF ANGLE-OF-ATTACK PERFORMANCE PARAMETERS FOR WING WITH ICE SHAPES BASED ON STREAMWISE ICING CONDITIONS AT  $Re = 11.9 \times 10^6$ ,  $M = 0.23$

Ice-shape fidelity	$\alpha_{stall}$		$\alpha_{use}$	
	$\alpha_{stall}$	$\Delta \alpha_{stall}^a$	$\alpha_{use}$	$\Delta \alpha_{use}^a$
Clean	15.2°	-----	12.7°	-----
3D high fidelity	17.6°	-----	8.5°	-----
3D smooth	18.7°	1.1°	9.5°	1.0°
3D smooth + grit	13.5°	-4.1°	11.0°	2.5°

<sup>a</sup> $\Delta \alpha$  = low fidelity – high fidelity.

TABLE XIX.—SUMMARY OF DRAG PERFORMANCE PARAMETERS FOR WING WITH ICE SHAPES BASED ON STREAMWISE ICING CONDITIONS AT  $Re = 11.9 \times 10^6$ ,  $M = 0.23$

Ice-shape fidelity	$C_{D,min}$			$C_{D,0.6}$		
	$C_{D,min}$	$\Delta C_{D,min}^a$	Percent $\Delta C_{D,min}^b$	$C_{D,0.6}$	$\Delta C_{D,0.6}^a$	Percent $\Delta C_{D,0.6}^b$
Clean	0.0078	-----	-----	0.0226	-----	-----
3D high fidelity	0.0098	-----	-----	0.0264	-----	-----
3D smooth	0.0087	-0.0011	-10.5	0.0241	-0.0023	-8.6
3D smooth + grit	0.0106	0.0008	8.8	0.0289	0.0026	9.7

<sup>a</sup> $\Delta C_D$  = low fidelity – high fidelity.

<sup>b</sup>Percent  $\Delta C_D$  = (low fidelity – high fidelity)/high fidelity.

### 3.3.3 Recommendations for Research To Advance Understanding of Ice-Shape Fidelity Effects

It was beyond the scope of this study to perform detailed flow-field visualization and velocity measurements to develop a more complete understanding of the complex Type I and Type II flow fields. The detailed physics and relative importance of these different flow mechanisms are unknown at this time. The global effect of the Type II 3D flow features is to prevent and/or delay the formation of the leading-edge vortex. Because the leading-edge vortex is a dominant feature in these flows, this also alters the aerodynamic performance of the wing,

as seen in the summary data and the more detailed analyses in the references cited in Section 3.2.3.

This study attempted to produce simple 3D ice shapes with periodic variations in the spanwise geometry that would produce a flow field with these Type II 3D flow features and similar performance to the high-fidelity shapes. These attempts, described in Section 3.2.3 and detailed in the references cited therein, had some success. However, because the flow field is not well understood, it is not possible at this time to provide clear guidance in how to produce simple shapes that provide accurate and conservative aerodynamic performance for high-fidelity scallop ice shapes.

For applications requiring low-fidelity versions of various high-fidelity shapes and swept-wing geometries, a better understanding of the flow-field physics is needed. This would provide more confidence in the ability of properly designed low-fidelity shapes to produce aerodynamics sufficiently similar to the high-fidelity shapes to satisfy the question of “How good is good enough?” for many applications.

The current study did not address leading-edge roughness and spanwise-ridge ice-shape classifications. These two classifications of ice shapes need significantly more research and are not addressed in the comments to follow. For the two horn classifications and the streamwise shape, a more confident ability to assess fidelity effects requires a much better understanding of the iced swept-wing flow field of scalloped horn shapes. To accurately reproduce the aerodynamics of iced swept wings with low-fidelity shapes, these shapes must reproduce the main flow features that drive the aerodynamics. Therefore, a systematic study of the iced swept-wing flow field is needed that varies the geometry of shapes that generate both Type I and Type II flow fields. Of particular importance is understanding the flow field generated by the complex scallop geometry, the suppression of the leading-edge vortex in Type II flows, and how this transitions into mixed and Type I flows with increasing angle of attack. Some parametric variation of the swept-wing geometry is needed, as it is expected that parameters such as wing sweep and twist will have a major effect on the leading-edge vortex, a main flow feature. It is especially important to consider more detailed configurations, including flaps down. In the 2D airfoil case, detailed flow-field measurements using hot wires, split films, laser Doppler velocimetry, and particle image velocimetry provided an understanding of the flow and enabled researchers to compare and contrast with more fundamental flows (e.g., backward-facing steps) that other researchers had studied in detail. Study of the separating shear layer and time-dependent measurements helped in the understanding of the unsteady aerodynamics and the separation region reattachment that controlled maximum lift. Similar studies of swept-wing icing (but more complex due to the fully 3D nature of the flow) are needed to more fully understand swept-wing aerodynamics. Such studies will provide improved guidance on low-fidelity simulation and, more generally, support knowledge of “how good is good enough.”

### **3.4 Computational Aerodynamic Simulation of the Iced Swept Wing**

The use of 3D computational tools for both ice-accretion simulation and aerodynamic simulation is described in detail in Sections 2.3.1, 2.3.2, and 3.1.1 to 3.1.3. These simulations were

critical for the hybrid model design, ice-accretion testing, and posttest comparison of computational and experimental ice shapes. As noted in Section 2.5, an additional aspect of computational simulation was to determine the aerodynamic effect of the ice on the CRM65 swept wing. This aspect was significantly more challenging, and this research effort has made some significant contributions, but much more work needs to be done. The large database of experimental results described earlier in this section provides the required data to pursue advanced simulation of the iced swept-wing aerodynamics. This section summarizes the important aspects and findings of mesh deformation and IBC methods implemented at ONERA. Computational simulation research for the iced swept wing was also carried out at the University of Virginia using 3D RANS and hybrid RANS–LES (large-eddy simulation) approaches on more conventional unstructured meshes. Those results are also summarized herein.

#### **3.4.1 Application of Immersed Boundary Conditions to Iced Swept-Wing CFD Simulation**

The use of numerical tools has become much more common for prediction and analysis of aerodynamic performance and for certification of ice-shape configurations. However, different tools or methods are generally used for ice accretion and aerodynamic performance estimation, and there could be advantages if similar methods could be used for both. The main obstacle is not in the CFD software used but in the mesh generation of the complex, highly 3D ice shapes. For ice-accretion tools, it is advantageous to make an update of the airfoil shape during the accretion phase, and for aerodynamic performance evaluation, it is necessary to handle the very complex ice shapes considered on wings. This section describes two different approaches for computation of the aerodynamics of the iced swept wing.

The first option available for grid generation of the ice shape is direct remeshing. However, this requires an accurate description of the ice-shape surface (CAD geometry), and generally, the exact surface geometry is not available at each step of the accretion process. The second option is to use local information on nodes or cells where ice is created, either for a local surface displacement (mesh deformation) or for an “obstacle source term” (IBC method) to be applied to a reference grid of the “clean” shape. Both mesh deformation and the IBC method were evaluated on a common 3D ice-shape configuration tested in the high-Reynolds-number test campaign in the ONERA F1 wind tunnel. For the comparison exercise, the 3D smooth maximum scallop ice-shape configuration was considered, as a reference grid can be generated for it. A rendering of a section of the wing with this configuration is shown in Figure 43.

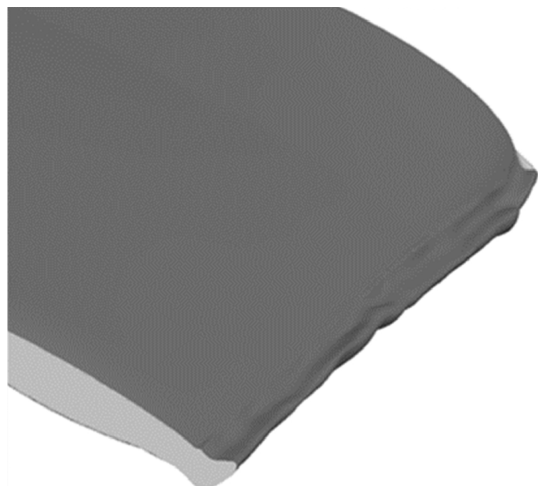


Figure 43.—CAD rendering of CRM65 wing section with 3D smooth maximum scallop ice-shape configuration.

### 3.4.2 3D RANS Simulations of 13.3-Percent-Scale Model of Clean Swept Wing

A reference grid based on the clean configuration was generated using ANSYS ICEM Hexa software. The grid integrates the different model elements (semispan wing and splitter plate) and the tunnel floor, as shown in Figure 44(a). The other tunnel walls (side walls and top) are not considered, as their influence on the measurements is very limited due to the low model blockage for the aerodynamic experiments. A specific domain delimitation where the ice shapes are present on the model has been used in the leading-edge area. Additionally, the grid has been densified in this region to increase the surface discretization for the mesh deformation method or the IBC method, as shown in Figure 44(b). The final grid is made up of about  $38.6 \times 10^6$  cells.

From the experimental test matrix, the flow conditions for the CFD were  $Re = 4.0 \times 10^6$  and  $M = 0.23$  (Table II). Results with forced boundary-layer transition (tripped) were considered. Computations were carried out in SI units (Système International d'Unités) (m, m/s, K, Pa, etc.). The main numerical settings used were as follows:

- elsA version: 4.1.02
- Jameson scheme with low 2nd- and 4th-order dissipation coefficients,  $K_2 = 0$  and  $K_4 = 1/64$ , respectively

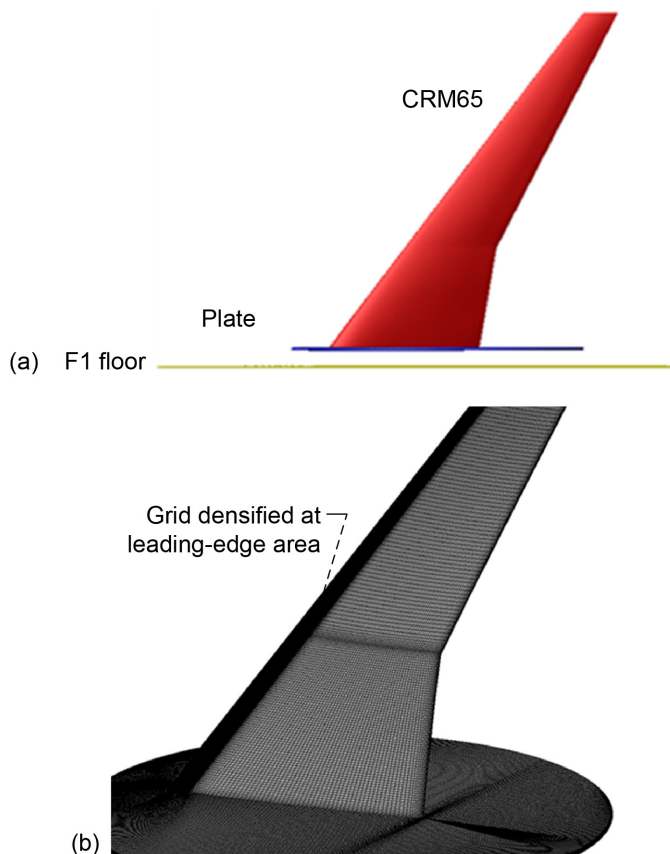


Figure 44.—CFD model geometry. (a) As installed in F1 wind tunnel. (b) Clean-wing reference grid.

- Backward Euler scheme with Courant–Friedrichs–Lewy (CFL) number from 1 to 100
- Fully turbulent computations with Spalart–Allmaras (SA) model with quadratic constitutive relation (QCR) correction
- Multigrid acceleration technique and low-speed preconditioning

A satisfactory correlation between the experimental and CFD results is observed in surface pressure over a large range of angles of attack, as shown in Figure 45 for  $\alpha = 2^\circ$  and in Figure 46 for  $\alpha = 10^\circ$ . Based on these results, the reference grid was determined to be suitable for the evaluation of the mesh deformation method or for IBC simulations.

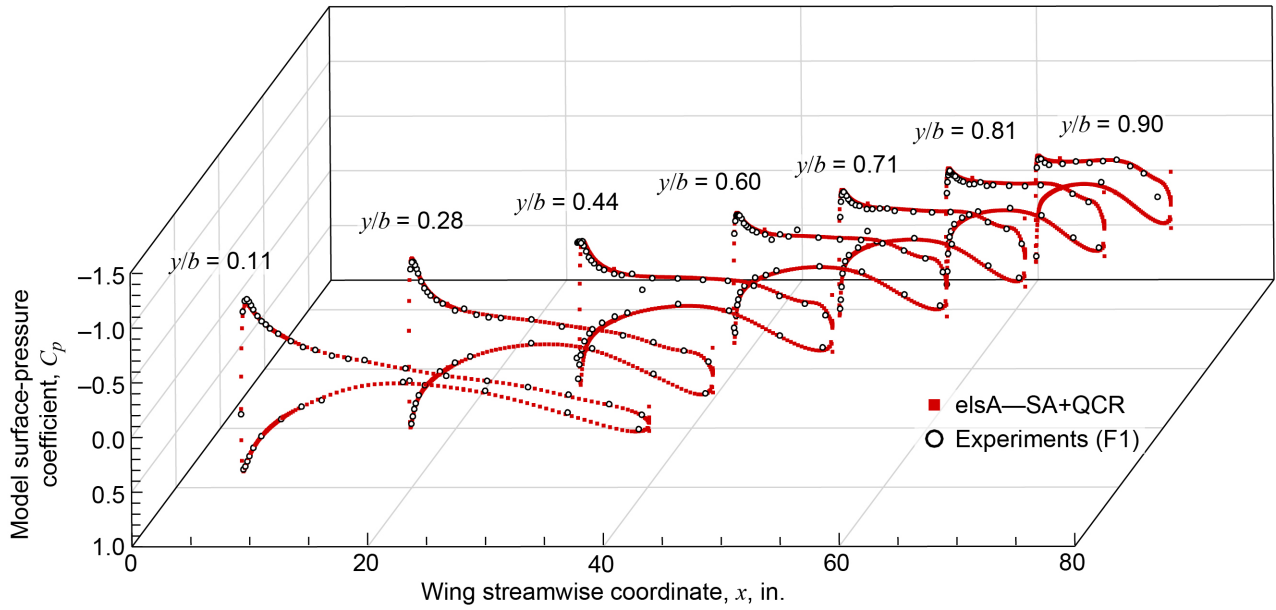


Figure 45.—Comparison of surface pressure coefficient CFD results with experimental data for clean-wing configuration at  $\alpha = 2^\circ$ ,  $Re = 4.0 \times 10^6$ , and  $M = 0.23$ . Experimental data from 13.3-percent-scale model in F1 wind tunnel.

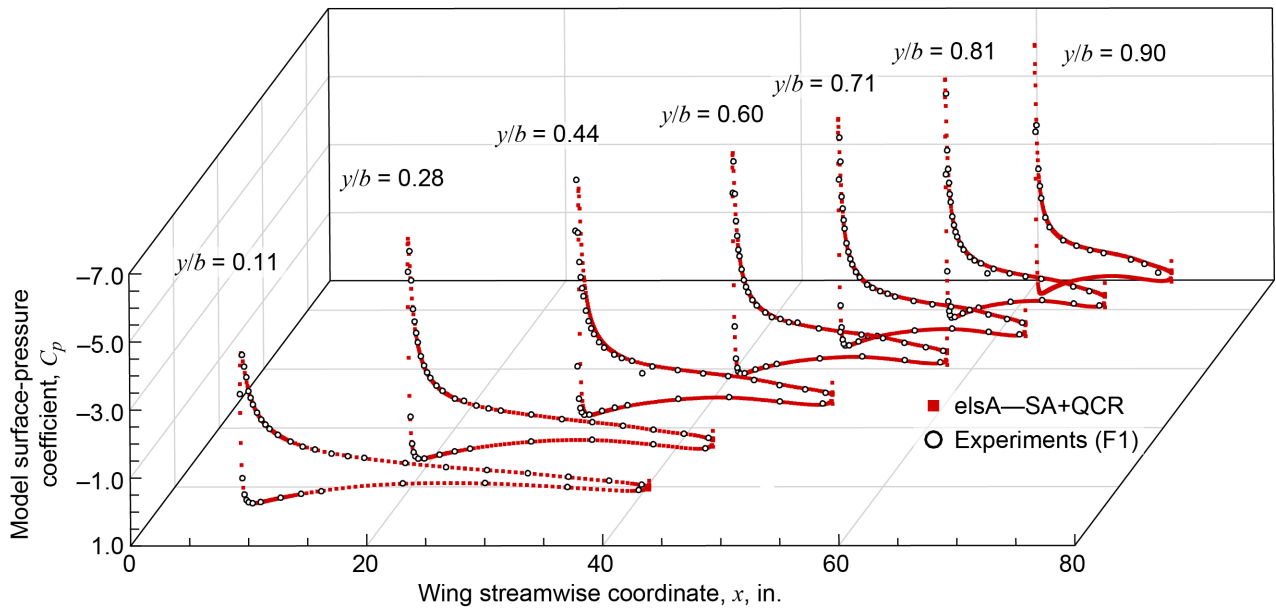


Figure 46.—Comparison of surface pressure coefficient CFD results with experimental data for clean-wing configuration at  $\alpha = 10^\circ$ ,  $Re = 4.0 \times 10^6$ , and  $M = 0.23$ . Experimental data from 13.3-percent-scale model in F1 wind tunnel.

### 3.4.3 3D RANS Simulations of 13.3-Percent-Scale Model of Iced Swept Wing Using Mesh Deformation Method

First, a grid was generated around the ice-shape geometry using Quantum, a mesh deformation tool developed by the Aerodynamics, Aeroelasticity, and Acoustics Department at ONERA. It was initially developed for aeroelasticity purposes and used in the framework of aerodynamic shape optimization (Refs. 110, 111, and 118). This tool can be applied to any kind of grid (structured, unstructured, or hybrid) and topology. It starts from an initial volume grid and the surface grid to be deformed. For each node of the surface grid, the displacement is decomposed in two vectors. The first vector takes into account the local rotation of the mesh; the second takes into account the translation. These two vectors are described by quaternions.

Next, the surface deformation field is propagated to the volume grid by an inverse distance approach accelerated by a fast multipole method. For the more complex deformation cases, the final solution can be regulated using subiterations of the deformation process. For the ice-shape configuration considered, five subiterations were used to handle the very complex shape to be obtained. Figure 47 presents the grid obtained at three wing sections. The initial grid is in green; the deformed grid is in black.

Finally, CFD computations were carried out using the same numerical settings as the reference clean-wing case for different angles of attack, and a satisfactory agreement was observed on the aerodynamic performance evaluation, as shown in Figure 48.

### 3.4.4 3D RANS Simulations of 13.3-Percent-Scale Model of Iced Swept Wing Using IBC

The use of IBC is quite natural for ice-accretion applications. Output from any accretion code will include location of the ice shape on the airfoil and its size. It is therefore simple to use this information on the reference grid to “flag” cells where ice is present and to reproduce a modified surface with a specific treatment. The ice geometry was defined using the surface grid generated from the mesh deformation technique described in Section 3.4.3. A postprocessor was then used to fit the ice geometry into the reference grid and detect the cells inside the ice shape or at its surface. Some source terms were then considered in the reference grid to account for the effect of the ice shape.

For the purpose of this study, the so-called “order 0” (or “no slip” condition) IBC implemented in the elsA software was considered. It takes into account turbulent properties of the flow and some velocity gradients near the wall through source terms, but with no wall functions.

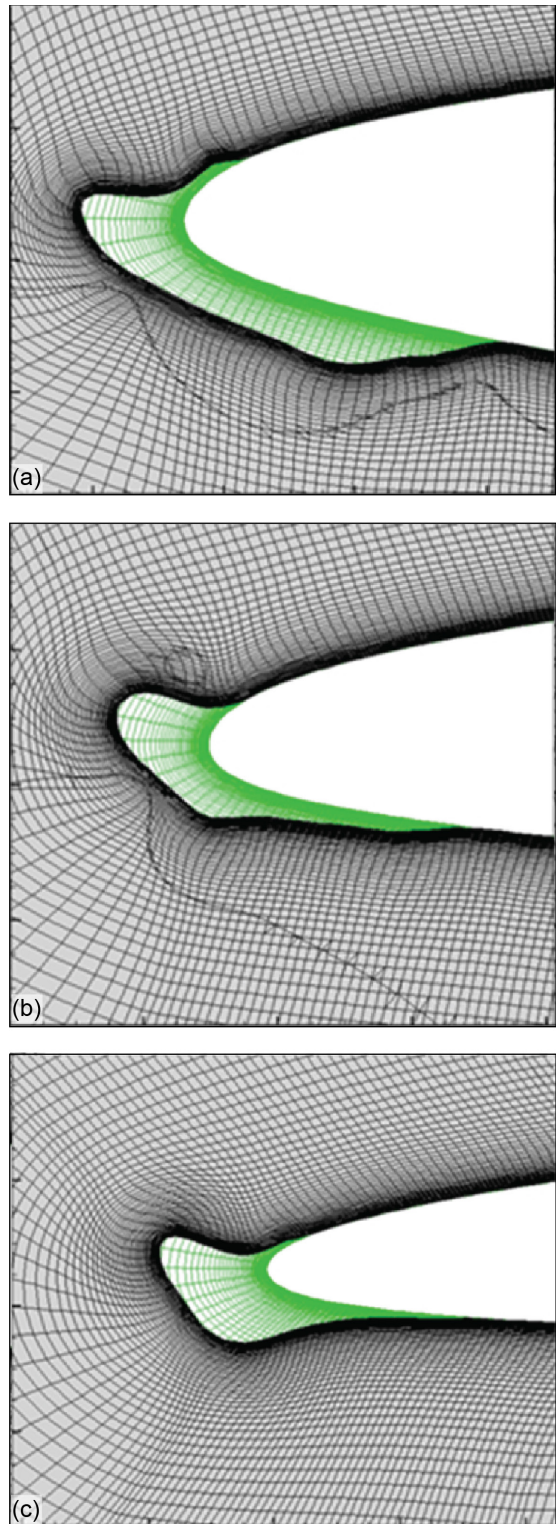


Figure 47.—Ice wing section cuts showing baseline grid obtained with Quantum deformation method. Initial grid shown in green; deformed grid shown in black. (a) Normalized spanwise location  $y/b = 0.28$ . (b)  $y/b = 0.52$ . (c)  $y/b = 0.87$ .

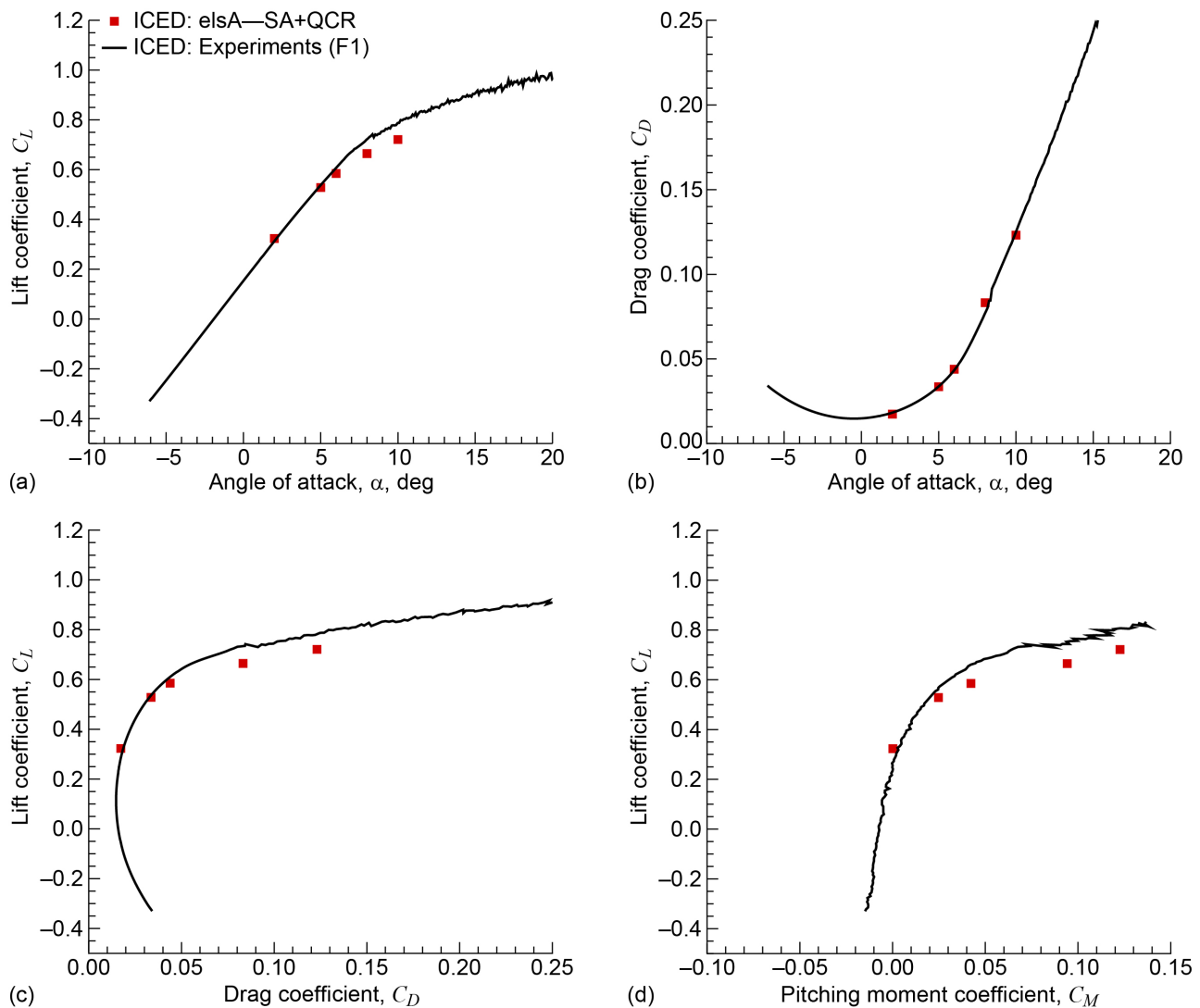


Figure 48.—Comparison of integrated aerodynamic CFD results with experimental data for the 3D smooth maximum scallop iced-wing configuration at  $Re = 4.0 \times 10^6$  and  $M = 0.23$ . Experimental data from 13.3-percent-scale model in F1 wind tunnel. (a)  $C_L$  versus  $\alpha$ . (b)  $C_D$  versus  $\alpha$ . (c)  $C_L$  versus  $C_D$ . (d)  $C_L$  versus  $C_M$ .

IBC computations considered the same values of numerical dissipation as for the reference. In terms of computational-wall-clock time and convergence characteristics, IBC calculations are similar to those carried out on the reference grid. However, multigrid computations considered only one coarse grid instead of two, mainly due to some unstable behavior observed at the beginning of the convergence for IBC.

The solutions obtained by both methods (Quantum grid with blue symbols, IBC solution with red symbols) are compared with experimental results (symbols) in Figure 49 to Figure 51. It is important to evaluate these results in the context of what is known about the flow field from Section 3.2.3. The 3D smooth maximum scallop ice shape exhibits a Type I flow where separation from the ice shape generates leading-edge vortices. In the pressure distributions (e.g., Figure 41), this leads to regions

of relatively constant pressure on the surface under the vortices. It is instructive to see which of these gridding schemes best reproduces this important flow physics feature.

First, for low angle of attack with no large separations present at the leading edge ( $\alpha = 2^\circ$ , Figure 49), both methods give similar results in terms of accuracy. However, results obtained with the Quantum grid seem slightly better than those from the IBC method. When leading-edge separation starts to be significant (Type I flow field), at  $\alpha = 5^\circ$  (Figure 50), the IBC results show much better agreement with experiments than do the Quantum grid results. For example, the IBC method at  $y/b = 81.1$  percent does an excellent job of predicting the pressure and length of the leading-edge separation zone. It can also be noted that with the Quantum grid, a high-pressure peak oscillation is computed in the attachment line region at leading edge, followed by a

low-pressure peak developed on the upper surface. This was not seen in the experimental data. When the wing is fully separated at  $\alpha = 8^\circ$  and  $10^\circ$  in Figure 51 and Figure 52, the IBC method again produces better results than the Quantum solutions, as it better predicts the leading-edge region flow-field pressures.

Thus, better agreement is observed on  $C_p$  distributions with the IBC method compared with the results obtained on the

Quantum grid, although there was no specific grid refinement done for the IBC method. Further validation work is needed, taking into account grid refinement studies and more complex ice-shape geometries, but the use of simple IBC methods applied on a standard reference clean-wing grid seems quite promising for a good estimation of the pressure field developed over a 3D wing with complex ice shapes.

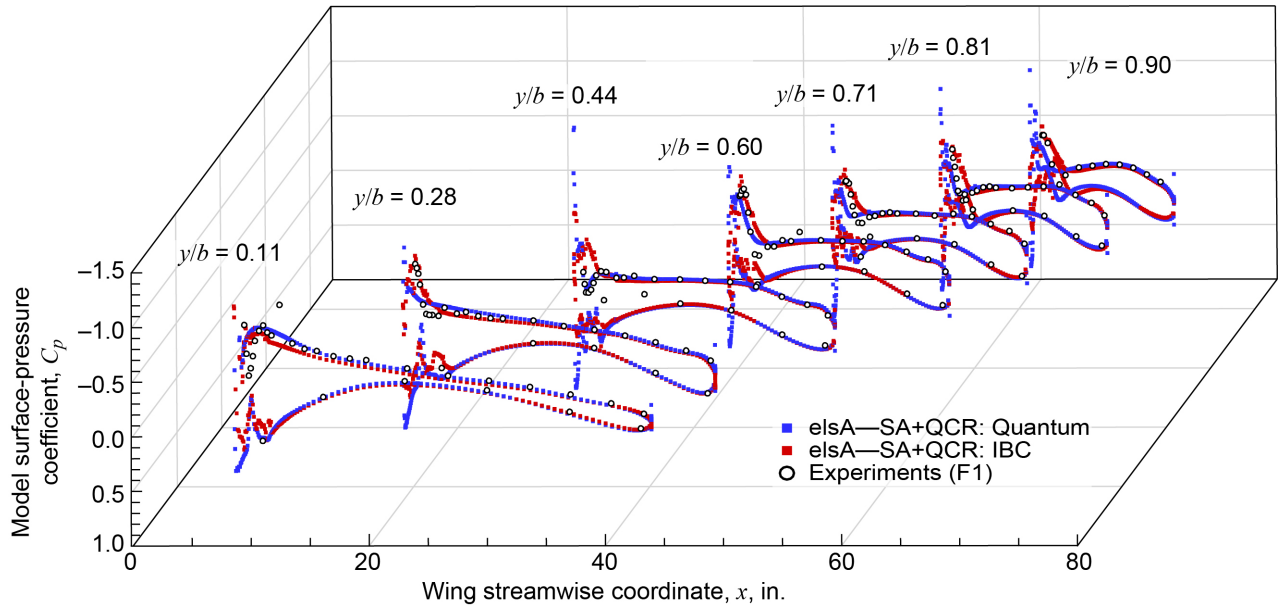


Figure 49.—Comparison of surface pressure coefficient CFD results with experimental data for 3D smooth maximum scallop iced-wing configuration at  $\alpha = 2^\circ$  and  $Re = 4.0 \times 10^6$  and  $M = 0.23$ . Experimental data from 13.3-percent-scale model in F1 wind tunnel.

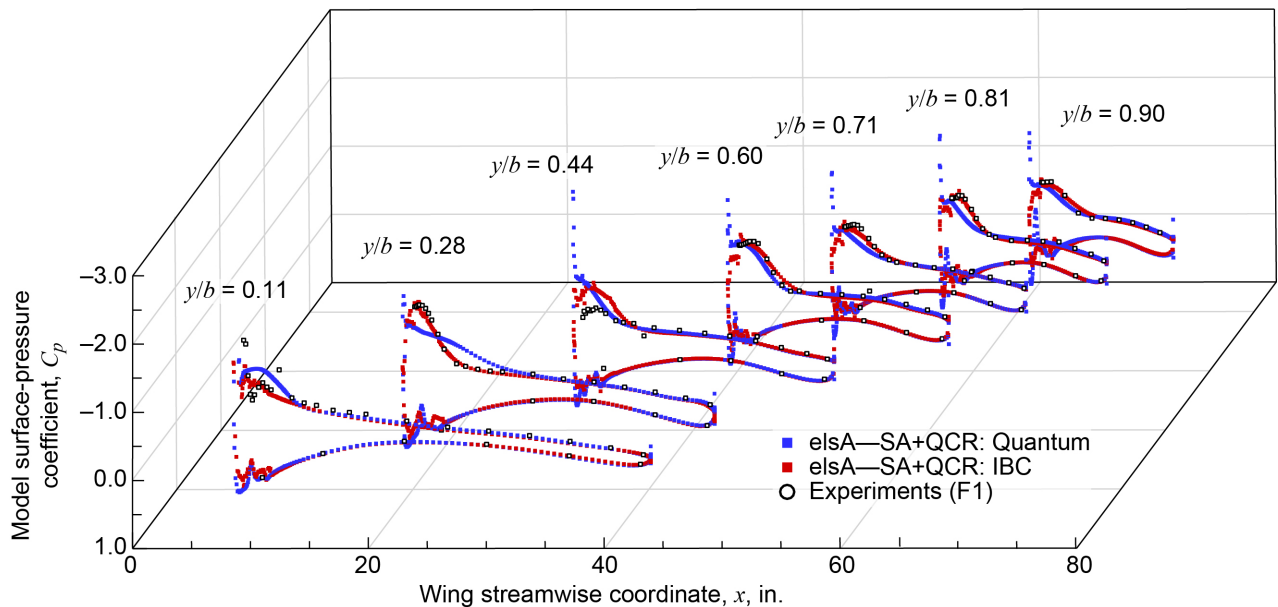


Figure 50.—Comparison of surface pressure coefficient CFD results with experimental data for 3D smooth maximum scallop iced-wing configuration at  $\alpha = 5^\circ$  and  $Re = 4.0 \times 10^6$  and  $M = 0.23$ .

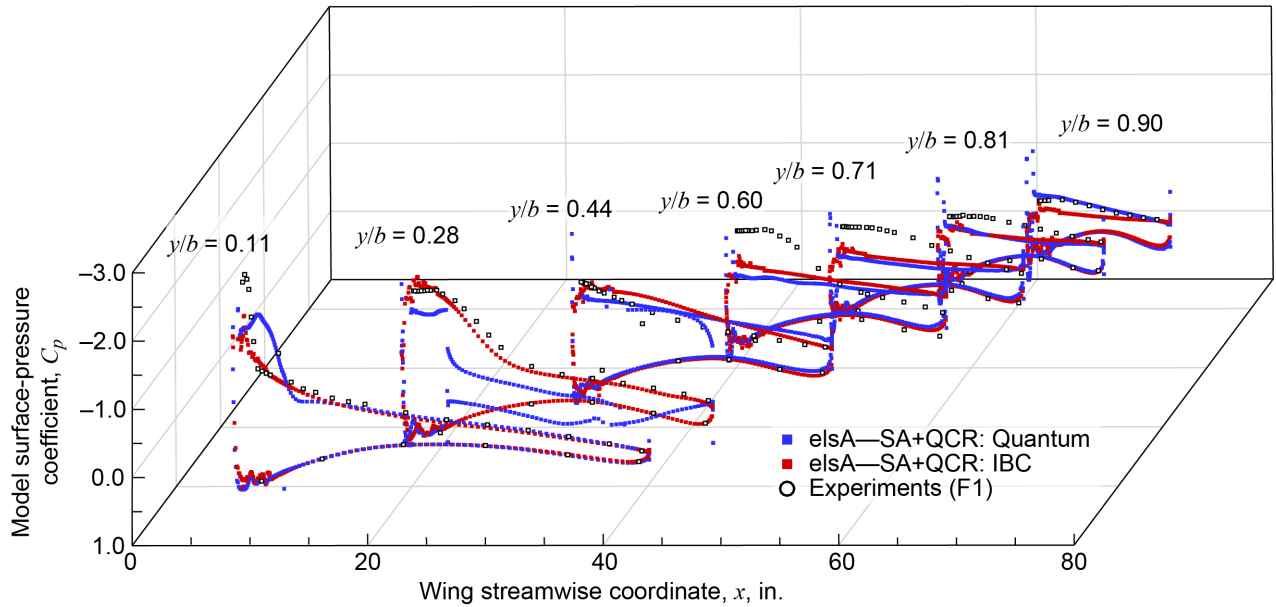


Figure 51.—Comparison of surface pressure coefficient CFD results with experimental data for 3D smooth maximum scallop iced-wing configuration at  $\alpha = 8^\circ$  and  $Re = 4.0 \times 10^6$  and  $M = 0.23$ . Experimental data from 13.3-percent-scale model in F1 wind tunnel.

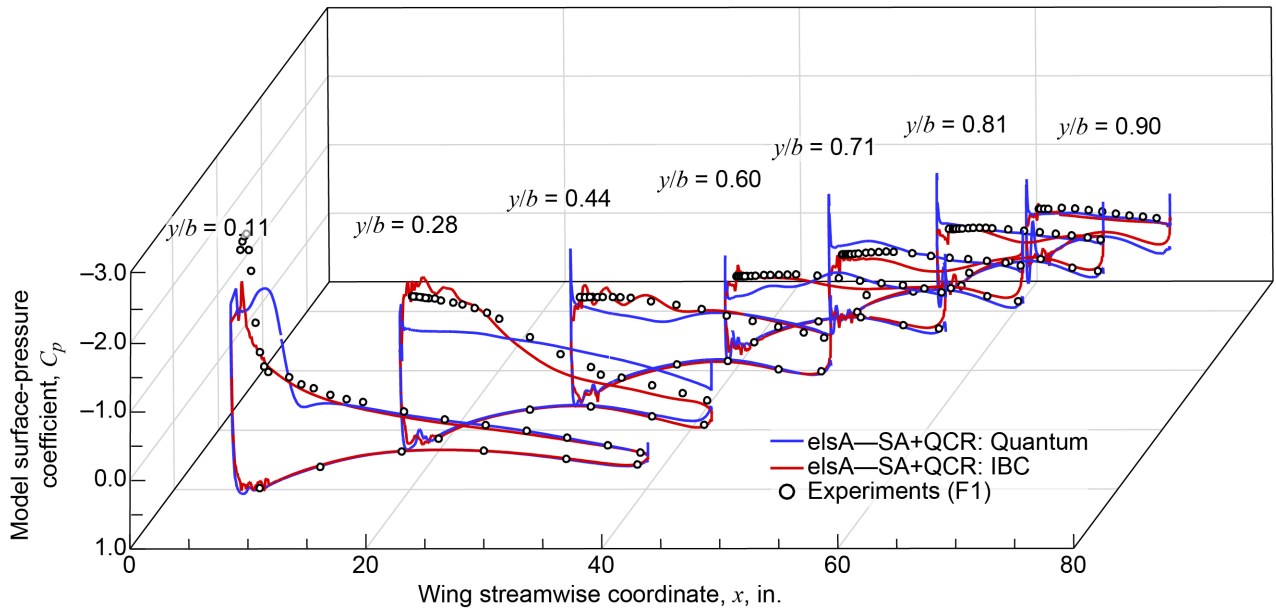


Figure 52.—Comparison of surface pressure coefficient CFD results with experimental data for 3D smooth maximum scallop iced-wing configuration at  $\alpha = 10^\circ$  and  $Re = 4.0 \times 10^6$  and  $M = 0.23$ . Experimental data from 13.3-percent-scale model in F1 wind tunnel.

### 3.4.5 3D RANS and IDDES Simulations of 8.9-Percent-Scale Model of Iced Swept Wing

Additional computational simulations were performed by Stebbins et al. (Refs. 104 and 105) using the same 3D smooth maximum scallop iced-wing configuration. While the iced-wing configuration was identical, the simulations were performed using the 8.9-percent-scale model geometry as installed in the WSU test section. These simulations included all four walls of the test section and were treated with viscous boundary conditions. Setting up the CFD simulation in this way allowed for direct comparison of the computational results with the experimental data without correction for any tunnel wall effects.

In the dissemination of their work, Stebbins et al. (Ref. 105) describe the numerical methodology utilized for carrying out the 3D RANS simulations with the commercially available ANSYS Fluent CFD code. The authors describe why they chose to use the shear stress transport (SST)  $k-\omega$  turbulence model and to develop unstructured boundary-layer meshes via Pointwise’s anisotropic tetrahedral extrusion (T-Rex) method. Special attention was given to the complex curvature areas associated with the leading-edge ice geometry. An initial grid height was selected to ensure a  $y^+$  value equal to one. Averaging over the angles of attack studied, the iced-wing domain was composed of  $28.1 \times 10^6$  nodes and  $70.2 \times 10^6$  cells. The number of iterations required to come to a converged solution was 120,000 at  $\alpha = 10^\circ$ .

In general, the results of the 3D RANS simulations showed good comparison with the experimental data. Stebbins et al.

(Ref. 105) provided comparisons of surface pressure and integrated performance data as well as to the surface oil flow visualization available from the WSU test campaigns. An example comparison of surface pressure is shown in Figure 53 for the wing with the 3D smooth maximum scallop configuration at  $\alpha = 10^\circ$ . At this angle of attack, the flow over the wing outboard of  $y/b = 0.28$  was highly separated. These comparisons show that the 3D RANS simulations were able to capture the separated flow correctly. The authors also show that the computational simulation was able to adequately predict the Type I flow-field characteristics that developed on the wing leading up to the usable-lift angle of attack. The effectiveness of the RANS simulations was somewhat surprising given the limited success of such simulation on 3D extruded versions of iced airfoils (cf. Stebbins et al. (Ref. 107)). However, it is unclear if the 3D RANS simulation would continue to perform well for angles of attack higher than  $10^\circ$  where there was significant flow separation on the iced wing. It is also important to note that Stebbins, Loth, and Qin (Ref. 104) had earlier attempted to use improved delayed detached-eddy simulation (IDDES)—a variation on the hybrid RANS and LES method—to analyze the same iced-wing configuration. These results showed that their implementation of IDDES did not accurately capture the Type I flow-field stalling characteristics. Because the study was preliminary in nature, it was not conclusive as to whether there was an inherent problem with the IDDES approach or an issue with their implementation of it.

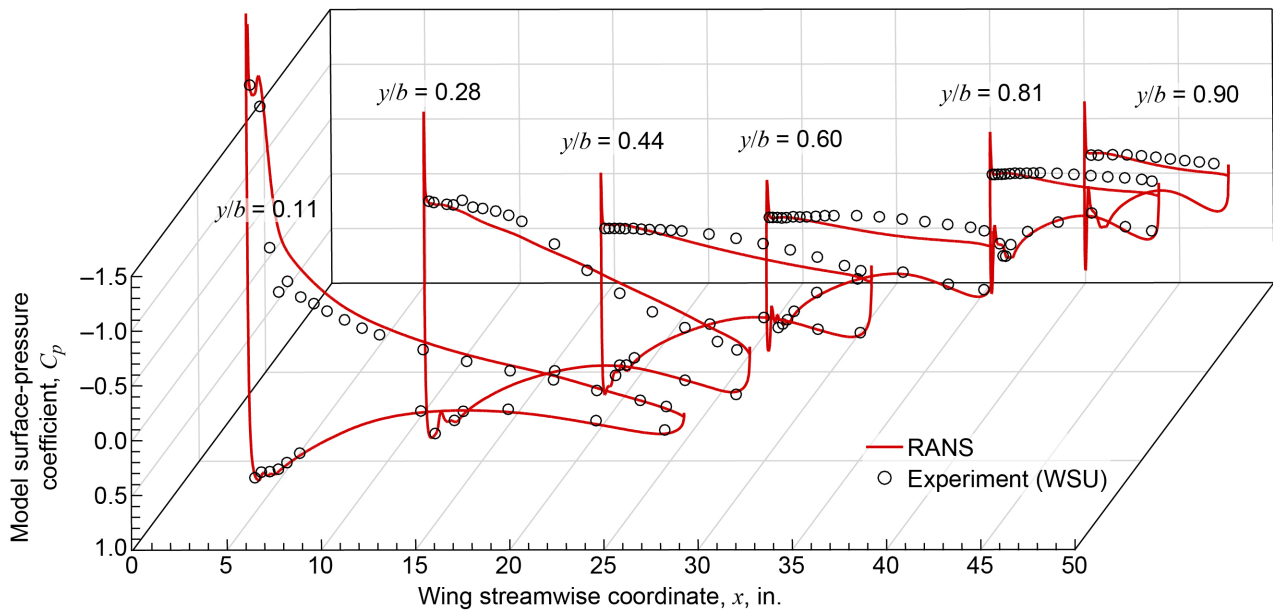


Figure 53.—Comparison of surface pressure coefficient CFD results with experimental data for 3D smooth maximum scallop iced-wing configuration at  $\alpha = 10^\circ$  and  $Re = 1.6 \times 10^6$  and  $M = 0.17$ . Experimental data from 8.9-percent-scale model in WSU wind tunnel.

## 4.0 Summary of Results

### 4.1 Project Summary

The overall goal of the Swept-Wing Icing Project (SWIP, also known as SUNSET II) was to improve the experimental and computational simulation capability for icing on large swept wings typical of commercial transports. The specific objectives of this large, multi-organization, multiyear effort were (1) to produce a large experimental database of three-dimensional (3D) ice accretion geometries, (2) to develop an understanding of iced swept-wing aerodynamics, and (3) to determine the effect of 3D ice-shape geometric fidelity on aerodynamic simulation of swept-wing icing effects. The research was organized into several phases to accomplish these objectives.

The ice accretion and resulting iced aerodynamics were studied using the NASA Common Research Model (CRM) as the reference geometry. For this work, a 65-percent-scale version—CRM65—was used as the full-scale baseline airplane geometry. Ice-accretion testing was conducted in the NASA Icing Research Tunnel (IRT) using three hybrid swept-wing models representing three different stations along the span of the CRM65 wing. The 3D ice-accretion geometries obtained from these test campaigns were used to evaluate the results of NASA and Office National d'Etudes et de Recherches Aérospatiales (ONERA) 3D icing simulation tools (LEWICE3D and IGLOO3D).

In addition, the 3D ice-accretion geometries were used to develop a series of artificial ice shapes for low- and high-Reynolds-number aerodynamic testing. This was carried out using reflection-plane, semispan wing models designed for the low-Reynolds-number 7- by 10-ft atmospheric wind tunnel at Wichita State University (WSU) and for the high-Reynolds-number ONERA F1 large-scale pressurized wind tunnel. The integrated aerodynamic forces, moments, and surface pressures, along with mini-tuft flow visualizations, were acquired in each facility. Additional measurements performed at WSU included surface oil flow visualizations and wake flow-field surveys. An 8.9-percent-scale model of the CRM65 wing was tested at WSU for Reynolds number based upon the model mean aerodynamic chord (16.67 in.) of  $0.8 \times 10^6$ ,  $1.6 \times 10^6$ , and  $2.4 \times 10^6$ , which corresponded to freestream Mach number of 0.09, 0.18, and 0.27. A 13.3-percent-scale model of the CRM65 wing was tested at the ONERA F1 wind tunnel over a range of Reynolds number based upon the model mean aerodynamic chord (25.01 in.) of  $1.6 \times 10^6$  to  $11.9 \times 10^6$  with Mach number range of 0.09 to 0.34. The pressurization capability of the F1 facility was exploited to perform Reynolds number sensitivity studies at constant Mach number and Mach number sensitivity studies at constant Reynolds number.

Artificial ice-shape configurations of varying fidelity to the actual ice shapes were attached to the leading edges of the wind tunnel models. All configurations were full-span ice shapes. The 3D high-fidelity ice shapes were developed from the 3D ice-accretion measurements in the IRT and were considered to accurately reproduce all of the highly 3D geometric features associated with the IRT ice accretion. A series of lower fidelity ice-shape geometries were also developed and tested. 3D smooth ice shapes were based upon lofted cross-sectional cuts taken from the high-fidelity geometry. The overall geometry of the 3D smooth ice shapes varied along the span of the wing but did not include the highly 3D ice features, such as scallops or feathers. Additional 3D smooth configurations were developed based upon LEWICE3D results. Other lower fidelity artificial ice shapes described in this report include 3D discontinuous ice and simple 3D horn ice.

This research effort was jointly sponsored by NASA, the Federal Aviation Administration (FAA), and ONERA and was supported by Boeing, the University of Illinois, the University of Virginia, and the University of Washington. A significant amount of original research was conducted during this project, and the detailed results are presented in numerous references cited in this report as well as in ice-accretion and iced-wing aerodynamics databases. This program marks the first nonproprietary research program to accrete full-scale swept-wing ice-shape accretions in an icing tunnel and then conduct semispan wing aerodynamic testing on scaled ice accretions at high Reynolds number (i.e., up to  $11.9 \times 10^6$ ). During this work, several new experimental and computational techniques were developed or documented, and new knowledge about swept-wing icing aerodynamics was identified.

### 4.2 Key Contributions

The entirety of the experimental program conducted during this research program had never been attempted; this effort was the first to accrete full-scale swept-wing ice-shape accretions and test them on a semispan wing at scale at low- to high-Reynolds number. This section briefly explains some of the key innovations to experimental and computational methods that supported the successful completion of this research effort. It is anticipated that others can benefit from these methods and build and improve upon what was done in this research program.

*Designing and conducting IRT models and tests:* The aerodynamic testing on the swept wing required a full-span ice shape scaled from a full-scale ice accretion. Because ice-accretion scaling is not practical at the large-scale factors required to test a semispan CRM65 wing in the IRT, a new approach was needed. A method was developed to test wing sections representing multiple spanwise stations and use those

stations to construct a full-span ice accretion. Three spanwise stations were chosen based on ice-shape geometry calculated using LEWICE3D to produce the best representation of the full-span accretion. Three hybrid IRT models were used with full-scale leading edges. Ice was accreted and digitized, and methods were developed to morph these digital shapes into 3D full-span ice shapes for aerodynamic testing. Ice-accretion testing was conducted in the IRT tunnel environment to match full-scale accretion. Scaling of the ice-accretion tunnel conditions was required due to tunnel speed limitations, and the model leading-edge flow field was adjusted to provide free-air-like accretions. Significant innovation in test design and performance contributed to the success of the swept-wing ice-accretion testing.

*Hybrid model design method:* Hybrid models have full-scale leading edges and redesigned, reduced-chord aft sections that enable IRT testing of aircraft components that would otherwise be too large and present blockage that is too high to be accurately tested in an icing tunnel. Methods to design hybrid airfoils had been developed and tested, but methods for designing large hybrid airfoils for swept wings did not exist in the open literature. The first step in the design process for the swept-wing hybrid wind tunnel model took advantage of two-dimensional (2D) tools to produce a representative 2D hybrid airfoil. The full-scale leading edge chordwise extent was set based on LEWICE3D ice-accretion calculations in free-air icing conditions. The resulting 2D hybrid airfoil sections were extended spanwise and swept to create the 3D models for testing in the IRT. A single-element slotted flap was added to the hybrid model design to enable matching of the leading-edge flow conditions (e.g., attachment line location) over the angle-of-attack range defined for the icing mission scenarios. The 3D hybrid model designs were validated using 3D RANS and LEWICE3D simulation tools. These flow simulations explored the highly 3D interference of the tunnel walls, evaluated resulting flow separation, and helped optimize the flap deflections required.

*3D scanner development:* Generating a database of 3D experimental ice-accretion geometries and associated artificial ice shapes for subsequent aerodynamic testing required a robust measurement system that did not exist at the outset of this project. Therefore, a method to digitize ice accretion accurately and efficiently in 3D was required. The data must be processed and archived so that (1) comparisons to ice-accretion code results can be performed, (2) artificial ice shapes can be readily fabricated for aerodynamic testing (at different scales than the original ice accretion), and (3) the geometry may be readily adapted for CFD simulations. To accomplish this, a commercially available laser scanning method was adapted and its use on ice accretion developed and validated. Software was used to create data files appropriate for various rapid prototyping manufacturing methods. Such methods can be used

to fabricate artificial ice shapes from the scan data. The software also has exact surfacing capability to develop grids for computational analysis.

*Maximum combined cross section (MCCS) method:* Many of the ice accretions observed during the IRT test campaigns were highly 3D, such that any type of 2D description is limited. There is also a lack of quantitative methods to compare highly 3D ice shapes. Given that icing simulation tools typically provide 2D ice-shape cross sections, results of this type are required for comparison. The approach developed for this research effort was to take 30 section cuts through the 3D scan of the ice accretion perpendicular to the wing leading edge. These 30 section cuts were taken at a spacing of 0.2 in., thus covering 6 in. of ice accretion along the leading edge near the model centerline, 36 in. above the floor. The section cuts were projected onto a single plane and the maximum outer boundary was obtained. The resulting MCCS represents the outermost extent of the ice over that 6-in. segment. The 6-in. segment was determined to be sufficient to capture the significant features of the ice accretions in these test campaigns. The MCCS is designed to be equivalent to the traditional hand-tracing method, which typically results in the maximum outer boundary of an ice accretion and has been the basis for evaluation of icing simulation codes such as LEWICE3D.

*3D artificial ice-shape development:* This research program was the first time that swept-wing high-fidelity full-span and full-scale ice shapes were developed from icing tunnel accretions for aerodynamic testing. A method was developed to generate full-span artificial ice shapes from limited partial-span segments of digital representations of experimental ice accretions. A weighted averaging technique was used to interpolate the ice shapes from one scanned section to another scanned section. This interpolation method was applied over the length of the full-scale leading edge of the CRM65 using the high-fidelity ice shapes from the Inboard, Midspan, and Outboard models that were tested in the IRT. An extrapolation method was also developed to generate artificial ice shapes at the root and tip of the wing using the artificial ice shapes at the Outboard and Inboard model stations and results from the LEWICE3D ice-prediction code. Artificial ice shapes with reduced geometric fidelity were created for aerodynamic testing as well. To generate a low-fidelity ice-shape geometry, evenly spaced 2D cuts along the span of a high-fidelity interpolated ice shape were lofted through to create a solid geometry. Once full-span, artificial ice shapes were created for the high- and low-fidelity configurations, they were scaled for subscale aerodynamic testing. These scaled artificial ice shapes were merged with the removable leading edge of a wind tunnel model using functions in the Geomagic Studio software package. The iced removable leading edges were 3D printed using a stereolithography (SLA) rapid prototype manufacturing technique.

*Aerodynamic testing:* Aerodynamic testing of the CRM65 semispan wing with full-span ice shapes was performed to document the iced-wing performance, evaluate the effect of ice-shape fidelity, evaluate Reynolds and Mach number effects, and better understand the clean and iced swept-wing flow fields that control the aerodynamic performance. This research represents the first comprehensive effort to accomplish these goals. While the aerodynamic tools themselves were not new, their application and combination to help accomplish these goals was innovative. The combination of low- and high-Reynolds-number testing in two separate wind tunnel facilities reduced risk and increased efficiency, as some tasks were more easily accomplished in the atmospheric tunnel environment. The combination of force balance data, surface pressure data, fluorescent mini-tuft and fluorescent surface oil flow visualization, and five-hole probe wake surveys provided quantitative data and insights into the flow field to help explain the complex behavior of the iced wing. The systematic use of multiple levels of ice-shape fidelity, including simple geometric representations, explored the impact of fidelity on aerodynamics. The aerodynamic impacts were quantified in terms of traditional parameters, such as maximum lift coefficient and stalling angle of attack. Additional performance parameters were identified and adapted for application to iced swept-wing aerodynamics. These parameters, such as usable lift, associate the change in pitching moment with respect to angle of attack due to increasing flow separation on the wing.

*Integration of 3D computational methods with experiment:* Computational and experimental simulation tools, most of them 3D, were strongly integrated throughout this research program, and indeed made the program feasible. This was a first for 3D swept-wing ice-shape testing in the public domain. Initially 3D RANS and LEWICE3D calculations on the baseline CRM in free air allowed the selection of realistic icing scenarios and provided key input to the hybrid model design process. The hybrid model designs were extensively tested in the icing tunnel with 3D simulations, again using 3D RANS to simulate the model in the tunnel and LEWICE3D to predict the ice accretion. This helped in understanding the complex interaction between the model and the tunnel and, in effect, allowed the design of the hybrid models in the 3D tunnel environment. 3D RANS was also used to model the clean semispan wing in the aerodynamic tunnel, which provided critical insight and confidence in the aerodynamic testing. The 3D full-span ice accretion design and construction relied on 3D scan data processing and CAD tools, and the size of the data sets stressed the ability to compute and morph the shapes. The experimental ice-accretion results were subsequently used to perform initial comparisons of IGLOO3D and two versions of LEWICE3D for ice-accretion prediction. Similarly, an initial attempt was made to simulate the

aerodynamics of the iced wing using 3D CFD tools. The quality of the tools greatly enhanced the quality of the testing.

*Experimental ice accretion and aerodynamics database:* The experimental data generated in this research effort have been compiled into a comprehensive database. The database will be located at <https://commonresearchmodel.larc.nasa.gov/home-2/icing-research>. The ice accretion test results from the three IRT test campaigns include the measured test conditions, photographs, ice scans, and MCCA. The aerodynamic test results from two F1 test campaigns and four WSU test campaigns include measured test conditions, performance coefficients from force balance measurements, surface pressure data, and flow visualization images. The database also contains information about the test article geometry, including artificial ice-shape geometry, and instrumentation for ice accretion and aerodynamic tests.

It should be noted that all of these contributions, and indeed the research program itself, would not have been possible without the participation of a committed team of researchers from multiple organizations. Researchers from Government, industry, and universities all brought different critical skills to allow this technically challenging program to be successful. The core team developed a collaborative and inclusive research style that allowed the team's diverse skills to effectively engage in the program over its multiyear duration.

The completion of this research effort, along with the numerous and significant contributions noted here, would not have been possible without the sustained financial and management support at NASA, the FAA, and ONERA over a period of approximately 7 years. This type of commitment is needed to provide fundamental advancements in the state of the art in certain research focus areas. The solutions to these complicated problems inherently require sustained resources over periods of time longer than typical project life cycles.

## 5.0 Concluding Remarks

### 5.1 Conclusions

- While both two-dimensional (2D) and three-dimensional (3D) computational simulation tools were used in the hybrid model design process, many 3D simulations were required to refine the model design in the presence of the wind tunnel walls. This was due to the strong interaction of the swept-wing flow with the tunnel walls, which resulted in a highly 3D flow field on the hybrid models. These results emphasize the need to perform efficient 3D flow simulations at the outset of the process. The 2D tools have limited value for large models where the wind tunnel walls produce 3D flow effects that must be taken into account.

- In a number of cases, the computational and experimental ice-shape comparisons revealed significant differences. In some cases, particularly for warmer temperatures, the simulation-based ice shapes tended to underpredict the experimental ice shapes defined by the maximum combined cross section (MCCS). For the IGLOO3D simulations with an ice density of  $917 \text{ kg/m}^3$ , the code results better matched the average ice-shape cross section. These observations are consistent with the inability of the icing codes to account for the numerous voids and individual feather or scallop features of the experimental ice accretion. Another common trend in the comparison of the simulation and experimental ice-shape results was that the poorest agreement occurred for the Inboard model. This trend may indicate some type of systematic problem with the numerical models, a possible effect of the large model on the icing cloud in the Icing Research Tunnel (IRT), or some combination of these two factors. The ice-shape comparisons also provided a strong motivation for the aerodynamic research that comprised the other major objectives of this research effort. The computational and experimental ice-shape comparisons were largely qualitative, using terminology such as “good” and “poor.” In addition, the experimental ice accretions were highly 3D, whereas the icing code results were primarily 2D. Therefore, research to understand this effect on the flow field, and thus on the aerodynamics, is very important.
- Two types of flow fields were identified based on two key features that were observed to result from horn-ice-shape geometry. These features result from differences in the formation and development of the leading-edge vortex that dominates these flow fields at moderate to high angle of attack. These two flow-field types are referred to as “Type I” and “Type II.” Type I flow fields are dominated by spanwise-running leading-edge vortices generated by flow separation from the leading-edge ice accretion. Type II flow fields lack the leading-edge spanwise vortex, which appears to be suppressed by streamwise vorticity resulting from highly 3D horns (scallop) and, in some cases, ice shapes with surface roughness added.
- For the horn ice shapes (which includes the scalloped shapes), aerodynamic results on the lower fidelity 3D smooth shapes based on the outermost surface geometry (akin to the MCCS) always generated nonconservative performance degradation as compared with the high-fidelity ice shapes. The 3D ice features of the high-fidelity horn ice configurations are important to the iced-wing flow field and resulting integrated performance of this swept-wing configuration.
- The aerodynamic studies were used to propose a new swept-wing ice-shape classification system:
  - Roughness: Key parameters are roughness height, location, and density.
  - Streamwise: Key parameters are shape thickness, roughness height, and density.
  - 3D leading-edge horn: Key parameters are horn height, location, angle, and roughness.
  - Highly 3D leading-edge horn: Key parameters are spanwise averaged horn height, location, angle, spanwise variation of horn geometry, and roughness.
  - Spanwise ridge: Key parameters are location and height.
- While Reynolds and Mach number effects are important for quantifying the clean-wing performance, for this swept-wing configuration there is very little to no effect for an iced wing with 3D, high-fidelity artificial ice shapes or 3D smooth ice shapes with grit roughness. These conclusions are consistent with the large volume of past research on iced airfoils. However, some differences were noted for the associated stalling angle of the iced swept wing and for various lower fidelity versions of the leading-edge ice accretion.
- Two different grid approaches were evaluated for the flow-field computation of 3D ice shapes attached to a realistic transport aircraft wing. The first approach is based on the Quantum grid deformation software, and the second is based on use of the “order 0” immersed boundary conditions (IBC) method. Both methods provided satisfactory results on an ice-shape configuration tested in the Office National d’Etudes et de Recherches Aérospatiales (ONERA) F1 wind tunnel during this program. However, better agreement was observed on pressure distributions with the IBC method as compared with results obtained on the Quantum grid, although no specific grid refinement was done for IBC. Further validation is needed, taking into account grid refinement studies and more complex ice-shape geometries, but the use of simple immersed boundary methods applied on a standard-reference clean-wing grid seems quite promising for a good estimation of the pressure field developed over a 3D wing with complex ice shapes. Furthermore, 3D Reynolds-averaged Navier–Stokes (RANS) simulations performed with the same ice-shape configuration using more conventional unstructured meshes also yielded promising results. This approach deserves further investigation.

## 5.2 Recommendations

The following recommendations, based on lessons learned through this program, may be useful in improving and guiding future swept-wing icing research. Recommendations to improve the conducting of the research are listed first (Sec. 5.2.1), followed by recommendations for future research (Sec. 5.2.2).

### 5.2.1 Experimental and Computational Methods

- Improvements are needed in the methods used to build the full-span ice shape based on the limited ice-accretion segments digitized from the icing tunnel tests. These improvements include
  - Better blending where the repeated morphed ice-shape sections are merged
  - A lap joint design for better sealing of the adjoining section
  - More robust and capable 3D-geometry software
  - A solution for current computing-power limits
- Version control is extremely important in this research and must be carefully and consistently implemented from the beginning. Important items to control include the detailed model and ice-shape geometry as well as the icing conditions for testing and simulation.
- Because Reynolds and Mach number effects on this iced swept-wing configuration were small, additional use of lower cost, lower Reynolds number facilities could provide even more efficient use of resources.
- Methods to better quantify and compare these highly 3D scallop-ice-shape geometries are needed, followed by better methods to systematically produce aerodynamically inspired, simplified versions appropriate for wind tunnel testing and computational fluid dynamics (CFD) modeling.
- Future hybrid swept-wing model design methods may be able to reduce the 2D initial designs and move more rapidly to 3D methods that better represent the complex flow on the model in the icing tunnel. The effect of ice accretion on the hybrid model's ability to perform as designed during the icing tunnel testing should be considered.
- The icing simulations presented in this report provide a basis for future improvements in ice-accretion codes to capture the highly 3D ice shapes observed on swept wings. A first approach should consist of establishing some best practices to infer the main 3D structure (scallop gaps and wavelength, for instance) from the ice-accretion code result and the icing conditions. Another approach would be to improve the

ice-accretion codes so they produce scallops with the expected level of fidelity. Progress on the generation of ice shapes in a 3D multistep approach is also needed. Finally, a better understanding of the mechanisms leading to the development of scallops could help to better characterize the main features of the scallop geometry.

### 5.2.2 Additional Research Needed

- All but one of the ice shapes tested in the current study were classified as horn ice shapes. Testing of shapes from other classifications is needed to better understand those ice shapes and their aerodynamics.
- Only one swept-wing geometry was used in this research. Airfoil research has shown that ice-accretion shape and aerodynamic performance depends on the airfoil geometry. For swept wings, the sweep angle is very important in determining the leading-edge vortex, which was seen to be a key flow-field feature for both clean and iced swept wings. Research is needed to help understand how different swept-wing geometries are affected by icing.
- The current research focused on ice accretion and aerodynamic performance. Measurements that might help in understanding the flow field that drives the aerodynamics included only limited surface techniques and a downstream wake survey. Off-body iced swept-wing flow-field measurements and analysis in the vicinity of the ice shapes are required to understand the flow physics and provide important information for CFD simulation. This approach, coupled with some time-dependent measurements, has provided critical insight in previous research on iced-airfoil flow fields. These measurements would help to
  - Document and improve understanding of the aerodynamics of Type I and Type II flow fields
  - Understand the stalling process
  - Understand challenges in reproducing high-fidelity drag
  - Develop CFD methods
  - Design more accurate simplified ice shapes

## Appendix—Nomenclature

### Acronyms

2D	two-dimensional
3D	three-dimensional
AIAA	American Institute of Aeronautics and Astronautics
AoA	angle of attack
BC	Boeing Company
CFB	clean flight baseline
CFD	computational fluid dynamics
CFL	Courant–Friedrichs–Lewy
CRM	Common Research Model
CRM65	Common Research Model 65-percent-scale version
CT	computed tomography
FAA	Federal Aviation Administration
FS	full scale
IBC	immersed boundary conditions
IDDES	improved delayed detached-eddy simulation
IFB	iced flight baseline
IRT	Icing Research Tunnel
LE	leading edge
LES	large-eddy simulation
LWC	liquid water content
MAC	mean aerodynamic chord
MCCS	maximum combined cross section
MVD	median volumetric diameter
NACA	National Advisory Committee for Aeronautics
ONERA	Office National d’Etudes et de Recherches Aérospatiales
QCR	quadratic constitutive relation
RANS	Reynolds-averaged Navier–Stokes
RPM	rapid prototype manufacturing
SA	Spalart–Allmaras
SI units	Système International d’Unités
SLA	stereolithography
SST	shear stress transport
SWIP	Swept-Wing Icing Project
T-Rex	anisotropic tetrahedral extrusion
UAM	urban air mobility
UV	ultraviolet
UW	University of Washington
WSU	Wichita State University

### Symbols

$b$	wingspan
$C_D$	drag coefficient
$C_{D,\min}$	minimum drag coefficient
$C_{D,0.6}$	drag coefficient at $C_L = 0.6$
$C_L$	lift coefficient
$C_{L,\max}$	maximum lift coefficient
$C_{L,\text{use}}$	usable lift coefficient
$C_M$	quarter-chord mean aerodynamic chord pitching moment
$C_{M,\min}$	minimum quarter-chord mean aerodynamic chord pitching moment
$C_p$	model surface-pressure coefficient
$c$	local chord length perpendicular to the leading edge
$c_{\text{FS}}$	full-scale normal chord
$c_{\text{Hyb}}$	hybrid model normal chord
$k$	ice-horn height
$K$	dissipation coefficient
$M$	freestream Mach number
$p_o$	freestream total pressure
$q_\infty$	freestream dynamic pressure
$Re$	freestream Reynolds number based on mean aerodynamic chord
$s$	wrap distance
$T_{\text{static}}$	static temperature
$V_{s,1g}$	aircraft 1g stall speed
$x$	wing streamwise coordinate
$x'$	wing chordwise coordinate
$y$	wing spanwise coordinate
$z$	wing thickness coordinate
$z'$	wing vertical coordinate
$\alpha$	angle of attack
$\alpha_{\text{geo}}$	geometric angle of attack
$\alpha_{\text{stall}}$	stalling angle of attack, consistent with the maximum lift coefficient
$\alpha_{\text{use}}$	usable angle of attack, consistent with the usable lift coefficient
$\beta$	local collection efficiency
$\delta$	flap angle
$\theta$	ice-horn angle measured at its base location on airfoil surface

## References

1. Leopold, D.: Flight in Icing Regulatory Evolution and the Influence on Aircraft Design. SAE Int. J. Adv. & Curr. Prac. in Mobility (SAE 2019-01-1958), vol. 2, no. 1, 2020, pp. 71-77.
2. Broeren, Andy P., et al.: Aerodynamic Simulation of Ice Accretion on Airfoils. NASA TP-2011-216929, 2011. <https://ntrs.nasa.gov>
3. Bragg, M., et al.: Airfoil Ice-Accretion Aerodynamics Simulation. AIAA 2007-0085, 2007.
4. Bragg, M.B.; Broeren, A.P.; and Blumenthal, L.A.: Iced-Airfoil and Wing Aerodynamics. SAE 2003-01-2098, 2003.
5. Bragg, M.B.; Broeren, A.P.; and Blumenthal, L.A.: Iced-Airfoil Aerodynamics. Prog. Aerosp. Sci., vol. 41, no. 5, 2005, pp. 323-362.
6. Busch, Greg; Broeren, Andy; and Bragg, Michael: Aerodynamic Simulation of a Horn-Ice Accretion on a Subscale Model. AIAA 2007-87, 2007.
7. Busch, Greg T.; Broeren, Andy P.; and Bragg, Michael B.: Aerodynamic Simulation of a Horn-Ice Accretion on a Subscale Model. J. Aircr., vol. 45, no. 2, 2008, pp. 604-613.
8. Blumenthal, L.A.: Surface Pressure Measurement on a Three-Dimensional Ice Shape. M.S. Thesis, Univ. of Illinois, 2005.
9. Busch, G.T.: Ice Accretion Aerodynamic Simulation on a Subscale Model. Doctoral dissertation, Univ. of Illinois, 2006.
10. Blumenthal, Leia A., et al.: Issues in Ice Accretion Aerodynamic Simulation on a Subscale Model. AIAA 2006-262, 2006.
11. Busch, Greg; Broeren, Andy; and Bragg, Michael: Aerodynamic Fidelity of Sub-Scale Two-Dimensional Ice Accretion Simulation. AIAA 2008-7062, 2008.
12. Broeren, Andy P.; Busch, Greg T.; and Bragg, Michael B.: Aerodynamic Fidelity of Ice Accretion Simulation on a Subscale Model. SAE Transactions (SAE 2007-01-3285), vol. 116, 2007, pp. 560-575.
13. Moens, F.: SUNSET Project: Numerical Investigations for the Preparation of the F1 Test Campaign. ONERA Report N° RT 1/12405 DAAP, April 2007.
14. CassouDeSalle, D.; and Gilliot, A.: SUNSET (Studies on Scaling Effects due to Ice) Tests at High Reynolds Number in F1 Wind Tunnel. ONERA Report N° PV 4/12361 DSFM, December 2008.
15. CassouDeSalle, Denis, et al.: Experimental Investigations of Simulated Ice Accretions at High Reynolds Numbers in the Onera F1 Wind Tunnel. AIAA 2009-4265, 2009.
16. Broeren, Andy P., et al.: Effect of High-Fidelity Ice-Accretion Simulations on Full-Scale Airfoil Performance. J. Aircr., vol. 47, no. 1, 2010, pp. 240-254.
17. Broeren, Andy P., et al.: Effect of High-Fidelity Ice-Accretion Simulations on the Performance of a Full-Scale Airfoil Model. AIAA 2008-434, 2008.
18. Busch, Greg T.: Experimental Study of Full-Scale Iced-Airfoil Aerodynamic Performance Using Sub-Scale Simulations. Ph.D. Dissertation, Univ. of Illinois, 2010.
19. Duclercq, Marion; Brunet, Vincent; and Moens, Frederic: Physical Analysis of the Separated Flow Around an Iced Airfoil Based on ZDES Simulations. AIAA 2012-2798, 2012.
20. Addy, Harold E., Jr., et al.: Ice Accretions and Full-Scale Iced Aerodynamic Performance Data for a Two-Dimensional NACA 23012 Airfoil. NASA/TP-2016-218348, 2016. <https://ntrs.nasa.gov>
21. Broeren, Andy P., et al.: Swept-Wing Ice Accretion Characterization and Aerodynamics. AIAA 2013-2824 (NASA TM-2013-216555), 2013. <https://ntrs.nasa.gov>
22. Potapczuk, Mark G.; and Broeren, Andy P.: An Integrated Approach to Swept Wing Icing Simulation. Presented at the 7th European Conference for Aeronautics and Space Sciences, Milan, Italy, 2017.
23. Bragg, M.B.; Kerho, M.F.; and Khodadoust, A.: LDV Flowfield Measurements on a Straight and Swept Wing With a Simulated Ice Accretion. AIAA 93-300, 1993.
24. Kwon, Oh J.; and Sankar, Lakshmi N.: Numerical Study of the Effects of Icing on Fixed and Rotary Wing Performance. AIAA 91-662, 1991.
25. Khodadoust, A.; and Bragg, M.B.: Measured Aerodynamic Performance of a Swept Wing With a Simulated Ice Accretion. AIAA 90-490, 1990.
26. Bragg, M.B., et al.: Effect of a Simulated Ice Accretion on the Aerodynamics of a Swept Wing. AIAA 91-442, 1991.
27. Vargas, Mario, et al.: Ice Accretions on a Swept GLC-305 Airfoil. NASA/TM-2002-211557 (SAE 02GAA-43), 2002. <https://ntrs.nasa.gov>
28. Papadakis, Michael, et al.: Performance of a Swept Wing With Ice Accretions. AIAA 2003-731, 2003.
29. Papadakis, Michael, et al.: Experimental Investigation of Ice Accretion Effects on a Swept Wing. DOT/FAA/AR-05/39, 2005.
30. Reehorst, Andrew, et al.: Wind Tunnel Measured Effects on a Twin-Engine Short-Haul Transport Caused by Simulated Ice Accretions. NASA TM-107143 (AIAA 96-0871), 1996. <https://ntrs.nasa.gov>
31. Reehorst, Andrew, et al.: Wind Tunnel Measured Effects on a Twin-Engine Short-Haul Transport Caused by Simulated Ice Accretions: Data Report. NASA TM-107419, 1997. <https://ntrs.nasa.gov>

32. Papadakis, Michael, et al.: Experimental Investigation of Simulated Ice Accretions on a Full-Scale T-tail. AIAA 2001–90, 2001.
33. Papadakis, Michael, et al.: Effects of Roughness on the Aerodynamic Performance of a Business Jet Tail. AIAA 2002–242, 2002.
34. Broeren, Andy P.; Diebold, Jeff M.; and Bragg, Michael B.: Aerodynamic Classification of Swept-Wing Ice Accretion. NASA/TM—2013-216381 (DOT/FAA/TC–13/21), 2013. <https://ntrs.nasa.gov>
35. Diebold, Jeff M.; Broeren, Andy P.; and Bragg, Michael B.: Aerodynamic Classification of Swept-Wing Ice Accretion. AIAA 2013–2825, 2013.
36. Bragg, Michael B., et al.: Ice Shape Classification for Swept Wings. AIAA 2020–2845, 2020.
37. Vassberg, John C., et al.: Development of a Common Research Model for Applied CFD Validation Studies. AIAA 2008–6919, 2008.
38. Rivers, Melissa B.; and Dittberner, Ashley: Experimental Investigation of the NASA Common Research Model (Invited). AIAA 2010–4218, 2010.
39. Rivers, Melissa B.; and Dittberner, Ashley: Experimental Investigations of the NASA Common Research Model in the NASA Langley National Transonic Facility and the NASA Ames 11-Ft Transonic Wind Tunnel (Invited). AIAA 2011–1126, 2011.
40. Vassberg, John C., et al.: Summary of the Fourth AIAA CFD Drag Prediction Workshop. AIAA 2010–4547, 2010.
41. Reehorst, Andrew L.; and Richter, G. Paul: New Methods and Materials for Molding and Casting Ice Formations. NASA TM–100126, 1987. <https://ntrs.nasa.gov>
42. Lee, Sam, et al.: Development of 3-D Ice Accretion Measurement Method. NASA TM—2012-217702 (AIAA 2012–2938), 2012. <https://ntrs.nasa.gov>
43. Monastero, Marianne Cathleen: Validation of 3-D Ice Accretion Documentation and Replication Method Including Pressure-Sensitive Paint. M.S. Thesis, Univ. of Illinois, Urbana-Champaign, 2013.
44. Lee, Sam, et al.: Implementation and Validation of 3-D Ice Accretion Measurement Methodology. AIAA 2014–2613, 2014.
45. Broeren, Andy P., et al.: Validation of 3-D Ice Accretion Measurement Methodology for Experimental Aerodynamic Simulation. NASA/TM—2015-218724, 2015. <https://ntrs.nasa.gov>
46. Monastero, Marianne C.; and Bragg, Michael B.: Validation of 3-D Ice Accretion Measurement Methodology Using Pressure-Sensitive Paint. AIAA 2014–2615, 2014.
47. Broeren, Andy P., et al.: Three-Dimensional Ice-Accretion Measurement Methodology for Experimental Aerodynamic Simulation. *J. Aircr.*, vol. 55, no. 2, 2018, pp. 817–828.
48. Diebold, Jeff M.; Monastero, Marianne C.; and Bragg, Michael B.: Aerodynamics of a Swept Wing With Ice Accretion at Low Reynolds Number. AIAA 2012–2795, 2012.
49. Diebold, Jeffrey Michael: Aerodynamics of a Swept Wing With Leading-Edge Ice at Low Reynolds Number. M.S. Thesis, Univ. of Illinois, Urbana-Champaign, 2012.
50. Diebold, Jeff M.; and Bragg, Michael B.: Study of a Swept Wing With Leading-Edge Ice Using a Wake Survey Technique. AIAA 2013–0245, 2013.
51. Diebold, Jeffrey Michael: The Effects of Turbulence on the Measurements of Five-Hole Probes. Ph.D. Dissertation, Univ. of Illinois, Urbana-Champaign, 2017.
52. Fujiwara, Gustavo Eidji Camarinha: Design of 3D Swept Wing Hybrid Models for Icing Wind Tunnel Tests. M.S. Thesis, Univ. of Illinois, Urbana-Champaign, 2014.
53. Fujiwara, Gustavo, et al.: Development of Experimental Icing Simulations Capability for Full-Scale Swept Wings: Hybrid Design Process, Years 1 and 2. NASA/CR—2017-219573, 2017. <https://ntrs.nasa.gov>
54. Sclafani, Anthony J., et al.: Extended OVERFLOW Analysis of the NASA Trap Wing Wind Tunnel Model. AIAA 2012–2919, 2012.
55. Bidwell, Colin S.; and Potapczuk, Mark G.: User’s Manual for the NASA Lewis Three-Dimensional Ice Accretion Code (LEWICE3D). NASA TM–105974, 1993. <https://ntrs.nasa.gov>
56. Saeed, Farooq; Selig, Michael S.; and Bragg, Michael B.: Hybrid Airfoil Design Procedure Validation for Full-Scale Ice Accretion Simulation. *J. Aircr.*, vol. 36, no. 5, 1999, pp. 769–776.
57. Saeed, Farooq; Selig, Michael S.; and Bragg, Michael B.: Hybrid Airfoil Design to Simulate Full-Scale Ice Accretion Throughout a Given  $\alpha$  Range. *J. Aircr.*, vol. 35, no. 2, 1998, pp. 233–239.
58. Saeed, Farooq; Selig, Michael S.; and Bragg, Michael B.: Design of Subscale Airfoils With Full-Scale Leading Edges for Ice Accretion Testing. *J. Aircr.*, vol. 34, no. 1, 1997, pp. 94–100.
59. Mortonson, Andrew J.: Use of Hybrid Airfoil Design in Icing Wind Tunnel Tests of Large Scale Swept Wings. M.S. Thesis, Univ. of Illinois, Urbana-Champaign, 2011.
60. Fujiwara, Gustavo E.C., et al.: A Hybrid Airfoil Design Method for Icing Wind Tunnel Tests. AIAA 2013–2826, 2013.
61. Fujiwara, Gustavo E.C.; and Bragg, Michael B.: Method for Designing Hybrid Airfoils for Icing Wind-Tunnel Tests. *J. Aircr.*, vol. 56, no. 1, 2019, pp. 137–148.
62. Fujiwara, Gustavo E.C., et al.: 3D Swept Hybrid Wing Design Method for Icing Wind Tunnel Tests. AIAA 2014–2616, 2014.

63. Fujiwara, Gustavo E.C.; and Bragg, Michael B.: Method for Designing Three-Dimensional Swept Hybrid Wings for Icing Wind-Tunnel Tests. *J. Aircr.*, vol. 56, no. 2, 2019, pp. 730–746.
64. Wiberg, Brock Demont: Large-Scale Swept-Wing Ice Accretion Modeling in the NASA Glenn Icing Research Tunnel Using LEWICE3D. M.S. Thesis, Univ. of Illinois, Urbana-Champaign, 2013.
65. Wiberg, Brock D., et al.: Large-Scale, Swept-Wing Icing Simulations in the NASA Glenn Icing Research Tunnel Using LEWICE3D. AIAA 2014–2617, 2014.
66. Butler, C.; and Loth, E.: Detached Eddy Simulation on a Swept Hybrid Model in the IRT. SAE 2015–01–2122, 2015.
67. Butler, Cameron; Qin, Chao; and Loth, Eric: Improved Delayed Detached-Eddy Simulation on a Swept Hybrid Model in IRT. AIAA 2016–3736, 2016.
68. Broeren, Andy P., et al.: Ice-Accretion Test Results for Three Large-Scale Swept-Wing Models in the NASA Icing Research Tunnel. AIAA 2016–3733 (NASA/TM—2016-219137), 2016. <https://ntrs.nasa.gov>
69. Steen, Laura E., et al.: NASA Glenn Icing Research Tunnel: 2014 and 2015 Cloud Calibration Procedures and Results. NASA TM—2015-218758, 2015. <https://ntrs.nasa.gov>
70. Soeder, Ronald H., et al.: Glenn Icing Research Tunnel User Manual. NASA TM—2003-212004, 2003. Available from the NASA STI Program.
71. Anderson, David N.: Manual of Scaling Methods. NASA/CR—2004-212875, 2004. <https://ntrs.nasa.gov>
72. Tsao, J.; and Lee, S.: Evaluation of Icing Scaling on Swept NACA 0012 Airfoil Models. SAE 2011–38–0081 (NASA/CR—2012-217419), 2011. <https://ntrs.nasa.gov>
73. Tsao, Jen-Ching: Further Evaluation of Swept Wing Icing Scaling with Maximum Combined Cross Section Ice Shape Profiles. AIAA 2018–3183, 2018.
74. Fujiwara, Gustavo E.C., et al.: Computational and Experimental Ice Accretions of Large Swept Wings in the Icing Research Tunnel. AIAA 2016–3734, 2016.
75. Fujiwara, Gustavo E.C.; Bragg, Michael B.; and Broeren, Andy P.: Comparison of Computational and Experimental Ice Accretions of Large Swept Wings. *J. Aircr.*, vol. 57, no. 2, 2020, pp. 342–359.
76. Yadlin, Yoram, et al.: Icing Simulation Research Supporting the Ice-Accretion Testing of Large-Scale Swept-Wing Models. NASA/CR—2018-219871 (DOT/FAA/TC–18/17), 2018. <https://ntrs.nasa.gov>
77. Radenac, Emmanuel: Validation of a 3D Ice Accretion Tool on Swept Wings of the SUNSET2 Program. AIAA 2016–3735, 2016.
78. Radenac, E., et al.: IGLOO3D Computations of the Ice Accretion on Swept-Wings of the SUNSET2 Database. SAE 2019–01–1935, 2019.
79. Torz-Dupuis, L.: Test NASA SUNSET II of the CRM65 Wing Model Representative of the CRM65 Wing at 1/7.5 on Half Model Set-Up in the ONERA F1 Wind Tunnel. ONERA Report No. PV 4/23611 DMPE/DSFM, Dec. 2017.
80. Rossoni, L.: Test NASA SUNSET II—Part 2 of the CRM65 Wing, Representative of the CRM65 Wing at 1/7.5 on Half Model Set-Up in the ONERA F1 Wind Tunnel. ONERA Report No. PV 8/23611 DMPE/DSFM, Mar. 2019.
81. Woodard, Brian S., et al.: Preliminary Testing of Low Reynolds Number Aerodynamics for a Swept Wing With Artificial Ice Roughness. DOT/FAA/TC–17/48, 2017.
82. Broeren, Andy P., et al.: Independent Effects of Reynolds and Mach Numbers on the Aerodynamics of an Iced Swept Wing. NASA/TM—2019-220012 (AIAA–2018–3492), 2019. <https://ntrs.nasa.gov>
83. Broeren, Andy P., et al.: Low-Reynolds Number Aerodynamics of an 8.9 Percent Scale Semispan Swept Wing for Assessment of Icing Effects. NASA/TM—2017-219533 (AIAA 2017–4372), 2017. <https://ntrs.nasa.gov>
84. Camello, Stephanie C., et al.: Effect of Ice Shape Fidelity on Swept-Wing Aerodynamic Performance. AIAA 2017–4373, 2017.
85. Lum, Christopher W., et al.: The Application of a Five-Hole Probe Wake-Survey Technique to the Study of Swept Wing Icing Aerodynamics. AIAA 2017–4374, 2017.
86. Lee, Sam, et al.: Comparison of Iced Aerodynamic Measurements on a Swept Wing From Two Wind Tunnels. AIAA 2018–3493, 2018.
87. Lee, S., et al.: Additional Comparison of Iced Aerodynamic Measurements on a Swept Wing From Two Wind Tunnels. SAE 2019–01–1986, 2019.
88. Diebold, Jeffrey M., et al.: Experimental Study of Splitter Plates for Use With Semispan Wing Models. AIAA 2015–1227, 2015.
89. Furlong, G. Chester; and McHugh, James G.: A Summary and Analysis of the Low-Speed Longitudinal Characteristics of Swept Wings at High Reynolds Number. NACA TR–1339, 1957.
90. Lynch, Frank T.; and Khodadoust, Abdollah: Effects of Ice Accretions on Aircraft Aerodynamics. *Prog. Aerosp. Sci.*, vol. 37, no. 8, 2001, pp. 669–767.
91. 3D Systems, Inc.: 3D Scanning, Design and Reverse Engineering Software From 3D Systems. Geomagic, 2022. <http://www.geomagic.com> Accessed Feb. 1, 2022.

92. Camello, Stephanie C., et al.: Generation of Full-Span Leading-Edge 3D Ice Shapes for Swept-Wing Aerodynamic Testing. AIAA 2016–3737, 2016.
93. Camello, Stephanie Chen: Effect of Ice Accretion Simulation Fidelity on Low-Reynolds Number Swept-Wing Aerodynamic Performance. M.S. Thesis, Univ. of Washington, 2017.
94. Lee, S., et al.: Effect of Geometric Fidelity on the Aerodynamics of a Swept Wing With Scalloped Ice Accretion. AIAA 2020–2847, 2020.
95. Fujiwara, Gustavo E.C.; and Bragg, Michael B.: 3D Computational Icing Method for Aircraft Conceptual Design. AIAA 2017–4375, 2017.
96. Broeren, Andy P., et al.: Experimental Aerodynamic Simulation of a Glaze Ice Accretion on a Swept Wing. SAE 2019–01–1987, 2019.
97. Broeren, Andy P., et al.: Effect of Geometric Fidelity on the Aerodynamics of a Swept Wing With Glaze Ice Accretion. AIAA 2020–2846, 2020.
98. Woodard, Brian, et al.: Experimental Aerodynamic Simulation of a Scallop Ice Accretion on a Swept Wing. SAE 2019–01–1984, 2019.
99. Woodard, Brian S.; and Bragg, Michael B.: Effect of Spanwise Discontinuities on the Aerodynamics of a Swept Wing With Scalloped Ice Accretion. AIAA 2020–2848, 2020.
100. Federal Aviation Administration: Performance and Handling Characteristics in Icing Conditions. Advisory Circular AC 25–25A, 2014.
101. Woodard, Brian S., et al.: Summary of Ice Shape Geometric Fidelity Studies on an Iced Swept Wing. AIAA 2018–3494, 2018.
102. Moens, Frederic, et al.: Transition Prediction and Impact on a Three-Dimensional High-Lift-Wing Configuration. *J. Aircr.*, vol. 45, no. 5, 2008, pp. 1751–1766.
103. Jun, GaRam, et al.: Computational Aerodynamic Analysis of Three-Dimensional Ice Shapes on a NACA 23012 Airfoil. AIAA 2104–2202, 2014.
104. Stebbins, Spencer J.; Loth, Eric; and Qin, Chao: Computations of Swept Wing Icing Aerodynamics. AIAA 2019–0328, 2019.
105. Stebbins, Spencer, et al.: Aerodynamics of a Common Research Model Wing With Leading-Edge Ice Shape. *J. Aircr.*, vol. 58, no. 4, 2021.
106. Stebbins, Spencer J.: Review and Study of Aerodynamic Simulations of Lifting Bodies With Ice Accretion. M.S. Thesis, Univ. of Virginia, 2018.
107. Stebbins, Spencer J., et al.: Review of Computational Methods for Aerodynamic Analysis of Iced Lifting Surfaces. *Prog. Aerosp. Sci.*, vol. 111, no. 100583, 2019.
108. Terracol, Marc; Manoha Eric; and Lemoine Benoit: Investigation of the Unsteady Flow and Noise Sources Generation in a Slat Cove: Hybrid Zonal RANS/LES Simulation and Dedicated Experiment. AIAA 2011–3203, 2011.
109. Péron, Stephanie, et al.: A Mixed Overset Grid/Immersed Boundary Approach for CFD Simulations of Complex Geometries. AIAA 2016–2055, 2016.
110. Péron, Stephanie, et al.: An Immersed Boundary Method for Preliminary Design Aerodynamic Studies of Complex Configurations. AIAA 2017–0362, 2017.
111. Renaud, Thomas, et al.: Validation of an Immersed Boundary Method for Compressible Flows. AIAA 2019–2179, 2019.
112. Reneaux, J.; Beaumier, P.; and Girodroux-Lavigne: Advanced Aerodynamic Applications With the elsA Software. *Onera AerospaceLab Journal*, issue 2, no. AL02–12, 2011. [https://aerospacelab.onera.fr/sites/w3.onera.fr.aerospacelab/files/AL2-12\\_2.pdf](https://aerospacelab.onera.fr/sites/w3.onera.fr.aerospacelab/files/AL2-12_2.pdf) Accessed Feb. 1, 2011.
113. Papadakis, Michael, et al.: Water Impingement Experiments on a NACA 23012 Airfoil With Simulated Glaze Ice Shapes. AIAA 2004–0565, 2004.
114. Poll, D.I.A.: Spiral Vortex Flow Over a Swept-Back Wing. *Aeronaut. J.*, vol. 90, no. 895, 1986, pp. 185–199.
115. Sandhu, Navdeep, et al.: Effect of Simulated Scalloped Ice on the Aerodynamics of a Swept-Wing at Low-Reynolds Number. AIAA 2018–3495, 2018.
116. Sandhu, Navdeep: Aerodynamics of Swept Wing With Simulated Scalloped Ice at Low Reynolds Number. M.S. Thesis, Univ. of Washington, 2018.
117. Yoshida, William Tsuyoshi: Investigation of the Flowfield Downstream of a Discontinuous Backward-Facing Step on a Swept Flat Plate. M.S. Thesis, Univ. of Washington, 2020.
118. Maruyama, Daigo; Bailly, Didier; and Carrier, Gerald: High-Quality Mesh Deformation Using Quaternions for Orthogonality Preservation. *AIAA J.*, vol. 52, no. 12, 2014, pp. 2712–2729.





